

ABSTRACT

Title of Thesis: MODELING OF INTERFACES: APPLICATIONS
 IN SURFACE AND POLYMER PHYSICS

Paul Patrone, Doctor of Philosophy, 2013

Dissertation directed by: Professor Theodore L. Einstein
 Department of Physics

In this dissertation, I give an overview of my work on multiscale modeling of interfaces in crystalline and block-copolymer systems. I focus on two distinct interface systems: steps on vicinal surfaces and microdomain interfaces in block-copolymers melts. For each system, I consider how to (i) define the interface, (ii) derive a coarse-grained model of the interface, and (iii) use the model to study morphological features of the interface. For vicinal surfaces, we define a step by means of ensemble averages, which leads to a Burton-Cabrera-Frank (BCF) -type model of surface evolution. Using the BCF model, we study the combined effects of step interactions and fluctuations. For block-copolymers, we define the microdomain interfaces in terms of the relative density of monomers and use the Leibler-Ohta-Kawasaki phase-field Hamiltonian to study the line-edge roughness.

MULTISCALE MODELING OF INTERFACES: APPLICATIONS
IN SURFACE AND POLYMER PHYSICS

by

Paul Patrone

Dissertation submitted to the Faculty of the Graduate School of the
University of Maryland, College Park in partial fulfillment
of the requirements for the
Doctor of Philosophy
2013

Advisory Committee:
Professor Theodore L. Einstein, Chair/Advisor
Professor Dionisios Margetis, Co-Advisor
Dr. Gregg M. Gallatin, Co-Advisor
Professor John D. Weeks
Professor Ricardo Nochetto

Acknowledgments

I acknowledge support under the National Institute of Standards and Technology American Recovery and Reinvestment Act Measurement Science and Engineering Fellowship Program Award 70NANB10H026 through the University of Maryland; and the NSF under MRSEC grant DMR 0520471 at the University of Maryland; and the Condensed Matter Theory Center at the University of Maryland. I also wish to thank Ted, Dio and Gregg for seeing me through these last four years.

Table of Contents

List of Figures	vi
Terminology and notation	vii
1 Multiscale modeling of interfaces: main themes	1
1.1 Vicinal surfaces: free-boundary perspective	6
1.2 Block-copolymers: phase-field perspective	8
I Free-boundary model of vicinal surfaces	11
2 Preliminaries: stochastic, lattice-gas description of surfaces	12
2.1 General framework	13
2.2 Kinetic Monte Carlo approach	16
2.2.1 Example of a 1+1D algorithm	17
2.2.2 Simulation results	23
2.3 Processes affecting the transition rates	26
2.3.1 Classical elastic effects	27
2.3.2 Quantum mechanical effects: RKKY interaction	28
3 Coarse-graining the atomistic model: Burton-Cabrera-Frank theory	32
3.1 Key ideas of the derivation	33
3.1.1 A 1+1D Burton-Cabrera-Frank-type model	36
3.1.2 Our derivation in the context of past works	37
3.2 Terminology and notation	39
3.3 Atomistic, kinetic Monte Carlo master equation	41
3.3.1 General case: the m-particle model	41
3.3.2 An example: the 2-particle model	43
3.3.3 M-particle model as a BBGKY-type hierarchy	44
3.3.4 1-p model	45
3.4 Averaging the 1-particle model: physics of step-flow	47
3.4.1 1-particle equilibrium solution: notion of averaging	48
3.4.2 Evolution laws for averaged quantities	50
3.4.3 Maximum principle for 1-particle model	52
3.5 Derivation of a Burton-Cabrera-Frank-type model	53
3.5.1 Averaging: definitions of step position and adatom density	54
3.5.2 Discrete Burton-Cabrera-Frank equations	55
3.5.3 Maximum principle for the m-particle model	60
3.5.4 Continuum limit of the m-particle model	62
3.6 Discussion	64
3.6.1 Comparison with real material parameters	65
3.6.2 Consequences of dimensionality	67
3.6.3 Limitations of the atomistic model	69

3.7	Summary	70
4	Terrace-width fluctuations: stochastic Burton-Cabrera-Frank model	72
4.1	Key ideas	73
4.2	Burton-Cabrera-Frank model of interacting steps	76
4.2.1	Deterministic equations	76
4.2.2	Interpretation of the interaction parameter	80
4.2.3	Stochastic equations	81
4.2.4	Form of noise: relation to a linearized model	81
4.3	Mean-field formalism	84
4.3.1	Mean-field Burton-Cabrera-Frank equations	85
4.3.2	Evolution law for terrace-widths via BBGKY hierarchy	86
4.3.3	Self-consistency equation for the mean field	88
4.4	Mean-field terrace-width distribution	89
4.4.1	Formulation of the asymptotics	89
4.4.2	Zeroth-order approximation and composite expression	91
4.4.3	Time-dependent terrace-width distribution	96
4.5	Discussion	100
4.5.1	Comparison of the mean-field and linearized models	100
4.5.2	Limitations and applications of our approach	102
4.5.3	Open questions	104
4.6	Summary	105
II	Phase-field model of block-copolymers	106
5	Physics of block-copolymers: an unhappy marriage	107
5.1	Leiber-Ohta-Kawasaki phase-field model	109
5.1.1	Microscopic Gaussian-chain model	109
5.1.2	Coarse-graining the Gaussian-chain model	111
5.2	Defining microdomain interfaces via the phase-field model	114
6	Line-edge roughness of block-copolymer microdomain interfaces	116
6.1	Main ideas	118
6.1.1	Background	118
6.1.2	Notation and terminology	120
6.2	Perspective: system geometry and model of fluctuations	120
6.3	Characterizing interface fluctuations	124
6.4	Defining the line-edge roughness	131
6.5	Discussion	135
6.5.1	Line-edge roughness from a mean-field perspective	135
6.5.1.1	Physics of line-edge roughness	135
6.5.1.2	Limitations of the approach	137
6.5.2	Comparison of our results to experiments	137
6.5.3	Comparison of our results to other models	139

6.5.4	Line-edge roughness in a manufacturing setting	141
6.6	Summary	142
7	Conclusion	144
7.1	Summary of main results	144
7.2	Open problems	146
7.3	Closing statements	147
A	Asymptotic calculations of the mean field and terrace-width distribution	149
A.1	Time independent terrace-width distribution and mean field	149
A.2	Approximation of the mean-field variance	152
B	1D kinetic Monte Carlo simulations for terrace-width distribution	155
	Bibliography	159

List of Figures

1	Two views of a vicinal surface	x
2	Block-copolymers	xi
1.1	Example of how the definition of an interface is subjective.	3
2.1	Cartoon of a crystal surface	13
2.2	Stochastic lattice-gas model	18
2.3	Schematic of the system in our 1D kMC simulations	20
2.4	Simulation results for the expected number of adatoms	24
2.5	Simulation results for the adatom flux	26
2.6	Constant energy curves for a hexagonal lattice	31
3.1	One-dimensional Burton-Cabrera-Frank perspective of a vicinal surfaces	38
3.2	Schematic of the 2-p model	43
3.3	Schematic of the 1-p model	46
3.4	Forbidden transitions in our kMC model	57
3.5	Transitions that leave the adatom density unchanged	58
3.6	The effect of step motion on adatom density	58
3.7	Numerical verification of the linear kinetic relations of the Burton-Cabrera-Frank model	65
3.8	Islands in 1D versus 2D	68
4.1	Side and top views of step systems	78
4.2	Steady-state terrace-width distribution	95
4.3	Variance of the terrace-width distribution as a function of dimensionless time	98
4.4	Time-dependent terrace width distribution for fixed intermediate time	99
5.1	Template directed self assembly	108
5.2	The mean field monomer density for lamellar microdomains	115
6.1	Three views of a polymer melt in the lamellar phase	121
6.2	The effect of fluctuation modes on the ground state monomer density	128
6.3	Line-edge roughness in frequency and real space	133
7.1	Scanning-tunneling microscope image of Si(100) surface	146

Table of Acronyms

BBGKY	Bogoliubov-Born-Green-Kirkwood-Yvon	Chapters 3, 4
BCF	Burton-Cabrera-Frank	Part I
BCP	block-copolymer	Part II
CE	composite expression	Chapter 4
FPE	Fokker-Planck equation	Chapter 4
ITRS	International Technology Roadmap for Semiconductors	Chapter 6
kMC	kinetic Monte Carlo	Part I
LER	line-edge roughness	Chapter 6
LM	linearized model	Chapter 4
LOK	Leibler-Ohta-Kawasaki	Part II
m-p	m-particle	Chapters 2,3
MF	mean-field	Chapter 4
PDE	partial differential equation	Parts I,II
PMMA	poly(methyl methacrylate)	Part II
PS	polystyrene	Part II
SAV	sidewall-angle variation	Chapter 6
SDE	stochastic differential equation	Part I
SEM	scanning electron microscope	Part II
SLG	stochastic lattice-gas	Part I
SS	surface state	Chapter 2
SSR	strong-segregation regime	Part II
TDSA	template-directed self-assembly	Part II
TST	transition-state theory	Chapter 2
TWD	terrace-width distribution	Chapter 4
ZO	zeroth-order	Chapter 4

Terminology and notation

As the work contained in this dissertation lies at the interface of physics and applied mathematics, I use notation and terminology from both disciplines. For the benefit of both audiences, I define terms that are used throughout this work. Later, I also define notation that is needed locally in the context of certain chapters. The items in this list appear in roughly the same order as in the main text.

- A *vicinal surface* is a crystal surface that has been cut at some small angle relative to one of its faceting planes. Formally speaking, such surfaces look like staircases of flat *terraces* separated by atomic-height *steps*; cf. Fig. 1 [1].
- A *block-copolymer* (BCP) is a chain of monomers (individual molecules) having the general structure AAA...A-BBB...B, where A and B are different monomers. BCPs form microdomains shown, for example, in Fig. 2 [2]. We refer to the narrow region separating microdomains as the *microdomain interfaces*.
- A *surface state* (SS) is a quantum mechanical Bloch-like state that is localized at the surface of a crystal. One or more electrons can occupy a surface state, and in doing so, they may interact with the electrons in other atoms on the surface. The SS energy $E(\mathbf{k})$ is typically parameterized by a 2D momentum \mathbf{k} . A surface-state *band structure* is a set of surface state energies $E(\mathbf{k})$. For most metals at room temperature, electrons will fill the surface states up to some energy ϵ_F , called the *Fermi energy* [3, 4].

- The *Fermi function* is defined to be $F(E) = \{\exp[(E - \epsilon_F)/k_B T] + 1\}^{-1}$, where ϵ_F is the Fermi energy and $k_B T$ is the temperature in units of energy. For the applications considered here, the Fermi function is the expected number of electrons in a state with energy E [5].
- In the *Bogoliubov-Born-Green-Kirkwood-Yvon (BBGKY)* hierarchy of non-equilibrium statistical mechanics, the n -particle joint probabilities includes dependence on the n -particle joint probabilities, thereby forming a coupled chain of equations [6].
- Loosely speaking, *line-edge roughness (LER)* is the waviness of an interface.
- The terminology 1+1D means one spatial dimension and one time-like dimension. Similarly, 2+1D means two spatial and one time-like dimension. I use 1D and 2D to refer to one and two spatial dimensions, respectively.
- The adjective *semi-infinite* means that a spatial variable is bounded on one side but allowed to extend to infinity on another; e.g. $x \geq 0$ is a semi-infinite domain.

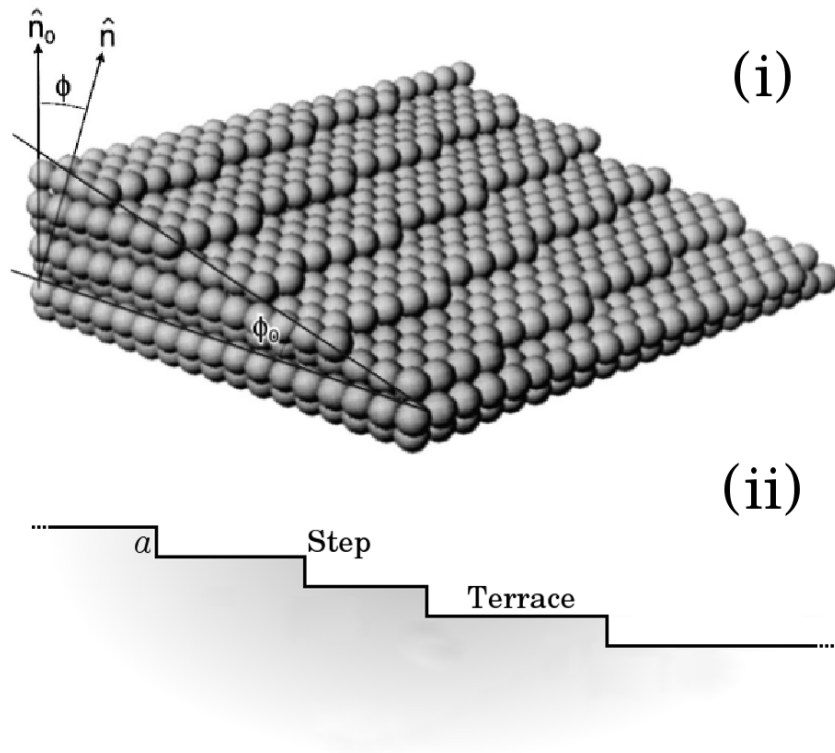


Figure 1: Two views of a vicinal surface. (i) The crystal is cut at some angle relative to one its faceting planes, which creates a staircase-like structure consisting of terraces and steps. Used with permission from Ref. [7]. (ii) A side view of the surface (atoms not shown for clarity).

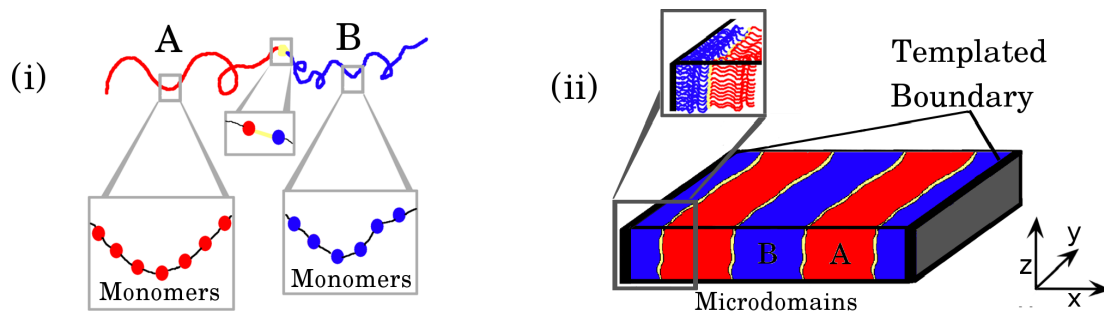


Figure 2: Block-copolymers. (i) A single block-copolymer with A (red) and B (blue) subchains. Insets show that the subchains are made of individual monomers (red and blue dots) connected in sequence. The yellow bond (middle inset) shows where the A and B subchains are connected. (ii) Lamellar BCP microdomains on a templated substrate. Note that the BCPs are small relative to the system size (inset). The yellow regions separating microdomains are the microdomain interfaces.

Chapter 1

Multiscale modeling of interfaces: main themes

The study and characterization of crystal and polymer interfaces is an important task in material science, physics, and applied mathematics. In surface physics, for example, the study of steps (atomic-height defects that separate nanoscale terraces on a surface, cf. Fig. 1) has led to advances in crystal growth and generated interesting classes of free boundary problems and partial differential equations (PDEs) [8, 9]. And in the lithography community, companies such as Intel and IBM are actively devoting resources to determine whether block-copolymer (BCP) microdomains can be used in nanomanufacturing of the next-generation microprocessors [10–14] (cf. Fig. 2).

A key task that arises in each of these contexts is to formulate an appropriate analytic description of the system. On a microscale, the evolution and morphology of an interface is determined by the motion of and interactions between individual atoms. But for many applications, one is interested in features that are hundreds of times (or more) larger than the basic elements of the system, which renders atomistic approaches computationally prohibitive. Consequently, a hierarchy of models have been developed to describe polymer and crystal interfaces at many different length scales.

The goal of this dissertation is to describe my work on multiscale modeling

of interfaces on crystal surfaces and BCPs. In particular, I focus on two distinct systems: steps on vicinal surfaces and microdomain interfaces in BCP melts. In the context of these applications, I address three related questions.

1. What is an interface; e.g. how do we define it in the context of experimental data or a microscopic model?
2. How do we formulate a corresponding interface model that is consistent with a set of appropriate first principles?
3. What information about the interface can we extract from such a model?

Despite seeming straightforward, the first question is often conceptually the most difficult to answer. Naively, one might propose that an interface is the boundary between two “phases” (e.g. two terraces on a vicinal surface). But microscopically a system is composed only of atoms or molecules, not phases; interfaces are not intrinsic elements of the system. Moreover, experiments often yield results in terms of pixel data or statistical ensembles, both of which require interpretation in order to identify an interface (cf. Fig. 1.1). Hence, I take the viewpoint that the definition of an interface is subjective and depends on what information one wishes to extract from the underlying microscopic perspective. Defining an interface in terms of a microscopic theory is therefore a critical first task that must be addressed *with respect to some application or experimental data*.

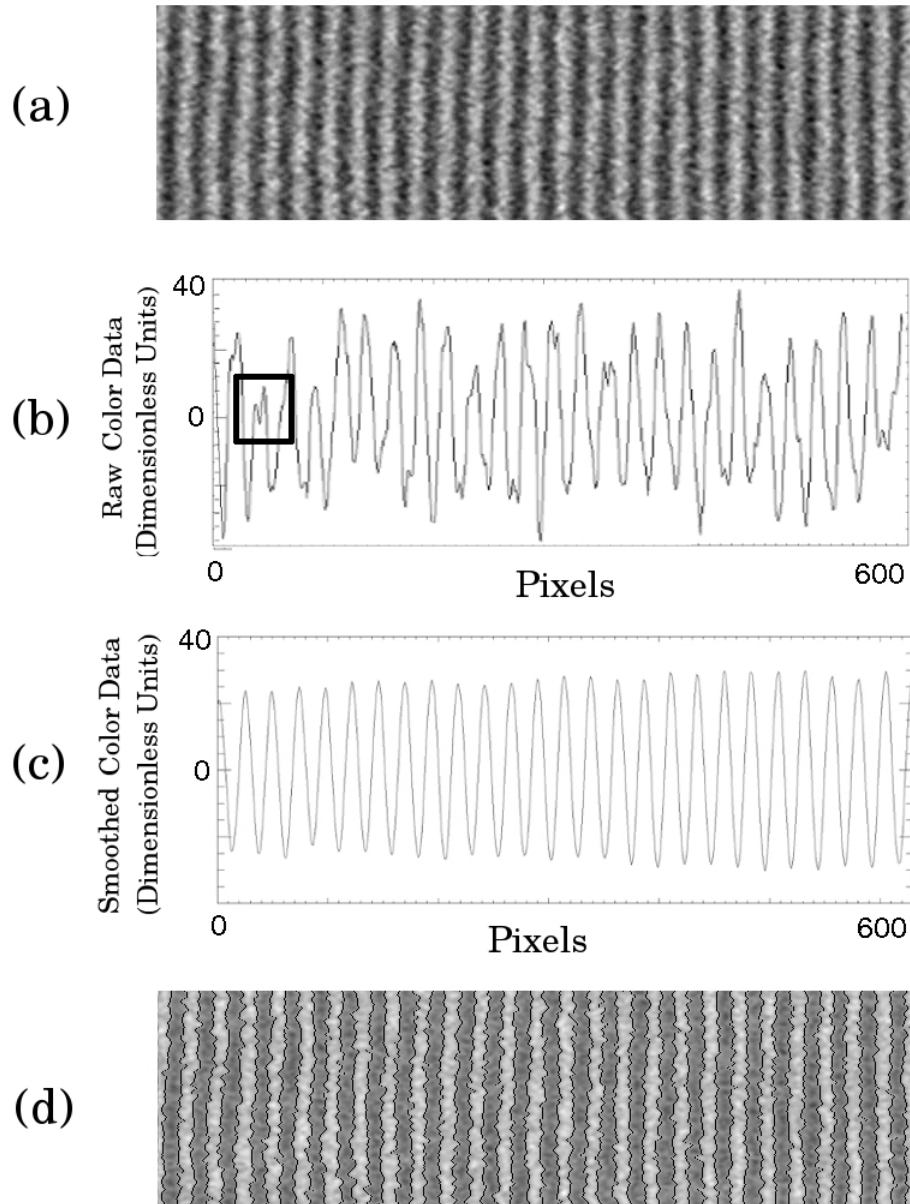


Figure 1.1: Example of how the definition of an interface is subjective. (a) A top-down, scanning electron microscope (SEM) image of BCP microdomains (white and black). Individual microdomains are roughly 8 nm wide. In applications to lithography, one wants to determine the line-edge roughness, or waviness, of the interface separating the white and black microdomains. But given this pixel data, how does one define the interface positions? (b) Raw pixel data for some row of the image. Positive values correspond to whiter pixels, and negative values correspond to blacker pixels. It is tempting to define the interfaces as the locations where the color data changes

sign. However, within the highlighted box, the color data crosses zero twice within the span of a few pixels; we do not expect that these crossings correspond to actual interfaces. (c) The pixel data after applying a filter in Fourier space. Note that the double zero crossing has disappeared in the pixel data. We now take the interface positions to correspond to the zeros of the filtered pixel data. (d) Interfaces drawn on the original image according to the interpretation of (c). Notably, we could have used a different procedure (besides application of a Fourier filter) to determine the interface positions. Images (a) and (d) are adapted with permission from [15]. Copyright 2010, American Chemical Society.

The second question (how do we formulate an appropriate interface model?) is addressed via a coarse-graining procedure. The details of this procedure, as well as the resulting model, depend on the definition of the interface and the length scale that one wishes to describe. For the applications motivating this work, the relevant physics takes place at the *mesoscale*, i.e. in intermediate-sized domains containing tens of interfaces or more. In the case of vicinal surfaces, we derive a free-boundary model based on the Burton-Cabrera-Frank (BCF) theory, which allows us to account for the motion of discrete steps while coarse-graining the diffusion of adsorbed atoms on terraces [16]. In block-copolymer systems, we adopt a phase-field approach, originally derived by Leibler, Ohta, and Kawasaki (LOK), that accounts for microdomain interfaces with some finite width where distinct polymer species mix [17,18].¹

The third question (what information can be obtained from the coarse-grained models?) is often technically the most difficult to answer since it involves actually solving a free-boundary or phase-field model. In the context of the aforementioned

¹Phase-field models have also been used to describe steps on vicinal surfaces, although we do not follow that approach here; see Refs. [19–21].

models, we are primarily interested in the morphological structure of the interfaces, i.e. how they are oriented relative to one another and what their individual shapes are. More generally, the mesoscopic models that we invoke are useful for understanding how interfaces interact with one another, since we consider domains with multiple interfaces.

By its very nature, multiscale modeling of interfaces creates its own set of limitations. In seeking to bridge different length scales, the starting microscopic model must often be sufficiently simple to allow for the derivation and analysis of an appropriate coarse-grained model; even then, asymptotic approximations are frequently invoked to render the mathematics tractable. Importantly, however, the use of asymptotics also yields simple interpretations of the physical processes affecting a system. An important theme of this research is therefore to show how asymptotics are an invaluable tool in the analysis of multiscale models.

While the systems (steps and BCP microdomains) treated in this dissertation differ in many regards, I consider them together because they are both current topics on which I have worked. In particular, the problems discussed herein characterize my interests in both academic and industrial research. But more fundamentally, crystals surfaces and BCP melts represent two different classes of condensed matter systems – hard and soft. In retrospect, these systems (and our analysis of them) can therefore also be thought of as prototypical examples that inform more complicated problems in condensed matter physics.

The rest of this dissertation is organized as follows. In the next two sections, I introduce applications of multiscale modeling to vicinal surfaces (Sec. 1.1) and

block-copolymers (Sec. 1.2). The remainder of the text is separated into two parts.

Part I (Chapters 2–4) focuses on vicinal surfaces. In Chapter 2, I first give an overview of the stochastic lattice-gas (SLG) description of surfaces. Chapter 3, shows how a 1+1D BCF-type model can be derived from a simple version of the SLG model considered in Chapter 2. In Chapter 4, I use a stochastic version of the BCF model to calculate the terrace-width distribution (TWD) of a vicinal surface in 1+1D.

Part II (Chapters 5–7) focuses mainly on block-copolymer systems. In Chapter 5, I provide a brief background on the Gaussian-chain model and the coarse-graining method used by Leibler, Ohta, and Kawasaki to derive their phase-field model. In Chapter 6, I show how the phase-field approach can be used to determine the line-edge roughness (LER) of BCP microdomain interfaces. Chapter 7 provides an overall summary of Parts I and II and discusses open problems.

The topics considered in this dissertation are based on several of my papers that were published in the past four years. In Part I, Chapters 2–3 are based loosely on a combination of Refs. [22, 23], while Chap 4 is based on Ref. [24]. Related works not covered in this dissertation include Refs. [25–27]. In Part II, Chapter 6 is based on work in Refs. [28, 29]. Related works not covered include Ref. [30].

1.1 Vicinal surfaces: free-boundary perspective

Vicinal surfaces are important for a variety of applications, including (for example) step-flow growth of crystals [8] and the nanofabrication of biosensors [31]. Moreover, vicinal surfaces exhibit a wide range of evolution behavior on length and

time scales that are readily observable, making these systems excellent candidates for the study of fluctuations and non-equilibrium statistical mechanics [9]. In each of these cases, nanoscale defects (e.g. steps separating terraces) are the key elements that render the system useful or interesting [1, 8] (cf. Fig. 1). Mesoscale models, which resolve many defects while retaining some atomistic elements of the system, are therefore important means of studying the evolution of surfaces.

An important first task in mesoscale modeling of surfaces is to say what we mean by a step. In many studies, experimentalists take several measurements of a *microscopic* step position or terrace width (quantities that they define in the context of their experiments) and then extrapolate the corresponding expectation values and probability densities [32–36].

We adopt a similar approach. Specifically, we consider a 1+1D stochastic lattice-gas (SLG) model that treats the system probabilistically; atoms move in random directions with probabilities that account for changes in the system energy. The *microscopic step position* is then defined as the location of the atom whose in-plane neighbors on one side have two in-plane nearest neighbors.² We define the *mesoscopic step position*³ as the ensemble average of the corresponding microscopic position. By invoking the SLG model, we also show that motion of this average is described by a version of the free-boundary model originally pioneered by Burton, Cabrera, and Frank [16, 23].

²Interestingly, we believe that the task of defining a step has never before been done analytically.

³In 1+1D, this definition excludes the possibility of holes on the surface. This restriction on our model is a consequence of the dimensionality of the system; see Chapter 3.

The free-boundary perspective that we invoke permits us to study questions related to the evolution of multiple, interacting steps. In particular, several works suggest that steps can interact via entropic forces and elastic dipoles that yield non-linear boundary conditions at the step edges [37–39]. Moreover, the introduction of a suitable noise to the BCF model yields a stochastic free boundary problem that can address questions of how thermal noise competes with step interactions to yield a terrace-width distribution (TWD) [24, 26, 40, 41]. The TWD can be used, for example, to understand how uniform a surface is expected to be, and it also provides information on the strength of step interactions [42, 43].

While the presentation of Part I covers the derivation and applications of BCF-type theories, we emphasize that the analysis contained therein leaves many open questions and problems. In particular, the models considered are all 1D. Many questions therefore remain about how to generalize the derivations and results to 2+1D systems, where the curvature of steps plays an important role in the system evolution. Moreover, our derivation of the BCF-type model applies only to a single step. While we believe that the analysis can be generalized to systems with many steps that interact (see Chapter 3), this remains an open problem.

1.2 Block-copolymers: phase-field perspective

In recent years, interest in self-assembling block copolymers (BCPs) has increased dramatically, due in large part to their potential applications in the semiconductor industry [10–14]. One of the key properties that makes BCPs promising

is their ability self-assemble into microdomains whose size, shape, and spacing are the same as or smaller than features found in modern microprocessors [44–47] (cf. Figs. 2 and 1.1). Because this self-assembly process is so crucial to high-fidelity pattern transfer in lithography, it is important to understand the thermodynamic limitations of BCPs; specifically, how much intrinsic line-edge roughness (LER) will the microdomain interfaces express? In Part II of this dissertation, my goal is to show how phase-field models can be used to address this question.

In polymer systems, it is difficult to define the microdomain interfaces in the same manner as for vicinal surfaces, i.e. as corresponding to a specific lattice site. This is a consequence of the fact that BCPs can fold and wrap around one another to form complicated microscopic geometries (cf. Fig. 2). As a result, the regions separating the A and B microdomains generally have some finite width where the different monomer species intermingle (see e.g. Ref. [18]). As in Part I, however, our definition of an interface should be motivated by some application or experimental data. For BCPs, Fig. 1.1 is representative of how an experimentalist might approach this question, i.e. by defining the interface position to be the zero crossing of pixel data (after some appropriate analysis of the image). Importantly, this perspective is consistent with our notion that the BCP interface should have a finite width.

This example therefore motivates a phase-field approach to modeling BCP interfaces. Specifically, we model the BCP melt through a continuous density whose value changes quickly in the interface region. Leibler, Ohta, and Kawasaki derived such a phase-field model of BCPs by coarse-graining a Gaussian-chain model of polymers [17,18]. The LOK model gives the energy of the system as a functional of

the relative density of monomers. For simple systems, the (approximate) minimizer of this functional has a boundary layer of finite thickness where the monomer density transitions from one species to another.

Our approach for determining the BCP morphology is variational. In solving for the LER, we propose a trial minimizer of the LOK functional and then determine the energy of fluctuations around that minimizer. Importantly, the boundary layer in the original LOK solution (on which our trial function is based) implies the presence of a small parameter – the interface width – in the theory, which allows us to construct approximation schemes for the BCP morphology and fluctuation spectrum.

As is the case for Part I of this dissertation, Part II leaves many open questions. In particular, the coarse-grained LOK functional is a mean-field model that makes many simplifying assumptions about the microscopic nature of the block-copolymers; it is not completely known how these approximation limit the theory. Moreover, solutions to the phase-field model can often only be found for BCP geometries and systems that are simpler than those that are of interest to industry.

Part I

Free-boundary model of vicinal surfaces

Chapter 2

Preliminaries: stochastic, lattice-gas description of surfaces

In principle, a complete description of surface evolution requires the full machinery of quantum mechanics; in practice, such treatments are virtually intractable owing to the complexity of even the simplest looking systems. Consequently, approximate theories, based on a combination of first principles and physical insight, have been developed in order to describe surface evolution at the atomic scale.

In this chapter, I consider one such theory, a stochastic, lattice-gas (SLG) model that treats the motion of atoms as probabilistic hopping events. The goal of this discussion is to establish an atomistic framework from which we can derive the BCF theory; in essence, we take the SLG model to be our “set of appropriate first principles.” Importantly, we will use this framework to formulate a definition of a *microscopic* step in the context of a 1+1D system; this definition is motivated by experimental measurements cited in Sec. 1.1.

This chapter is organized as follows. In Sec. 2.1, I lay out the basic ideas of the SLG model. In Sec. 2.2, I give a kinetic Monte Carlo (kMC) representation of the SLG model and show how the former can be used to extract information from the latter. In Sec. 2.3, I consider how the SLG model can be expanded to account for elastic and quantum interactions found in particular material systems.

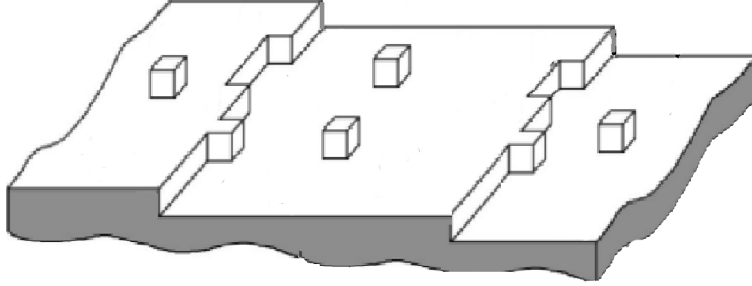


Figure 2.1: Cartoon of a crystal surface. Terraces are separated by steps. Adsorbed atoms (adatoms) cover a small fraction of the surface. Vacancies are not illustrated.

2.1 General framework

At the nanoscale, crystal surfaces are composed of atoms in a periodic array of lattice sites. Depending on how the atoms are arranged, a surface is composed of one or more terraces (perpendicular to some principal crystallographic axis) separated by discrete, atomic heights. Adsorbed atoms (adatoms) and islands (small clusters of adatoms) often cover some fraction of the terraces; cf. Fig. 2.1. These adatoms may hop between lattice sites, and over time, the combined effect of many such transitions will lead to larger scale morphological changes of the crystal [1, 8].

The goal of a SLG model is to capture this evolution by accounting for the hopping transitions of individual atoms. Mathematically, it achieves this goal by describing the time evolution of the joint probabilities of finding the system in one of its atomistic configurations. Our SLG model combines elements from two distinct areas: the lattice-gas model of surfaces and transition-state theory (TST).

The lattice-gas model is a way to represent the energy of a surface. The key idea is to assume that every atom in the system shares a separate bond with each

of its nearest neighbors.¹ The total energy of the system is simply the sum of the (negative) energies of all bonds [48]. If we let \mathbf{a} represent a configuration of atoms, then by Boltzmann statistics we may write

$$P_{\text{eq}}(\mathbf{a}) \propto \exp \left[- \sum_b E_b(\mathbf{a})/k_B T \right] \quad (2.1)$$

where $P_{\text{eq}}(\mathbf{a})$ is the equilibrium joint probability of finding the atoms in configuration \mathbf{a} , $k_B T$ is the temperature in units of energy, and b indexes the (negative) bond energies $-E_b(\mathbf{a})$ ($E_b > 0$), which are functions of \mathbf{a} [48]. In order to simplify the space of possible configurations \mathbf{a} , atoms typically are treated as rigid blocks that may only be found at the centers of each lattice site.² Under this restriction, it is reasonable to assume that $E_b(\mathbf{a}) = E_b$ is constant. Note that we will often refer to \mathbf{a} as a *system state*; we also refer to hopping events as changes in the system state.

While the lattice-gas model gives us the equilibrium properties of the surface, transition-state theory is used to account for its time evolution. Specifically, TST provides the rates $\mathcal{T}_{\mathbf{a} \rightarrow \mathbf{a}'}$ at which the system transitions from state \mathbf{a} to state \mathbf{a}' (i.e. the rates at which adatoms hop on the surface) [49–51]. Here our goal is to represent the surface evolution using a master equation of the form

$$\frac{dP(\mathbf{a}, t)}{dt} = \sum_{\mathbf{a}' \neq \mathbf{a}} P(\mathbf{a}', t) \mathcal{T}_{\mathbf{a}' \rightarrow \mathbf{a}} - \sum_{\mathbf{a}' \neq \mathbf{a}} P(\mathbf{a}, t) \mathcal{T}_{\mathbf{a} \rightarrow \mathbf{a}'}, \quad (2.2)$$

where $P(\mathbf{a}, t)$ is the probability of finding the system in state \mathbf{a} at time t [52–55].

¹This assumption ignores long-range elastic and quantum interactions, which are typically weaker than direct bonding between atoms; cf. Sec. 2.3.

²The shape of the adatoms in an SOS model actually depends on the underlying substrate. Here we only consider a simple cubic lattice.

The key assumptions that TST uses to determine the transition rates are that (i) the adatom must overcome a positive energy barrier $E_{\mathbf{a}\rightarrow\mathbf{a}'}$ in order to move to another lattice site, and (ii) before hopping, a Boltzmann distribution describes the probability that the adatom has energy E .³ TST then posits that the transition rate is given by the expression

$$\mathcal{T}_{\mathbf{a}\rightarrow\mathbf{a}'} = f \exp[-E_{\mathbf{a}\rightarrow\mathbf{a}'}/k_B T], \quad (2.3)$$

where f is an attempt frequency [49–51]. For applications in surface physics, f is usually taken to be 10^{13} s^{-1} [8].

The task of formulating a stochastic lattice gas model therefore amounts to establishing an appropriate set of energy barriers $E_{\mathbf{a}\rightarrow\mathbf{a}'}$ associated with hopping events. A convenient and often used choice is to assume

$$E_{\mathbf{a}\rightarrow\mathbf{a}'} = E_h + \max\{E_{\mathbf{a}'} - E_{\mathbf{a}}, 0\}, \quad (2.4)$$

where $E_h > 0$ is a hopping or diffusive barrier (see e.g. [27, 43, 52, 53] for related examples). For the simple bond counting model described above, the term $\max\{E_{\mathbf{a}'} - E_{\mathbf{a}}, 0\}$ is simply proportional to the number bonds that must be broken for the transition to happen. Physically, Eq. (2.4) is useful because it satisfies detailed balance. That is, in equilibrium,

$$P_{\text{eq}}(\mathbf{a})\mathcal{T}_{\mathbf{a}\rightarrow\mathbf{a}'} = P_{\text{eq}}(\mathbf{a}')\mathcal{T}_{\mathbf{a}'\rightarrow\mathbf{a}}. \quad (2.5)$$

This condition in particular is necessary for a system in equilibrium to remain so [54].

³That is, we assume that the adatom is *locally* in equilibrium with the surface. Note that this is different from the statement that the *entire* system is in equilibrium.

The assumption that the adatom is in equilibrium with the surface relies on a separation of timescales argument. Namely, hopping transitions are rare-events when compared with the attempt frequency f . Heuristically, one can imagine that the adatom position fluctuates around an energy minimum (corresponding to the lattice site) for so long that the particle loses any memory of its previous state. See Ref. [56] for a discussion of this point.

The SLG view of transitions, while useful, oversimplifies many aspects of adatom diffusion. In particular, TST assumes that an adatom always hops to another lattice site if it has enough energy to do so. However, in real systems energy barrier recrossing events are possible [56]. Moreover, adatoms with sufficient momentum (a quantity that is not treated at all in TST) may have sufficient energy to travel several lattice sites before finally sticking to a particular site. Nonetheless, the SLG model of surfaces is useful for describing systems out of equilibrium, as evidenced by the numerous works that solve such models using kMC approaches; see e.g. works by the authors of Refs. [43, 56–61].

2.2 Kinetic Monte Carlo approach

In the previous section, we described the main ideas of an SLG model. In this section, our goal is to give an example of an SLG model, which we solve by means of kinetic Monte Carlo (kMC) simulations. Throughout this section, we consider a single step (which we define) in 1+1D; this model serves as the starting point for our derivation of the BCF theory in the next chapter. This exposition is divided

into two subsections. In Sec. 2.2.1, I outline the simulation algorithm and describe the main ideas of our kMC approach; and in Sec. 2.2.2, I discuss some numerical results.

2.2.1 Example of a 1+1D algorithm

We consider a bond-counting, SLG model described in Sec. 2.1. Instead of solving Eq. (2.2) directly, we use a computer to follow many (10^8) realizations of the statistical ensemble underlying the probabilities $P(\mathbf{a}, t)$. Given enough realizations, we are able to approximately reconstruct the probabilities $P(\mathbf{a}, t)$ and their moments.

For a given realization, the system evolves by means of hopping events in which a single atom is chosen at random to move to an adjacent lattice site. The probability with which an atom is picked is given in terms of a transition rate $D e^{-E_b n / k_B T}$, where D is the hopping rate for adatoms with no in-plane nearest neighbors, E_b is a bond energy, and n is the number of in-plane nearest-neighbor bonds that the moving particle breaks. The parameters E_b and D are material dependent, whereas the temperature T is adjustable. The set of transition rates and initial probabilities are sufficient to determine the probabilities of any configuration at any later time [8, 56, 62, 63].

As an example, we consider a 1D surface with N semi-infinite height columns, which are each one atomic length a wide. These columns are indexed by j , where $0 \leq j \leq N - 1$; 0, 1, or more atoms may reside in each column. If \mathbf{m} atoms are in the same column, they form a stack (starting from the column base) that is \mathbf{m} atomic

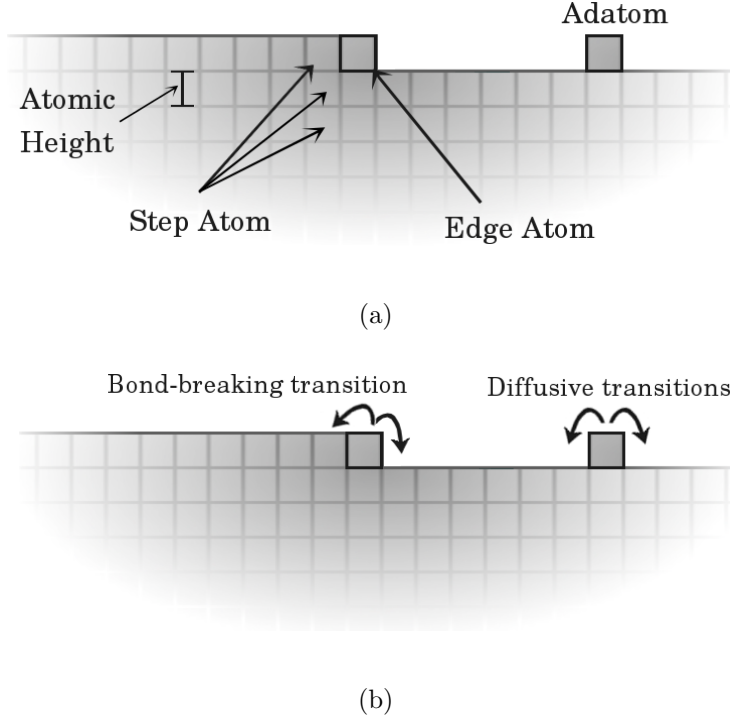


Figure 2.2: (a) SLG perspective of a 1D surface. Atoms, confined to a lattice, are the only elements of the model; they are classified according to the number of in-plane nearest-neighbor bonds that they have. In this perspective, the step is not an intrinsic element of the model, but must be defined in terms of adatom configurations. (b) Transitions in a kMC model. In our formulation, only adatoms and edge atoms are allowed to move, corresponding to the diffusive and bond-breaking transitions illustrated above.

lengths high (cf. Fig. 2.3). Thus, the coordinates j and \mathbf{m} define a 2D grid, and the number of atoms on any square of that grid is either 0 or 1. We impose screw periodic boundary conditions in the j direction; e.g the coordinate $(j, \mathbf{m}) = (N - 1, \mathbf{m})$ is directly to the left of $(j', \mathbf{m}') = (0, \mathbf{m} + 1)$. In other words, if an adatom hops to the right from the $(N - 1)$ th height column, it arrives at the 0th height column. We henceforth refer to the height columns indexed by j as lattice sites.

We take the total number of atoms to be $\mathcal{O}(N)$. These atoms are grouped

into one of three classes: step atoms, edge atoms, and adatoms, defined as follows [cf. Fig. 2.2(a)].

Definition 2.2.1 *A step atom has the properties that (i) it has two in-plane nearest neighbors, and (ii) all atoms to its left (taking into account the screw periodic boundary conditions) have two in-plane nearest neighbors.*

Definition 2.2.2 *An edge atom has the properties that (i) it has only one in-plane nearest neighbor, which is to its left, and (ii) all atoms to its left (taking into account the screw periodic boundary conditions) have two in-plane neighbors.*

Definition 2.2.3 *An adatom is a particle that is neither a step atom nor an edge atom.*

All atoms in a given class are otherwise indistinguishable. We place an immobile atom directly to the left of $(j, m) = (0, 1)$ so that an atom at $(0, 1)$ is always either an edge or step atom.

We define the terrace and *microscopic* step position $s(t)$ in terms of the atomistic configuration:

Definition 2.2.4 *A terrace site is any lattice site that is not directly to the right to an edge atom; see Fig. 2.3.*

Definition 2.2.5 *The microscopic step position $s(t)$ is the lattice site (i.e. height column) where the edge atom is found (cf. Fig. 2.3). We denote s_0 as the location of the step when all atoms are step or edge atoms, i.e. when there are no adatoms on the surface.*

We say that an adatom attaches to a step when it moves to the lattice site directly to the right of an edge atom; this adatom then becomes an edge atom. We say that an edge atom detaches from the step and becomes an adatom when it moves to either of its adjacent lattice sites; see Fig. 2.2(b). Because of the immobile edge atom left of $(j, \mathbf{m}) = (0, 1)$, the step cannot retreat indefinitely.

The state of the system is uniquely determined by the position of all *adatoms*, and the system transitions from one state to another when one of three events happens: (i) an adatom moves; (ii) an edge atom detaches from the step; or (iii) an adatom attaches to the step. Whenever an edge atom detaches from (or an adatom attaches to) the step, the step site moves to the left (right) by one lattice site.

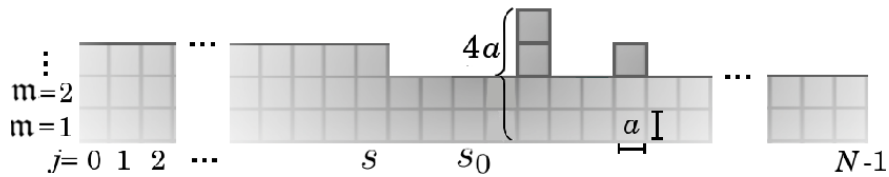


Figure 2.3: Schematic of the system in our 1D kMC simulations. The index j , $0 \leq j \leq N - 1$, labels height columns, and the index \mathbf{m} labels height, $\mathbf{m} \geq 1$. Each ordered pair (j, \mathbf{m}) corresponds to a square whose sides are an atomic length a . At most one atom may occupy any such square. There are three adatoms on the surface. The microscopic step position is denoted s (cf. Def. 2.2.5).

We describe our kMC algorithm through the following set of rules.

Rule 2.2.1 *An atom is only allowed to move horizontally a distance of one lattice site during a single time step; the stack from which (to which) the atom moves changes in height by $-a$ ($+a$).*

Rule 2.2.2 *An adatom hops from a terrace site to any adjacent terrace site with a probability proportional to a constant rate D (described below), independent of the number of adatoms occupying the ending sites.*

Rule 2.2.3 *An adatom hops from the left (-) or right (+) of the step to the site directly to the right of the step with probability proportional to an attachment rate $D\phi_{\pm}$ [defined in (2.6)], provided the process only creates a single step atom.*

Rule 2.2.4 *An edge atom is allowed to detach from a step to the left (-) or right (+) with probability proportional to a detachment rate $Dk\phi_{\pm}$ [defined in (2.6) and (2.7)], provided the process converts a single step atom into an adatom.*

Rule 2.2.5 *Processes that create more than one step atom or adatom are forbidden.*

The parameter D is the hopping transition rate, i.e. the inverse of the expectation time for an adatom to hop on the terrace. The parameters k and ϕ_{\pm} are the Arrhenius factors that account for the extra time needed to break a bond and attach to a step, respectively. We assume that

$$\phi_{\pm} = e^{-E_{\pm}/k_B T}, \quad (2.6)$$

$$k = e^{-E_b/k_B T}, \quad (2.7)$$

where $E_{\pm} \geq 0$ and $E_b > 0$ are the attachment and bond energy barriers, respectively; E_- is sometimes referred to as the ‘‘Ehrlich-Schwoebel barrier’’ [64,65]. Each of these barriers can be up to a few tenths of an eV, so that for temperatures up to roughly 1000 K, the values for ϕ_{\pm} and k can range from 10^{-1} to 10^{-6} or smaller, depending

on the material. See Refs. [56, 66, 67] for a discussion on the physical assumptions underlying D , ϕ_{\pm} , and k , as well as Sec. 3.6.1.

In practice, Rules 2.2.1-2.2.5 are implemented by a computer using random number generators. Given a starting configuration, a single particle (from the allowed set) is moved with a probability proportional to its transition rates. The amount of simulation time attributed to each individual process is chosen randomly from a Poisson distribution whose mean is the inverse of the transition rate for that process [56, 66]. Iterating this algorithm evolves the system. For each set of parameters E_{\pm} , E_b , and T , we run about 10^8 simulations and calculate (i) the average microscopic step position (cf. Def. 2.2.5), (ii) the average number of adatoms j sites away from the step (for $1 \leq j \leq N - 1$), and (iii) the average number of adatoms attaching to the step per unit time from the right (i.e. the average flux to the right of the step). Each realization begins in an initial configuration in which all atoms are attached to the step.

Remark 2.2.1 The probabilities of finding the system in an atomistic configuration are expected to numerically converge to an equilibrium Boltzmann distribution in the long-time limit; that is, the probability of finding a state with m adatoms is proportional to $\exp[-mE_b/k_B T]$ when $t \rightarrow \infty$. See, e.g., Ref. [68] for a discussion on how kMC simulations approach equilibrium.

In Sec. 2.2.2, we present numerical results of kMC simulations that suggest a correspondence between the kMC and BCF models.

Remark 2.2.2 Rule 2.2.2 amounts to neglecting the bonds between adatoms. In 1D, the presence of nearest-neighbor adatom bonds can lead to steady states in which the probability of an island nucleating is independent of its size. However, in 2D, Boltzmann statistics for a kMC scheme show that large islands are less probable than small islands (see Sec. 3.6.2). Our assumption that adatoms do not interact is meant to render the analysis of the next chapter more consistent with 2D systems while avoiding subtleties associated with nucleation in 1D. See Sec. 3.6.2 for a discussion of this issue; and Refs. [69, 70] for works related to nucleation in 1D.

Remark 2.2.3 Rules 2.2.3–2.2.5 imply that a step can never move by more than one lattice site at a time. While this assumption is not necessary for the purposes of the next chapter, it nonetheless simplifies the analysis. See Sec. 3.6.2 for a discussion on variations of the master equation that allow for more general types of step motion.

2.2.2 Simulation results

In Figs. 2.4 and 2.5, we show kMC results for our 1D surface with one step. In all simulations we fixed $k_B T = 1/40$ eV ($T \approx 273$ K), $D = 10^{10}$ s⁻¹, and $N = 50$.

Figure 2.4 shows the average number $n_j(t)$ of adatoms that are j lattices sites away from the step at six successive times. Since the index j is always measured relative to the step (regardless of the number of adatoms on the surface), we set the step position to be $j = 0$. By screw periodic boundary conditions, $j = 0$ and $j = 50$ correspond to the same lattice site.

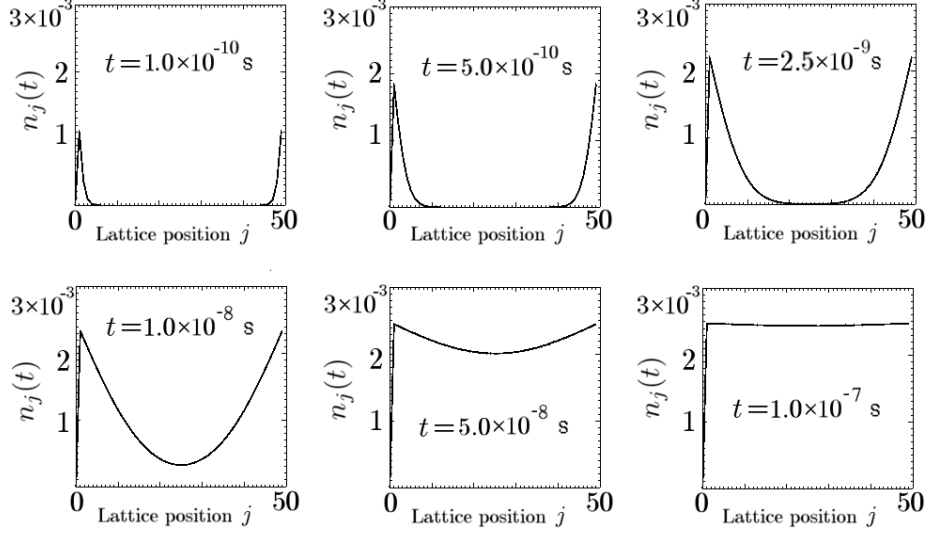


Figure 2.4: Average number of adatoms at a given lattice site, relative to the step, for six different times during a kMC simulation. The system is 50 lattice sites wide, and the step is always taken to be at the zeroth (or leftmost) lattice site. We use $E_b = 0.15$ eV, $E_{\pm} = 0$ eV, $k_B T = 1/40$ eV, $D = 10^{10}$ s $^{-1}$, and $N = 50$. The average number of adatoms directly to the right of the step reaches its equilibrium value fast relative to the timescale over which the system equilibrates. This behavior is reminiscent of diffusion limited kinetics, in which diffusion (as opposed to attachment/detachment) is the slowest process [8].

In Fig. 2.5(a), we plot the flux of atoms to the right of the step versus time. In Fig. 2.5(b), we plot this flux versus the number of adatoms n_1 to the right of the step. We emphasize five important features of Figs. 2.4 and 2.5.

Remark 2.2.4 Figure 2.4 shows that, on average, adatoms detach from a step and diffuse towards the middle of the terrace. At long times the system approaches an equilibrium in which the mean number of adatoms at a particular site is the same for all sites.

Remark 2.2.5 In Fig. 2.5(b), the average flux at the step is approximately linear

in the average number of adatoms n_1 over seven orders of magnitude of flux values. Moreover, the magnitude of the slope of the corresponding curve is of order D , where $D = 10^{10} \text{ s}^{-1}$, i.e. very large compared to $N^2 \text{ s}^{-1}$. We return to this point in Sec. 3.5.4.

Remark 2.2.6 In Fig. 2.5(b), the average flux vanishes when the average number of adatoms at the step goes to k ; cf. Eq. (2.7).

Remark 2.2.7 In Fig. 2.4, the average number of adatoms at the step edge reaches its equilibrium value on a timescale that is much shorter than the time for the system to reach equilibrium. In light of Remarks 2.2.5 and 2.2.6, this behavior is reminiscent of diffusion limited kinetics, meaning that diffusion is the rate limiting processes for the system to reach equilibrium.

Remark 2.2.8 Figures 2.4 and 2.5 show that in equilibrium, the probability of finding an adatom j sites from the step is $n_j(t \rightarrow \infty) \approx k = e^{-E_b/(k_B T)}$. Note that

$$n_j(t \rightarrow \infty) := \sum_{\alpha} \chi(\alpha, j) e^{-E_b n(\alpha)/(k_B T)} \approx e^{-E_b/(k_B T)}, \quad (2.8)$$

where summation is over all possible states α , the total number of adatoms in state α is $n(\alpha)$, and $\chi(\alpha, j)$ is the number of adatoms j sites away from the step for state α . *Since we identify E_b as the energy cost to create a single adatom, we conclude that n_j is dominated entirely by the one-particle states.* This observation is central to the analysis of the next chapter.

In Chapter 3, we will return to each of these remarks and show that they are consistent with predictions of the BCF-type theory that we derive.

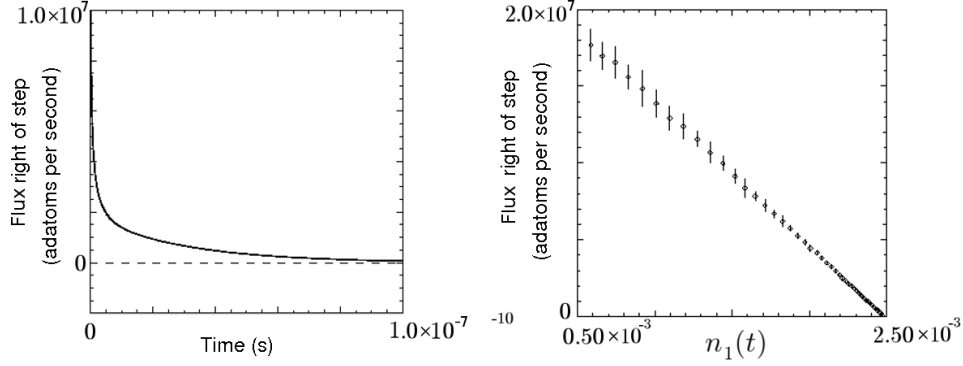


Figure 2.5: (a) Average flux of atoms to the right of the step versus time. Positive values correspond to net detachment of particles. (b) Average flux of atoms to the right of the step versus the probability n_1 of finding an adatom at $j = 1$. We set $E_b = 0.15$ eV, $E_{\pm} = 0$ eV, $k_B T = 1/40$ eV, $D = 10^{10}$ s $^{-1}$, and $N = 50$. Note that for $n_1 \approx k = \exp(-E_b/k_B T)$, the flux of atoms goes to zero. As a function of n_1 , the flux is approximately linear in a certain regime of adatom probabilities.

2.3 Processes affecting the transition rates

The SLG model described in the previous two sections largely ignores long-range elastic and quantum interactions, which are usually dominated by short range bonds or adhesive interactions. However, the formulation of appropriate energy barriers described in Sec. 2.1 only relies on the *differences in energy* between states, not the actual form of the energetic interactions themselves; see Eq. (2.4). Thus, modifying an SLG model to account for long range interactions is in principle straightforward. One need only calculate the energies of the states that the system can sample and determine the transition rates according to the recipe of Eq. (2.4) and Sec. 2.1.

The rest of this section is therefore devoted to a very brief review of a few classes of interactions that are important for many systems. In Sec. 2.3.1, I consider

classical elastic interactions, while in Sec. 2.3.2 I consider surface-state mediated quantum effects.

2.3.1 Classical elastic effects

In classical elasticity theory, it is well known that the mechanical stress caused by an impurity in a bulk crystal can be modeled as a distribution of point forces [71]. In 1980, Marchenko and Parshin extended this idea to account for the interaction energy between defects on a crystal surface [37] (cf. Eq. (2.11)).

The key idea of their approach was to introduce two linear distributions of forces, one normal to the surface (denoted \mathbf{f}_n) and the other in the plane of the surface but perpendicular to the step (denoted \mathbf{f}_x). Mathematically these forces were represented in the form

$$\mathbf{f}_n = \beta a \partial_x \delta(x), \quad (2.9)$$

$$\mathbf{f}_x = \mathbf{f} \partial_x \delta(x), \quad (2.10)$$

where β is a surface tension, a is the atomic spacing, $\delta(x)$ is the Dirac delta function, $x = 0$ is the position of the step, and \mathbf{f} is a free parameter. Classical elasticity theory then predicts that the interaction energy (per unit length) between two steps goes as

$$U(x) = \frac{A[\mathbf{f}^2 + (\beta a)^2]}{x^2}, \quad (2.11)$$

where x is the distance between the (straight) steps and A is a parameter that depends on the elastic properties of the surface [37].

Numerous works have noted the importance of such elastic effects, which can induce step bunching in step trains, for example [72, 73]; see also Ref. [74–76] for a more complete list of other effects. While we do not include such effects in the SLG model of this or the next chapter, we do discuss in Chapter 4 how step interactions can be incorporated into the BCF theory.

2.3.2 Quantum mechanical effects: RKKY interaction

In metallic systems (especially noble metals), electronic surface states (SS) [3, 4] can mediate quantum interactions between atoms on a surface. A simple but important example is the SS-mediated Ruderman-Kittel-Kasuya-Yosida (RKKY) interaction [77–80] between two adatoms, which is believed to be important for the self-assembly of novel structures in heteroepitaxial systems such as Ag on Pt(111) [81–84]. Physically, this interaction describes a process in which an electron associated with the substrate couples (via the Coulomb potential) to the electrons in two adatoms, causing the latter to interact indirectly.

For a 2D surface, the general form of the asymptotic, far-field RKKY interaction is [22, 85]

$$\Delta = -\mathcal{P} \int d^2\mathbf{k} d^2\mathbf{k}' \frac{e^{-i(\mathbf{k}-\mathbf{k}')\cdot\mathbf{R}} |J_{\mathbf{k}\mathbf{k}'}|^2}{E_{\mathbf{k}'} - E_{\mathbf{k}}} F(E_{\mathbf{k}}) [1 - F(E_{\mathbf{k}'})], \quad (2.12)$$

where \mathcal{P} indicates that the integral should be interpreted as a principal value. The vector \mathbf{R} connects the positions of the interacting adatoms. The Fermi function is denoted by $F(E_k)$ (cf. Terminology and notation on p. viii), and E_k is the energy of a SS with the wave vector \mathbf{k} . When multiplied by $F(E_{\mathbf{k}})[1 - F(E_{\mathbf{k}'})]$, the

exchange integral $J_{\mathbf{k}\mathbf{k}'}$ describes a coupling event whereby a SS below the Fermi energy is upscattered to a state above the Fermi energy via an interaction with an adatom; the hermitian conjugate of $[J_{\mathbf{k}\mathbf{k}'}]$ describes the opposite process in which the upscattered SS returns to its original state. The presence of $\exp[-i(\mathbf{k} - \mathbf{k}') \cdot \mathbf{R}]$ reveals that the interaction is mediated by a weighted sum of symmetric and anti-symmetric surface states. Integration runs over all \mathbf{k} in the first Brillouin zone of a single band; we neglect contributions from other bands.

Given a Fermi energy and the dispersion relation for the surface states [i.e. the energy $E(\mathbf{k})$ as a function of the wavevector \mathbf{k} , cf. Fig. 2.6], a stationary phase-approximation can be used to simplify Eq. (2.12) in the far-field limit (when R is large); see Ref. [22] for a full derivation. One finds (after much calculation) that

$$\Delta \approx -2\pi^3 k_B T \frac{|J_{\epsilon_F, \epsilon_F}|^2 \mathbf{n}(\epsilon_F)}{\mathcal{V}_F^2} \frac{\sin(2k_s R)}{\sinh[2\pi k_B T R / \mathcal{V}_F] R} \quad (2.13a)$$

$$\lim_{k_B T \rightarrow 0} \Delta = -\pi^2 \frac{|J_{\epsilon_F, \epsilon_F}|^2 \mathbf{n}(\epsilon_F)}{\mathcal{V}_F} \frac{\sin(2k_s R)}{R^2}. \quad (2.13b)$$

We treat $J_{\epsilon_F, \epsilon_F}$ as a free parameter.⁴ The parameters k_s , $\mathbf{n}(\epsilon_F)$, and \mathcal{V}_F^2 are defined through the following procedure (see also Fig. 2.6). First rotate the coordinate axes by an angle θ such that \mathbf{R} points in the y direction. Next, locate the constant energy curve $E(\mathbf{k}_F) = \epsilon_F$ and find its maximum $\check{\mathbf{k}}_F$ in the rotated coordinate system. Then $k_s = \check{\mathbf{k}}_F \cdot \mathbf{R} / R$; physically k_s is the projection onto the unit vector $\hat{\mathbf{R}}$ of the Fermi wavevector whose Fermi velocity is parallel to \mathbf{R} . The term

$$\mathcal{V}_F = \left(\partial k_y / \partial E \Big|_{\check{\mathbf{k}}_F} \right)^{-1} \quad (2.14)$$

⁴Strictly speaking then, Eq. 2.13 is well defined only for \mathbf{R} , a Bravais lattice vector.

is proportional to the Fermi velocity at $\check{\mathbf{k}}_F$, and

$$\mathbf{n}(\epsilon_F) = \left(-\frac{1}{2} \partial^2 k_y(E, k_x) / \partial k_x^2 |_{\check{\mathbf{k}}_F} \right)^{-1} \quad (2.15)$$

is proportional to the number of electronic SS at $\check{\mathbf{k}}_F$. Equations 2.13a and (2.13b) are valid provided that $R/\mathbf{n}(\epsilon_F) \gg 1$.

Equation (2.13a) illustrates the fact that quantum interactions exhibit anisotropy when the electronic band structure of the lattice is anisotropic. Importantly, SLG models are able to probe the effects of such interactions; see, e.g. Ref. [83]. However, much information can be gleaned from Eq. (2.13b) without the need for simulations. Specifically, when ϵ_F is near the center of the band structure (where there is little anisotropy in $E(\mathbf{k})$), we expect the corresponding RKKY interaction to be relatively isotropic. For ϵ_F near the edge of the first Brillouin zone (e.g. near the dashed lines in Fig. 2.6), anisotropy can be quite significant.

In principle, an adatom can interact via a SS with any other defect (such as a step or island) on the surface, leading to sinusoidal variations in the local density of electronic states (often called Friedel oscillations). Such oscillations can often be seen experimentally at liquid helium temperatures with a scanning tunneling microscope; see for example studies of beryllium [86,87]. Non-pairwise SS-mediated interactions between three or more adatoms can also modify the energy landscape [88–90]. In general, the list of possible interactions can be quite long, and we defer the reader to a general reference on the subject for more details [5,88].

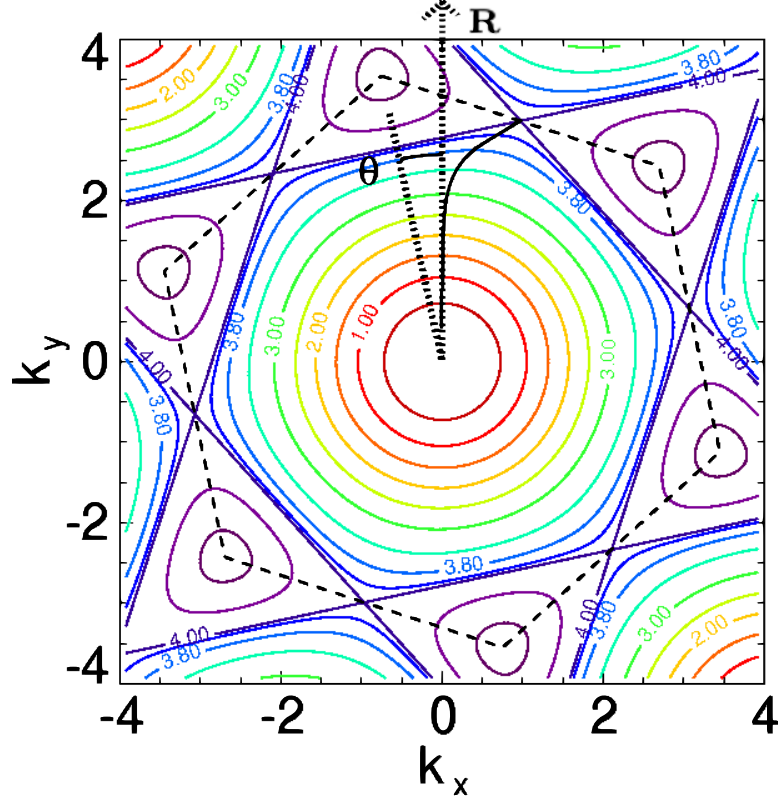


Figure 2.6: Example of constant-energy curves $E = \epsilon$ (for ϵ constant and dimensionless) for a hexagonal lattice when $\theta = \pi/15$; the constant-energy contours were calculated in Ref. [22]. The vertical dotted line points in the k_y direction and is parallel to \mathbf{R} . The slanted, dotted line shows the angle through which the constant-energy curves have been rotated. The black, dashed contour is the boundary of the first Brillouin zone. The solid black curve connecting the origin to the $E = 4$ contour intersects the point on each constant-energy contour for which k_y is maximized, so that $dk_y/dk_x = 0$. The intersection of this curve and the Fermi edge $E = \epsilon_F$ marks the location of the surface states that dominate the RKKY interaction. From Ref. [22].

Chapter 3

Coarse-graining the atomistic model: Burton-Cabrera-Frank theory

In the previous chapter, we considered an atomistic framework that describes the nanoscale evolution of crystal surfaces. In particular, we showed how this framework can be used to model vicinal surfaces, systems of terraces separated by moving steps. In this chapter, our goals are (i) to analytically define the notions of a step, terrace, and adatom, and (ii) derive a BCF-type¹ free boundary model that treats steps as intrinsic elements of the system, i.e. as the interfaces separating adjacent domains (terraces). This second task, in particular, is achieved by coarse-graining an appropriate SLG model of the surface. As the coarse-graining procedure yields correction terms to the BCF theory, a key task of our analysis will be to determine the conditions under which these corrections remain negligible for all times.

This chapter is divided into several sections. In Sec. 3.1, we introduce the key ideas of our derivation and provide a context for our work. In Sec. 3.2 we introduce notation that is used in the chapter. In Sec. 3.3, we formulate the m-particle (m-p) model (which is an analytic version of the kMC algorithm of Sec. 2.2) and apply a low-density approximation in order to derive a corresponding 1-particle (1-p) model. In Sec. 3.4, we show discrete BCF equations can be derived from the 1-p model alone. In Sec. 3.5, we extend this derivation to the m-p model

¹We use the phrase “BCF-type” since the following analysis does not account for step curvature, which is considered in the original work by BCF [16].

and show how the continuum BCF equations, with corrections, arise from the full atomistic perspective. In Sec. 3.6, we discuss our results in the context of variations on our SLG formulation and real material systems, and we outline limitations of the model and pose open questions.

Remark 3.0.1 This chapter is technical in nature. Section 3.5 in particular contains specialized notation and a detailed mathematical proof. For the reader interested in the physical ideas (but not the detailed mathematics) underlying this derivation, Sec. 3.4 should suffice as a replacement for Sec. 3.5; see also the text beginning at Eq. (3.63) and going to the end of Sec. 3.5.

3.1 Key ideas of the derivation

The starting point of the analysis is the 1+1D SLG model described in Sec. 2.2, which describes the evolution of a single step without external deposition. In order to proceed analytically, we first express the kMC Rules 2.2.1–2.2.5 in terms of a master equation and carry out the following tasks:

(i) we define the *mesoscale* step position and adatom density as appropriate averages of the corresponding *microscopic* quantities;

(ii) we show how the BCF model, *with correction terms accounting for adatom correlations*, describes the time evolution of these averages; and

(iii) by using a discrete maximum principle, we show that the temperature and initial adatom density control the size of the corrections to the BCF model.

The central idea of our approach is to exploit the fact that, for many mate-

rials undergoing relaxation at low enough temperatures, the number of adatoms on a surface is typically small. This fact has been predicted by theory [8, 91] and observed experimentally [92] (cf. also Remark 2.2.8). Consequently, we expect that at sufficiently low temperatures, the motion of a few isolated adatoms (as opposed to the correlated motion of many adatoms) should be the dominant physical process driving surface evolution.

These observations motivate two key aspects of our approach. First, we only study a one-step system. Since many systems are found to be in a low-density regime irrespective of the number of steps on the surface, we believe that the addition of more (non-interacting) steps does not significantly alter the dominant evolution process, i.e. single-adatom motion.

Second, we decompose the kMC master equation (m-p model), which accounts for the motion of m atoms, into a Bogoliubov-Born-Green-Kirkwood-Yvon (BBGKY)-type hierarchy [6] whose n th level describes the evolution of the n -adatom joint probabilities. Our analysis shows that the single-adatom probabilities play the dominant role in surface evolution, which leads us to truncate the hierarchy, yielding the 1-p model. We show how the BCF model can be derived from this 1-p model and find that corrections come from the multi-adatom joint probabilities. The size of the corrections is controlled by the temperature, which we treat as a small parameter.² Here we use the term *low-density regime* to describe systems with only

²We always compare the temperature to the bond energy E_b between atoms in the lattice. Temperatures as high as 1000 K (not unusual for experiments) are often small relative to E_b , which can range from a few tenths of an eV to a few eV. Note that room temperature is roughly

one adatom and refer to the neglect of the multi-adatom joint probabilities as the *low-density approximation*.³

A critical task that we address is to reconcile the atomistic nature of the kMC model with the notions of a continuous adatom density and step position in the BCF theory. Here we adopt a procedure that is consistent with Sec. 2.2. Specifically, we define a microscopic step position and adatom density in the context of our SLG model and show that the evolution of their expected values (which are continuous quantities) are described by the BCF-type theory. Importantly, this procedure emphasizes our viewpoint that the definition of a step (as a function of atomistic configurations) is subjective. Our definition implies the existence of the step for all times and is consistent with Boltzmann statistics when the system approaches equilibrium.⁴ Our averaging procedure is motivated by experimental studies of the statistical properties of the step position and terrace-width distribution [32–36]; see also Sec. 1.1.

1/40 eV.

³The term “low-density regime” anticipates one of our main results, since we have not yet discussed any *densities* at this point. In Secs. 3.3 and 3.5 we show, via a suitable averaging procedure, that one-adatom states correspond to a low number-density of adatoms on the surface (see also the following paragraph).

⁴In our approach, whether or not steps form spontaneously depends on the definition of a step.

3.1.1 A 1+1D Burton-Cabrera-Frank-type model

In this Section, we describe the BCF-type model that we seek to derive. For a one-step system, we consider an adatom density, $c(x, t)$, that obeys

$$\partial_t c(x, t) = \mathcal{D} \partial_x^2 c(x, t), \quad (3.1)$$

where \mathcal{D} is a (constant) diffusivity and $0 \leq x < \zeta(t)$, $\zeta(t) < x \leq L$, where $\zeta(t)$ is the step position [cf. Fig. 3.1(b)]. We apply periodic boundary conditions in the coordinate x . Boundary conditions at the step are [8]

$$J_{\pm} = -\mathcal{D} \partial_x c|_{\pm} = \mp \kappa_{\pm} (c^{\pm} - c^{\text{eq}}), \quad x = \zeta(t), \quad (3.2)$$

where J_{\pm} is the adatom flux at the right (+) or left(-) edge of the step, κ_{\pm} is an attachment/detachment rate at the right (+) or left (-) edge of the step,⁵ and c^{\pm} is the adatom concentration to the right (+) or left (-) of the step. The term c^{eq} is an equilibrium adatom concentration. *One of our goals is to derive an expression having the form of Eq. (3.2), which allows us to express k and c^{eq} in terms of parameters of the atomistic, SLG model.*

Because the step moves, we require an additional equation in order to close the system. Let $\dot{\zeta}(t)$ denote the step velocity and set it equal to the net flux,

$$\dot{\zeta}(t) = a(J_- - J_+), \quad (3.3)$$

where a is the (atomic) height of the step. Equation (3.3) can be viewed as a statement about mass conservation: adatoms diffusing to a step attach to or detach from it, which causes the step to advance or retreat.

⁵The original BCF formulation [16] amounts to $\kappa_{\pm} \rightarrow \infty$, so that $c = c^{\text{eq}}$ at the step edge. This limit is identified as *diffusion-limited kinetics*.

In our analysis, we use the term “discrete BCF equations” to refer to Eqs. (3.1)–(3.3) with the derivatives in x replaced by finite differences in the lattice site. The quasi-continuum theory comes from taking the limit as the lattice spacing approaches zero.

3.1.2 Our derivation in the context of past works

Several works have addressed questions related to the connection between atomistic surface models and BCF-type theories. We frame our analysis in the context of those studies.

In [93], Ackerman and Evans recently derived linear kinetic relations analogous to Eq. (3.2) for a 2D surface. We note three differences between their analysis and ours. (i) They focus on the effects of external material deposition, which we leave out. (ii) Their solution to the discrete diffusion equation (atomistic model) is the set of probabilities that an adatom is found at each lattice site, irrespective of the position of all other adatoms; correlations are not considered. In contrast, the solution to our SLG model is the set of joint probabilities of finding adatoms at different locations on the surface, which explicitly includes correlations. In Sec. 3.5, we show that these correlations give rise to correction terms in the BCF model. (iii) Evans and Ackerman fix the step position. Here, we view the step as a reservoir that can always move by emitting (or absorbing) adatoms.

Two decades ago, Zangwill, Vvedensky, et al. used a 2D SLG master equation to derive a modified diffusion equation that accounts for adatom interactions on a

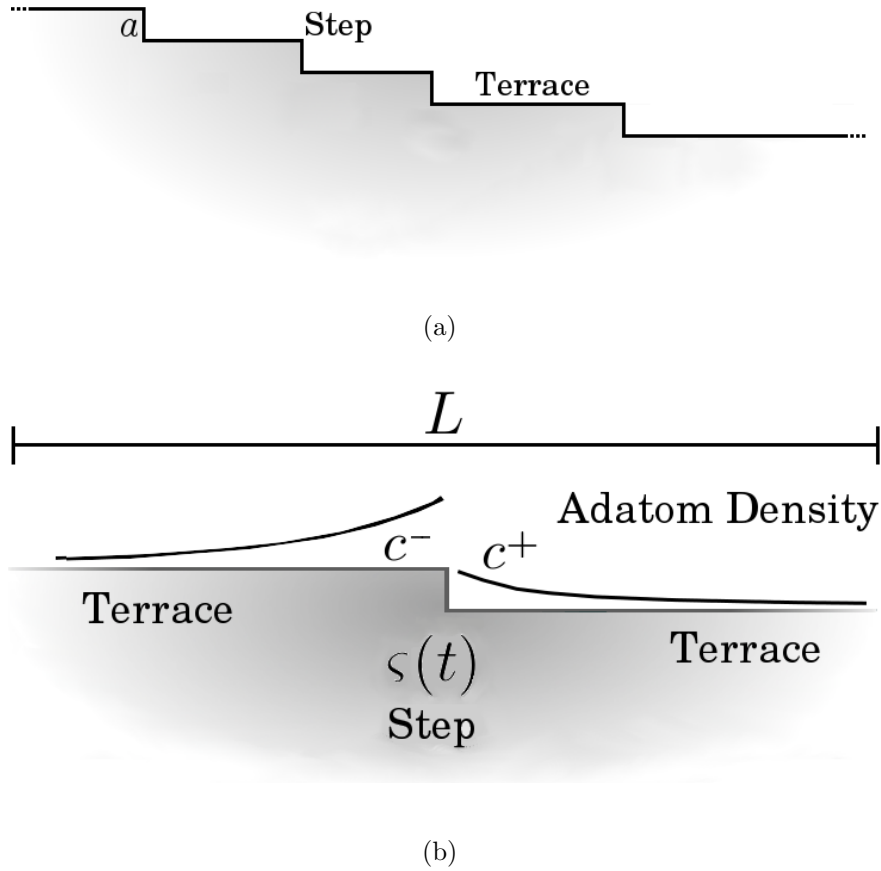


Figure 3.1: (a) A generic, 1D step system with multiple steps (with positions ς_j) separating terraces. Adatoms, represented by the densities c_j , diffuse on each terrace. The velocity of a step is proportional to the net current of adatoms arriving at the step. In general, the adatom densities need not be continuous across a step. In the BCF model, steps, which are an atomic length a in height, are defined as elements of the model from the outset. (b) The single-step system that we consider. The step position is denoted $s(t)$. The values c^\pm are the adatom densities on the right (+) and left (-) sides of the step; L is the length of the system.

terrace and external material deposition [52, 53]. However, they did not derive a step velocity law or linear kinetic relation. An important part of their analysis was to represent the atomistic states as sets of discrete height columns and then average over the heights of those columns. This procedure removes the notion of discrete changes in height associated with steps [see Fig. 3.1(a)]. We, on the other hand, do not average over heights, and we explicitly define steps in our analysis.

A decade ago, Schulze, Smereka, and E compared kMC simulations with the predictions of the BCF model for a system with external material deposition [59]. They found the best agreement between the two models when detachment from the step was switched off in the kMC simulations. We speculate that including both external material deposition and detachment in the kMC model could lead to conditions in which the surface is not in the low-density regime.

3.2 Terminology and notation

A few comments on the terminology and notation are in order.

- We use j as an Eulerian coordinate to represent lattice sites in 1D and \mathbf{j} as a Lagrangian coordinate to represent the position of a single adatom.
- A multiset is an unordered set that treats repeated elements as distinct; e.g. $\{1, 1, 2\}$ is a multiset with three elements.
- Lowercase bold letters (such as $\boldsymbol{\alpha}$ and \mathbf{a}) represent multisets whose elements denote the positions of *indistinguishable* adatoms.⁶

⁶Note that the use of multisets (as opposed to ordered sets) is convenient for our purposes,

- α is an Eulerian coordinate and \mathbf{a} is the corresponding Lagrangian coordinate in a setting where more than one adatom exist on the surface.
- $|\alpha|$ is the cardinality of multiset α , i.e. the number of elements in α , including multiplicity. (However, $|x|$ denotes the absolute value of the real number x , as usual.)
- The symbol $\{\}$ represents the empty set, \emptyset .
- $\alpha \setminus \alpha'$ denotes the multiset difference, or the elements of α that are not contained in α' , including multiplicity (i.e. $\{1, 1, 2\} \setminus \{1, 2, 3\} = \{1\}$).
- $\|\alpha\|$ is the Euclidean norm of α , i.e. $\|\alpha\| = \left(\sum_j j^2\right)^{1/2}$, $j \in \alpha$.
- Matrices are denoted by capital, bold letters (e.g. \mathcal{T}) and the corresponding matrix elements with subscripted letters (e.g. $\mathcal{T}_{i,j}$).
- $\mathcal{T}_{\alpha,\alpha'}$ extends the notation of a matrix element to multisets.
- $\mathbb{1}_\alpha(x) = y$ if x appears y times in α . Note that $\mathbb{1}_\alpha(x)$ is not the standard definition of the set indicator function. We omit the subscript α when the multiset being referenced is clear from context.
- Summation is implied over repeated indices unless otherwise noted.

since it avoids the need to count permutations of particle positions.

3.3 Atomistic, kinetic Monte Carlo master equation

In this Section we formulate an analytic framework from which to derive the BCF theory. We begin by considering the m-p model, which is an analytic version of the kMC algorithm of Sec. 2.2. Motivated by Remark 2.2.8, we show that the m-p model may be cast into the form of a BBGKY-type hierarchy whose first equation describes the motion of a single adatom. In Sec. 3.4, we show that this first equation (which we call the 1-p model) contains the essential elements of the BCF theory.

3.3.1 General case: the m-particle model

We begin with an analytic model that allows m atoms to move on the surface. We use the setting of Sec. 2.2; cf. Fig. 2.3.

Consider the system described in Sec. 2.2.1, and let α be a multiset whose elements denote the positions of $|\alpha| \leq m$ adatoms. Any element $j \in \alpha$ records the location of one of the m adatoms, where $0 \leq j \leq N - 1$. Moreover, the elements $j \in \alpha$ may have a multiplicity greater than 1; the multiplicity of j is equal to the number of adatoms at the lattice site j . Since the location of all adatoms contains all of the information about the system, we call $\mathbf{a} = \alpha$ the system *state*.

Our SLG model analytically expresses the rules of Sec. 2.2.1 via a system of ordinary differential equations (ODEs), a master equation.

Definition 3.3.1 (*m-p model*) *Let $p_\alpha(t)$ be the probability that there are adatoms occupying the sites given by α , where $|\alpha| \leq m$. This p_α satisfies the ODEs*

$$\dot{p}_\alpha = \mathcal{T}_{\alpha, \alpha'} p_{\alpha'}, \quad (3.4)$$

for $t > 0$. These ODEs are supplemented by screw periodic boundary conditions and the initial data $p_{\alpha}(0)$, which satisfies $\sum_{\alpha} p_{\alpha}(0) = 1$. The transition matrix $\mathcal{T} = [\mathcal{T}_{\alpha, \alpha'}]$ has the following properties.

$$\mathcal{T}_{\alpha, \alpha'} = 0 \quad \text{if } |\alpha| = |\alpha'|, |\alpha \setminus \alpha'| = 1, \text{ and } \left| \|\alpha \setminus \alpha'\| - \|\alpha' \setminus \alpha\| \right| > 1, \quad (3.5)$$

$$\mathcal{T}_{\alpha, \alpha'} = 0 \quad \text{if } \left| |\alpha| - |\alpha'| \right| > 1, \quad (3.6)$$

$$\mathcal{T}_{\alpha, \alpha'} = D \quad \text{if } |\alpha| = |\alpha'| \text{ and } \left| \|\alpha \setminus \alpha'\| - \|\alpha' \setminus \alpha\| \right| = 1, \quad (3.7)$$

$$\mathcal{T}_{\alpha, \alpha'} = Dk\phi_{\pm} \quad \text{if } |\alpha| - |\alpha'| = 1 \text{ and } \alpha \setminus \alpha' = \{s_0 - |\alpha'| \pm 1\}, \quad (3.8)$$

$$\mathcal{T}_{\alpha, \alpha'} = D\phi_{\pm} \quad \text{if } |\alpha'| - |\alpha| = 1 \text{ and } \alpha' \setminus \alpha = \{s_0 - |\alpha| \pm 1\}, \quad (3.9)$$

$$\mathcal{T}_{\alpha, \alpha} = - \sum_{\substack{\alpha' \\ \alpha' \neq \alpha}} \mathcal{T}_{\alpha', \alpha} \quad \text{for all } \alpha. \quad (3.10)$$

Equations (3.5)–(3.10) have interpretations in terms of Rules 2.2.1–2.2.5. Equation (3.5) states that only one adatom may move at a time, and in this process, it may only move a distance of one lattice site (Rule 2.2.1). Equation (3.6) states that no process may create or destroy more than one adatom [Rule 2.2.5; cf. also Remark 2.2.3]. Equation (3.7) states that adatoms hop between terrace sites at a constant rate D (Rule 2.2.2). Equation (3.8) states that edge atoms detach to the right or left at a constant rate $Dk\phi_{\pm}$ (Rule 2.2.4). Equation (3.9) states that adatoms attach to the step from the right or left at a constant rate $D\phi_{\pm}$ (Rule 2.2.3). Equation (3.10) ensures that probability is conserved, or equivalently, that $\sum_{\alpha} \dot{p}_{\alpha} = 0$.

Evidently, the parameter s_0 is the location of the edge atom when there are no adatoms on the surface. Thus, $s_0 - |\mathbf{a}|$ measures the position of the edge atom (or the microscopic step position) relative to the state $\{\}$ (when the edge atom is

at s_0). Equations (3.8) and (3.9) account for bonding at the edge atom site when multiple adatoms are on the surface.⁷

Remark 3.3.1 Any set of real initial data $p_\alpha(0)$ approaches a unique steady state in the long time limit; for a proof, see [23].

3.3.2 An example: the 2-particle model

In this section, we give a specific example of an m-p model in which there are only *two* movable atoms in the entire system, i.e. $m = 2$.

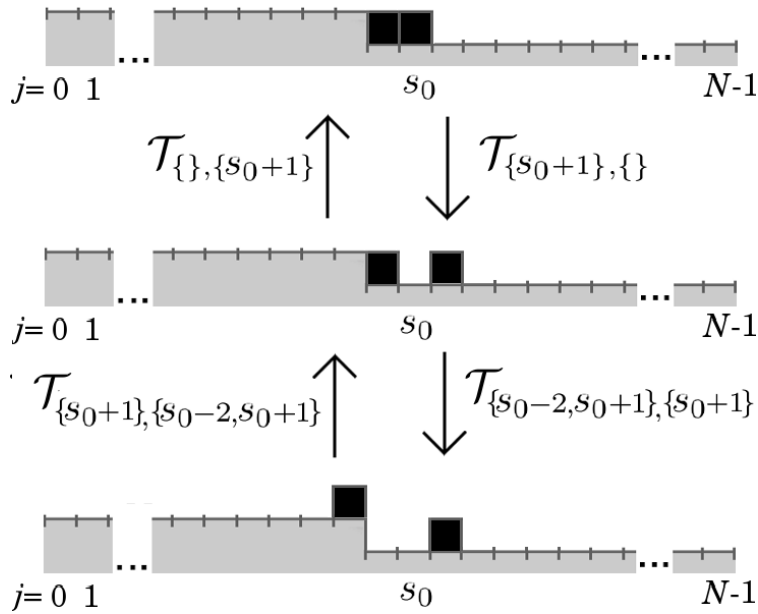


Figure 3.2: Schematic of the 2-p model. Only two atoms are movable. Top: Zero-particle state ($|\alpha| = 0$). Middle: One-particle state, for which $|\alpha| = 1$. Bottom: Two-particle state, for which $|\alpha| = 2$. The matrix elements of \mathcal{T} that describe the transition rates between the illustrated states are written next to arrows indicating the direction of the transition. See also Eq. (3.11).

⁷Because the form of the transition matrix (3.5)–(3.10) is translation invariant in s_0 , the step velocity law that we derive in Sec. 3.5 is independent of s_0 .

The multisets α that label adatom configurations may have 0, 1, or 2 elements, which correspond to zero-particle, one-particle, or two-particle states; see Fig. 3.2.

We enumerate all of the non-zero, off-diagonal matrix elements of $T_{\alpha,\alpha'}$:

$$\mathcal{T}_{\{s_0 \pm 1\}, \{\}} = Dk\phi_{\pm}, \quad (0\text{-p} \rightarrow 1\text{-p transition}) \quad (3.11a)$$

$$\mathcal{T}_{\{\}, \{s_0 \pm 1\}} = D\phi_{\pm}, \quad (1\text{-p} \rightarrow 0\text{-p}) \quad (3.11b)$$

$$\mathcal{T}_{\{j\}, \{j \pm 1\}} = D, \quad j, j \pm 1 \neq s_0 - 1, \quad (1\text{-p} \rightarrow 1\text{-p}) \quad (3.11c)$$

$$\mathcal{T}_{\{j, s_0 - 1 \pm 1\}, \{j\}} = Dk\phi_{\pm}, \quad j \neq s_0, s_0 - 1, \quad (1\text{-p} \rightarrow 2\text{-p}) \quad (3.11d)$$

$$\mathcal{T}_{\{j\}, \{j, s_0\}} = D\phi_+, \quad j \neq s_0 - 1, \quad (2\text{-p} \rightarrow 1\text{-p}) \quad (3.11e)$$

$$\mathcal{T}_{\{j\}, \{j, s_0 - 2\}} = D\phi_-, \quad j \neq s_0 - 1, s_0, \quad (2\text{-p} \rightarrow 1\text{-p}) \quad (3.11f)$$

$$\mathcal{T}_{\{j, k\}, \{j, k \pm 1\}} = D, \quad j \neq s_0 - 1, \quad (2\text{-p} \rightarrow 2\text{-p}) \quad (3.11g)$$

$$k, k \pm 1 \neq s_0 - 1.$$

3.3.3 M-particle model as a BBGKY-type hierarchy

As Sec. 3.3.2 illustrates, it is possible to separate the system states into a hierarchy based on the number of adatoms $|\mathbf{a}|$ in state \mathbf{a} . In general, we write

$$\dot{p}_{\alpha} = \sum_{|\alpha'|=|\alpha|-1} \mathcal{T}_{\alpha,\alpha'} p_{\alpha'} + \sum_{|\alpha'|=|\alpha|} \mathcal{T}_{\alpha,\alpha'} p_{\alpha'} + \sum_{|\alpha'|=|\alpha|+1} \mathcal{T}_{\alpha,\alpha'} p_{\alpha'}. \quad (3.12)$$

Equation (3.12) is a BBGKY-type hierarchy that connects the time evolution of an $|\alpha|$ -adatom joint probability to the $(|\alpha|-1)$ - and $(|\alpha|+1)$ -adatom joint probabilities.

Motivated by Remark 2.2.8, we explicitly write the equations for $|\mathbf{a}| = 1$:

$$\begin{aligned} \dot{p}_{\{j\}} = & D[p_{\{j+1\}} - 2p_{\{j\}} + p_{\{j-1\}}] - Dk(\phi_+ + \phi_-)p_{\{j\}} \\ & + D\phi_+p_{\{j,s_0\}} + D\phi_-p_{\{j,s_0-2\}}, \quad j \neq 0, s_0, s_0 \pm 1, N-1, \end{aligned} \quad (3.13)$$

$$\begin{aligned} \dot{p}_{\{s_0+1\}} = & D[k\phi_+p_{\{s_0+1\}} - (1 + \phi_+)p_{\{s_0+1\}} + p_{\{s_0+2\}}] - Dk(\phi_+ + \phi_-)p_{\{s_0+1\}} \\ & + D\phi_+p_{\{s_0,s_0+1\}} + D\phi_-p_{\{s_0-2,s_0+1\}}, \end{aligned} \quad (3.14)$$

$$\dot{p}_{\{s_0-1\}} = D[k\phi_-p_{\{s_0-1\}} - (1 + \phi_-)p_{\{s_0-1\}} + p_{\{s_0-2\}}], \quad (3.15)$$

$$\dot{p}_{\{\}} = D[\phi_-p_{\{s_0-1\}} - k(\phi_- + \phi_+)p_{\{\}} + \phi_+p_{\{s_0+1\}}]. \quad (3.16)$$

Note that the terms $Dk(\phi_+ + \phi_-)p_{\{j\}}$ and $D\phi_+p_{\{j,s_0\}} + D\phi_-p_{\{j,s_0-2\}}$ in Eq. (3.13) [and the analogous terms in Eq. (3.14)] account for processes in which an adatom detaches from or attaches to the step.

Based on our numerical results in Sec. 2.2, we expect that the system will predominantly reside in the 1-p states described by Eqs. (3.13)–(3.16). Note that Eq. (3.13) resembles a discrete diffusion equation (provided we ignore processes involving two-particle states), and Eqs. (3.14)–(3.16) describe transitions at the step.

3.3.4 1-p model

In this section, we define the 1-p model more precisely as coming from a truncation of the m-p model at the level of the $|\mathbf{a}| = 1$ states. Consider (3.13)–(3.16) and neglect all terms that contain (i) p_{α} , where $|\alpha| = 2$, or (ii) kp_{α} , where $\alpha \neq \{\}$. We replace the multiset notation $\alpha = \{j\}$ with the index j and $\alpha = \{\}$ with s_0 . This truncation scheme amounts to the low-density approximation and produces the 1-p model as follows.

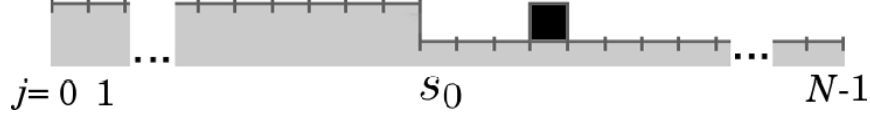


Figure 3.3: Schematic of the 1-p model. Only a single particle is allowed to move on the surface, and it may occupy one of N lattice sites, indexed $0 \leq j \leq N - 1$. All other particles are fixed.

Definition 3.3.2 Let $p_j(t)$ be the probability that the atom is at site j . This $p_j(t)$ is the solution to the 1-p model if

$$\dot{p}_j = D[p_{j+1} - 2p_j + p_{j-1}], \quad j \neq 0, s_0, s_0 \pm 1, N - 1 \quad (3.17)$$

$$\dot{p}_{s_0 \pm 1} = D[k\phi_{\pm} p_{s_0} - (1 + \phi_{\pm})p_{s_0 \pm 1} + p_{s_0 \pm 2}], \quad (3.18)$$

$$\dot{p}_{s_0} = D[\phi_- p_{s_0-1} - k(\phi_- + \phi_+)p_{s_0} + \phi_+ p_{s_0+1}], \quad (3.19)$$

for $t > 0$, which are supplemented by the initial data $p_j(0)$ and the screw periodic boundary conditions,

$$\dot{p}_0 = D[p_1 - 2p_0 + p_{N-1}], \quad (3.20)$$

$$\dot{p}_{N-1} = D[p_{N-2} - 2p_{N-1} + p_0], \quad (3.21)$$

where $p_j(0)$ must satisfy

$$\sum_{j=0}^{N-1} p_j(0) = 1. \quad (3.22)$$

By analogy to Sec. 3.3.1, we denote the position of the moving atom by \mathbf{j} , where $0 \leq \mathbf{j} \leq N - 1$ (cf. Fig. 3.3). We refer to the atom position \mathbf{j} (which is a Lagrangian coordinate) as the system *state*, since \mathbf{j} is the only element of the model that changes.

It is straightforward to show that the boundary conditions (3.20) and (3.21) imply $\sum_{j=0}^{N-1} \dot{p}_j = 0$, so that properly normalized initial data will remain so for all times $t > 0$.

Equations (3.17)–(3.21) may be written in the form

$$\dot{p}_j = \mathcal{T}_{j,j'} p_{j'}, \quad (3.23)$$

where $\mathcal{T}_{j,j'}$ is a matrix element that describes the transition rate from state $j' = j'$ to state $j = j$. The matrix elements are

$$\begin{aligned} \mathcal{T}_{j,j'} = & D\{\delta_{j+1,j'}[1 + \delta_{j,s_0}(\phi_+ - 1) + \delta_{j+1,s_0}(k\phi_- - 1)] \\ & - \delta_{j,j'}[2 + \delta_{j,s_0}(\phi_+ + \phi_- - 2) + \delta_{j,s_0+1}(\phi_+ - 1) + \delta_{j,s_0-1}(\phi_- - 1)] \\ & + \delta_{j-1,j'}[1 + \delta_{j,s_0}(\phi_+ - 1) + \delta_{j-1,s_0}(k\phi_+ - 1)]\}, \end{aligned} \quad (3.24)$$

where $\delta_{j,j'}$ is the Kronecker delta, i.e. $\delta_{j,j'} = 1$ if $j = j'$ and $\delta_{j,j'} = 0$ if $j \neq j'$.

Remark 3.3.2 Any real initial data will evolve to a unique steady state at long times; see Ref. [23].

3.4 Averaging the 1-particle model: physics of step-flow

Motivated by the results of Sec. 2.2.2 and Remark 2.2.8, our goal in this section is to show that the 1-p model contains the essential elements of the BCF model. In this vein, we pursue the following tasks: (i) we define the mesoscale step position and adatom density as averages over the probabilities $p_j(t)$ of the 1-p model (Sec. 3.4.1); (ii) we show that the time evolution of these averages is described by a *discrete* second order difference scheme for the adatom density, a step velocity law

(Sec. 3.4.2); (iii) we derive a linear kinetic relation, *with corrections*, at the step edge (Sec. 3.4.2); and (iv) we determine the conditions under which the corrections remain negligibly small for all $t > 0$ (Sec. 3.4.3).

3.4.1 1-particle equilibrium solution: notion of averaging

We use the notion of the equilibrium Boltzmann distribution to motivate definitions of the step position and adatom density for a system out of equilibrium.

We begin by setting $\dot{p}_j = 0$ in (3.17)–(3.21). By inspection we find that the steady state solution is $p_j^{\text{eq}} = k/\mathcal{Z}$ for $j \neq s_0$ and $p_{s_0}^{\text{eq}} = 1/\mathcal{Z}$, where $\mathcal{Z} = [(N-1)k+1]$ is a normalization constant.⁸ Noting that $k = \exp(-E_b/k_B T)$, we immediately conclude that p_j^{eq} is the Boltzmann distribution corresponding to our 1-p model; the steady state is equilibrium.

Hence, a natural definition of the equilibrium step position is

$$\zeta^{\text{eq}} := \left[\sum_{j \neq s_0} (s_0 - 1) a p_j^{\text{eq}} \right] + s_0 a p_{s_0}^{\text{eq}}, \quad (3.25)$$

while the adatom density may be defined as

$$c_j^{\text{eq}} := p_j^{\text{eq}}/a \quad j \neq s_0, \quad (3.26)$$

where $a = L/N$ and L is the linear size of the system. Note that the equilibrium adatom density is everywhere constant (cf. Fig. 2.4).

We define the time-dependent step position and adatom density by replacing the equilibrium probabilities p_j^{eq} with $p_j(t)$ in expressions (3.25) and (3.26).

⁸ \mathcal{Z} is in fact the partition function.

Definition 3.4.1 *The step position $\varsigma(t)$ and adatom density $c_j(t)$ are defined as*

$$\varsigma(t) := \left[\sum_{j \neq s_0} a(s_0 - 1)p_j(t) \right] + a s_0 p_{s_0}(t), \quad (3.27)$$

$$c_j(t) := p_j(t)/a \quad j \neq s_0, \quad (3.28)$$

for all $t \geq 0$.

By Remark 3.3.2, $s(t)$ and $c_j(t)$ are guaranteed to converge to their equilibrium values given by (3.25) and (3.26). Hence, we view (3.27) and (3.28) as the simplest expressions for the step position and adatom density that are consistent with equilibrium statistical mechanics. Note that (3.27) is the expectation value of the *microscopic* step position defined in Sec. 2.2.1. In the context of our master equation perspective, we believe that (3.27) is the first instance of an analytic definition of a step.

Remark 3.4.1 We always assume that $N \exp(-E_b/k_B T) = Nk \ll 1$. This may be viewed as either a low-temperature or high-bond energy limit of the system. Recalling that $\mathcal{Z} = (N - 1)k + 1$ one finds that $p_{s_0}^{\text{eq}} = 1/\mathcal{Z} = 1 - \mathcal{O}(Nk)$ and $p_j^{\text{eq}} = k/\mathcal{Z} = k - \mathcal{O}(Nk^2)$ for $j \neq s_0$. That is, the low-temperature limit also corresponds to a low-density limit of the system, insofar as in equilibrium, the atom remains attached to the step with a probability approximately equal to 1; see also Sec. 3.4.3.

Remark 3.4.2 We always assume that $D = \mathcal{O}(N^2) s^{-1}$; see Sec. 3.6.1 for justification in the context of real material systems. Note that by definition $a = L/N$, so that $a^2 D = \mathcal{O}(L^2) s^{-1}$.

3.4.2 Evolution laws for averaged quantities

Next, we derive evolution laws for (3.27) and (3.28). Applying a time derivative to (3.27) and noting that the sum over (3.17) is telescoping, we find

$$\dot{\zeta}(t) = a^2 D\phi_-(c_{s_0-1} - kp_{s_0}/a) + a^2 D\phi_+(c_{s_0+1} - kp_{s_0}/a). \quad (3.29)$$

The differences $c_{s_0\pm 1} - kp_{s_0}/a$ are proportional to the flux of adatoms to site s_0 , and the step velocity is given by the difference of adatom fluxes at the step.

Equation (3.17) is already a discrete adatom diffusion equation, so that we only need to derive boundary conditions at the step edge. We first write (3.18) in the same form as (3.17) plus a remainder term:

$$\dot{c}_{s_0\pm 1} = D(c_{s_0}^\pm - 2c_{s_0\pm 1} + c_{s_0\pm 2}) + D[(1 - \phi_\pm)c_{s_0\pm 1} + (k\phi_\pm)p_{s_0}/a - c_{s_0}^\pm], \quad (3.30)$$

where we introduce the new variables $c_{s_0}^\pm$, which we interpret as the right (+) or left (-) density at the step edge. We identify these densities $c_{s_0}^\pm$ as the discrete analogues of c^\pm appearing in (3.2).

By setting

$$D[c_{s_0\pm 1} - c_{s_0}^\pm] = D\phi_\pm[c_{s_0\pm 1} - kp_{s_0}/a], \quad (3.31)$$

we cast (3.30) into the same form as (3.17) and determine a set of boundary conditions for the adatom density at the step edge.⁹

To interpret the quantities appearing in (3.31), we compare this equation with (3.2). On the left-hand side of (3.31), we identify

$$\mathcal{J}_\pm := aD(c_{s_0\pm 1} - c_{s_0}^\pm) \quad (3.32)$$

⁹Note that (3.31) adds two additional equations (corresponding to $c_{s_0}^\pm$) to the system (3.17)–(3.21).

as the discrete flux to the step edge. On the right-hand side of (3.32), we assume that $c_{s_0\pm 1} \approx c_{s_0}^\pm$ when $a = L/N$ is small.

Caution should be exercised in comparing the term kp_{s_0}/a of (3.31) with the c^{eq} of the BCF theory. In (3.2), c^{eq} is a reference density against which $c_{s_0}^\pm$ is measured. If the $c_{s_0}^\pm$ equals c^{eq} , then no current flows to or from the step. Moreover, this reference density should be defined for a system in equilibrium.

Microscopically, this idea corresponds to a detailed balance of flux at the step edge. Specifically, in (3.18), if $p_{s_0\pm 1} = k/\mathcal{Z}$ and $p_{s_0} = 1/\mathcal{Z}$, then on average, no adatoms diffuse to or from the step. *In the kMC model, the reference density is simply proportional to the rate k at which atoms detach from the step, provided k is small.* This idea is further reinforced by the usual definition that $c^{\text{eq}} \sim \exp(-\mu/k_B T)$, where the chemical potential μ is the energy cost of adding an adatom to the surface. In the kMC model, this cost is precisely E_b . Hence, we define the discrete equilibrium density as

$$\check{c}^{\text{eq}} := k/a. \tag{3.33}$$

On the right-hand side of (3.31), this \check{c}^{eq} is multiplied by p_{s_0} . However, we recall that when $kN \ll 1$, the equilibrium solution $p_{s_0} = 1 - \mathcal{O}(Nk)$. Therefore, we postulate that whenever the system is sufficiently close to equilibrium, we can replace $kc_{s_0} \rightarrow k/a + \mathcal{O}[(Nk)^2]$ and neglect the correction term. Under this assumption, we write

$$\mathcal{J}_\pm = aD\phi_\pm[c_{s_0\pm 1} - k/a] + a^2D\mathcal{O}[(Nk)^2] \sim D\phi_\pm[c_{s_0\pm 1} - \check{c}^{\text{eq}}], \tag{3.34}$$

which is a discretized version of (3.2).

Remark 3.4.3 Unlike the correction terms that we consider in Sec. 3.5, the $\mathcal{O}[(Nk)^2]$ term in (3.34) is due to memory effects, not multi-atom correlations. Indeed, by integrating (3.19), we obtain

$$p_{s_0}(t) = D \int_0^t dt' e^{-Dk(\phi_- + \phi_+)(t-t')} [\phi_- p_{s_0-1}(t') + \phi_+ p_{s_0+1}(t')]. \quad (3.35)$$

The value of p_{s_0} that multiplies k/a in (3.31) depends on the history of p_{s_0-1} and p_{s_0+1} . Physically, we interpret this to mean that the rate of detachment from a step depends on whether an edge atom is actually available to detach.

3.4.3 Maximum principle for 1-particle model

In this section, we derive a simple maximum principle (cf. [94]) that specifies a class of initial data for which $c_{s_0} = \mathcal{O}[(aZ)^{-1}]$ for all times. When this condition is satisfied, we define the system as being “near-equilibrium.” If, in addition, $Nk \ll 1$ (i.e. in the low-temperature regime), then $kc_{s_0} = k/a - \mathcal{O}[(Nk)^2]$, and we can ignore the correction terms in (3.31).

Proposition 3.4.1 *Let $p_j(t)$ be the solution to (3.17)–(3.21) with initial data $p_j(0)$, and define $\hat{p}_j = p_j/k$ for $j \neq s_0$ and $\hat{p}_{s_0} = p_{s_0}$. Then \hat{p}_j satisfies the maximum principle that $\max_j \{\hat{p}_j(t)\} \leq \max_j \{\hat{p}_j(0)\}$ for all $t > 0$.*

Proof 3.4.1 We proceed by *reductio ad absurdum*. Writing (3.17)–(3.21) in terms

of \hat{p}_j yields

$$\begin{aligned}
k\dot{\hat{p}}_j &= Dk[\hat{p}_{j+1} - 2\hat{p}_j + \hat{p}_{j-1}], & j \neq s_0, s_0 \pm 1, \\
k\dot{\hat{p}}_{s_0 \pm 1} &= Dk[\phi_{\pm}\hat{p}_{s_0} - (1 + \phi_{\pm})\hat{p}_{s_0 \pm 1} + \hat{p}_{s_0 \pm 2}], \\
\dot{\hat{p}}_{s_0} &= Dk[\phi_-\hat{p}_{s_0-1} - (\phi_- + \phi_+)\hat{p}_{s_0} + \phi_+\hat{p}_{s_0+1}].
\end{aligned} \tag{3.36}$$

Let us assume that at some time t there is an l such that $\dot{\hat{p}}_l(t) \geq 0$ and $\hat{p}_l(t) \geq \hat{p}_j(t)$ for all $j \neq l$. By virtue of (3.36), we infer that

$$\hat{p}_l(t) \geq \frac{\theta_1 \hat{p}_{l-1}(t) + \theta_2 \hat{p}_{l+1}(t)}{\theta_1 + \theta_2},$$

where $\theta_{1,2}$ stand for 1 or ϕ_{\pm} , depending on the value of l . By assumption, it is impossible to have $\hat{p}_{l \pm 1}(t) > \hat{p}_l(t)$, so that either \hat{p}_l is not a maximum or \hat{p}_j is constant for all j .

Corollary 3.4.1 *If $p_j(0) \leq \mathcal{O}(k)$ for $j \neq s_0$ and $p_{s_0}(0) = \mathcal{O}(1)$, then $p_j(t) \leq \mathcal{O}(k)$ for $j \neq s_0$ and $p_{s_0}(t) = \mathcal{O}(1)$ for all times t .*

Definition 3.4.2 *Whenever $p_j(0)$ satisfies the hypotheses of Corollary 3.4.1, we define the state of the system to be near equilibrium.*

Corollary 3.4.1 specifies the conditions under which (3.34) is a discrete linear kinetic relation to $\mathcal{O}(k)$; if the system starts in any configuration in which $p_{s_0} = \mathcal{O}(1)$, then corrections to the linear kinetic relation will always be $\mathcal{O}[(Nk)^2]$.

3.5 Derivation of a Burton-Cabrera-Frank-type model

Motivated by the results of Sec. 2.2.2 and Remark 2.2.8, our goal in this section is to show that the BCF model describes the evolution of a surface with a

low density of adatoms. In this vein, we pursue the following tasks: (i) we define the step position and adatom density as averages over the probabilities $p_{\alpha}(t)$ of the m-p model (Sec. 3.5.1); (ii) we show that the time evolution of these averages, plus corrections, is described by a *discrete* second order difference scheme for the adatom density, a step velocity law (Sec. 3.5.2); (iii) we derive a linear kinetic relation, *with corrections*, at the step edge (Sec. 3.5.2); and (iv) we determine the conditions under which the corrections remain negligibly small for all $t > 0$ (Sec. 3.5.3). Finally, we show that the step continuum theory emerges in the limit that the lattice spacing goes to zero (Sec. 3.5.4).

3.5.1 Averaging: definitions of step position and adatom density

In this section, we define the step position and adatom density for the m-p model by averaging over all states α ; cf. Eq. (3.38) and Eq. (3.39). We begin by finding the equilibrium solution of the m-p model. Examination of Eqs. (3.5)–(3.10) reveals that $\dot{p}_{\alpha} = 0$ implies that the steady state solution is $p_{\alpha}^{\text{eq}} = k^{|\alpha|}/\mathcal{Z}$ for all α , where

$$\mathcal{Z} := 1 + k \left(\sum_{|\alpha|=1} 1 \right) + k^2 \left(\sum_{|\alpha|=2} 1 \right) + \dots + k^m \left(\sum_{|\alpha|=m} 1 \right). \quad (3.37)$$

Noting that $k^{|\alpha|} = \exp(-|\alpha|E_b/k_B T)$, where $|\alpha|$ is the number of adatoms in state α , we conclude that the steady-state solution of the m-p model is in fact the Boltzmann distribution, where \mathcal{Z} is the partition function.

Consequently, we define the following *time-dependent* expectation values for the step position and adatom density.

Definition 3.5.1 *The step position $\varsigma(t)$ and adatom density $c_j(t)$ at the j th lattice site away from the step are defined as*

$$\varsigma(t) := \left[\sum_{\alpha} a (s_0 - |\alpha|) p_{\alpha}(t) \right] \quad (3.38)$$

$$c_j(t) := \sum_{\substack{\alpha \\ s_0 - |\alpha| + 1 + j \in \alpha}} p_{\alpha}(t) / a, \quad (3.39)$$

for all $t > 0$, where $a = L/N$ is the lattice spacing.

Importantly, these definitions converge to the equilibrium expectation values of the microscopic step position and adatom density; see Ref. [23].

Remark 3.5.1 Equation (3.39) is the expectation value of finding *at least* one adatom j sites from the step. This definition does not coincide with the conventional notion of a particle density, since $|\alpha|$ does not multiply p_{α} . On the other hand, Eq. (3.39) is appropriate for comparing with a kMC scheme in which only one particle is allowed to move at any given time, regardless of how many adatoms occupy a given site. See Sec. 3.6.3 for a discussion of this point.

Remark 3.5.2 If $Nk \ll 1$, then by Eq. (3.37), one finds $\mathcal{Z} = 1 - \mathcal{O}(Nk)$. In equilibrium the probability that all atoms are attached to the step is $p_{\{\}} = 1 - \mathcal{O}(Nk)$.

3.5.2 Discrete Burton-Cabrera-Frank equations

In this section we derive evolution laws for the (time dependent) step position and adatom density. We begin by applying a time derivative to Eq. (3.38) and using

Eqs. (3.5)–(3.10) to simplify the resulting expression. This yields

$$\begin{aligned} \dot{c}(t) = & Da^2[\phi_+c_1(t) + \phi_-c_{-1}(t) - (\phi_- + \phi_+)(k/a)] \\ & - Da \sum_{\alpha \in \mathcal{F}_a^+} \phi_+p_\alpha - Da \sum_{\alpha \in \mathcal{F}_a^-} \phi_-p_\alpha + Da \sum_{\alpha \in \mathcal{F}_d} k(\phi_+ + \phi_-)p_\alpha, \end{aligned} \quad (3.40)$$

where the sets \mathcal{F}_a^\pm and \mathcal{F}_d are defined as

$$\mathcal{F}_a^+ := \{\alpha : \mathbb{1}(s_0 - |\alpha| + 2) \geq 2\}, \quad (3.41)$$

$$\mathcal{F}_a^- := \{\alpha : \mathbb{1}(s_0 - |\alpha| + 2) \geq 1, \mathbb{1}(s_0 - |a|) \geq 1\}, \quad (3.42)$$

$$\mathcal{F}_d := \{\alpha : s_0 - |\alpha| \in \alpha\}. \quad (3.43)$$

Equations (3.41)–(3.43) define the sets of states in which attachment to the step from the right (\mathcal{F}_a^+), attachment from the left (\mathcal{F}_a^-), and detachment (\mathcal{F}_d) are forbidden; cf. Rule 2.2.5 and Fig. 3.4. By virtue of Eq. (3.39) (the definition for $c_j(t)$), such forbidden transitions are included in the first line of step velocity law Eq. (3.40), so that the second line is necessary to remove them.

In order to derive the discrete adatom diffusion equation, we apply a time derivative to Eq. (3.39) for $j \neq \pm 1$ and again use Eqs. (3.5)–(3.10) to simplify the resulting expression. By letting $\tilde{p}_\alpha = p_\alpha/a$, we find

$$\begin{aligned} \dot{c}_j(t) = & D[c_{j+1} - 2c_j + c_{j-1}] \\ & - D \sum_{\alpha \in \mathcal{U}_j^-} \tilde{p}_\alpha + 2D \sum_{\alpha \in \mathcal{U}_j} \tilde{p}_\alpha - D \sum_{\alpha \in \mathcal{U}_j^+} \tilde{p}_\alpha \\ & - D \sum_{\alpha \in \mathcal{D}_j} k(\phi_+ + \phi_-)\tilde{p}_\alpha + D \sum_{\alpha \in \mathcal{A}_{j+1}^+} \phi_+\tilde{p}_\alpha + D \sum_{\alpha \in \mathcal{A}_{j+1}^-} \phi_-\tilde{p}_\alpha \\ & + D \sum_{\alpha \in \mathcal{D}_{j-1}} k(\phi_+ + \phi_-)\tilde{p}_\alpha - D \sum_{\alpha \in \mathcal{A}_j^+} \phi_+\tilde{p}_\alpha - D \sum_{\alpha \in \mathcal{A}_j^-} \phi_-\tilde{p}_\alpha, \end{aligned} \quad (3.44)$$

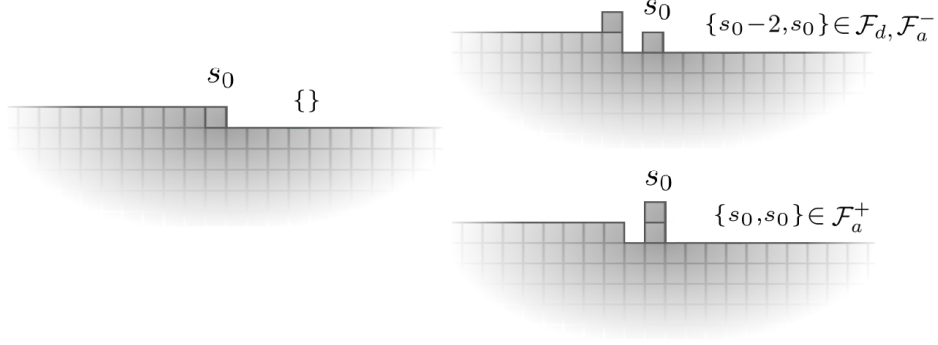


Figure 3.4: Illustration of forbidden transitions in our kMC model. The state $\{\}$ on the left may not transition to the states $\{s_0 - 2, s_0\}$ or $\{s_0, s_0\}$ on the right. More generally, the model forbids processes in which (i) a step atom moves or (ii) two or more step atoms are created; see also Eqs. (3.41)–(3.43).

where the sets \mathcal{U}_j , \mathcal{U}_j^\pm , \mathfrak{D}_j , and \mathcal{A}_j^\pm are defined as

$$\mathcal{U}_j := \{\alpha : \mathbb{1}(s_0 - |\alpha| + 1 + j) \geq 2\}, \quad (3.45)$$

$$\mathcal{U}_j^+ := \{\alpha : s_0 - |\alpha| + 1 + j \in \alpha, s_0 - |\alpha| + 2 + j \in \alpha\}, \quad (3.46)$$

$$\mathcal{U}_j^- := \{\alpha : s_0 - |\alpha| + j \in \alpha, s_0 - |\alpha| + 1 + j \in \alpha\}, \quad (3.47)$$

$$\mathfrak{D}_j := \{\alpha : s_0 - |\alpha| + j + 1 \in \alpha, s_0 - |\alpha| \notin \alpha\}, \quad (3.48)$$

$$\mathcal{A}_j^+ := \{\alpha : s_0 - |\alpha| + j + 1 \in \alpha, \mathbb{1}(s_0 - |\alpha| + 2) = 1\}, \quad (3.49)$$

$$\mathcal{A}_j^- := \{\alpha : s_0 - |\alpha| + j + 1 \in \alpha, s_0 - |\alpha| \in \alpha, s_0 - |\alpha| + 2 \notin \alpha\}. \quad (3.50)$$

The set \mathcal{U}_j contains all states α in which two or more adatoms are at site j (relative to the step), while the sets \mathcal{U}_j^\pm are those sets in which an adatom is at site j , and another adatom is at $j \pm 1$. The set \mathfrak{D}_j contains all states with an adatom at j and an edge atom that may detach from the step. The sets \mathcal{A}_j^\pm contain the states with an adatom at j and another adatom which is able to attach to the step from

the left (-) or right (+). By virtue of Eq. (3.39), transitions between state $\mathbf{a} \in \mathcal{U}_j$ and state $\mathbf{a}' \in \mathcal{U}_j^\pm$ (where $T_{\mathbf{a},\mathbf{a}'} \neq 0$) leave the value of $c_j(t)$ unchanged; thus, the second line of Eq. (3.44) removes such transitions from Eq. (3.44) (see also Fig. 3.5 and Remark 3.5.1). The third and fourth lines of Eq. (3.44) account for the fact that the density $c_j(t)$ [cf. Eq. (3.39)] changes whenever the step moves, since the adatom positions are always measured relative to the step; see also Fig. 3.6.

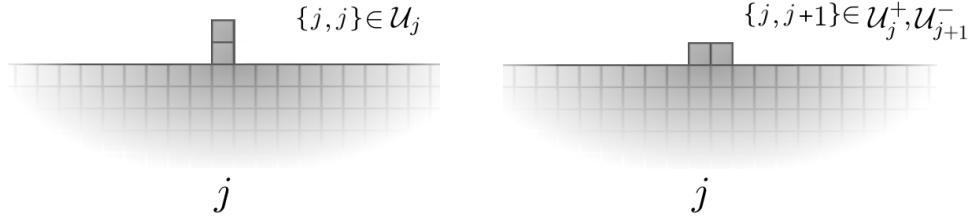


Figure 3.5: Transitions that leave the adatom density unchanged. The density $c_j(t)$ is not changed by any transition in which the lattice site j (relative to the step) is occupied by at least one adatom before and after the transition. The correction terms appearing in the second line of Eq. (3.44) remove such transitions from the equation for \dot{c}_j . See Eq. (3.39) and Remark 3.5.1.

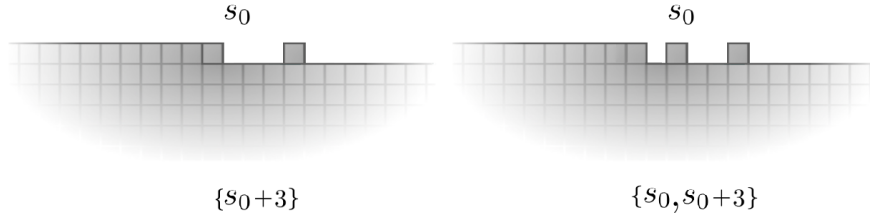


Figure 3.6: Schematic of the effect of step motion on adatom density. When a step moves via an attachment or detachment process, all adatoms change their position relative to the step. Hence, such transitions also change the density $c_j(t)$ [cf. Eq. (3.39)]. The correction terms appearing in the third and fourth lines of Eq. (3.44) account for such changes.

By applying a time derivative to $c_1(t)$, we find

$$\begin{aligned}
\dot{c}_1(t) &= D[c_{s_0}^+ - 2c_1 + c_2] + D[c_1(1 - \phi_+) + (k/a)\phi_+ - c_{s_0}^+] \\
&\quad - D \sum_{\alpha \in \mathcal{F}_d} k\phi_+ \tilde{p}_\alpha + D \sum_{\alpha \in \mathcal{F}_a^+} \phi_+ \tilde{p}_\alpha + D \sum_{\alpha \in \mathcal{U}_1} \tilde{p}_\alpha - D \sum_{\alpha \in \mathcal{U}_1^+} \tilde{p}_\alpha \\
&\quad - D \sum_{\alpha \in \mathcal{D}_1} k\phi_- \tilde{p}_\alpha + D \sum_{\alpha \in \mathcal{A}_2^+} \phi_- \tilde{p}_\alpha, \tag{3.51}
\end{aligned}$$

where the last two lines are correction terms accounting for processes that (i) are forbidden in our kMC rules (via \mathcal{F}_d and \mathcal{F}_a^+), (ii) leave the density of adatoms unchanged (via \mathcal{U}_1 and \mathcal{U}_1^+), or (iii) cause the step to move (relative to the adatom) by means of a detachment (\mathcal{D}_1) or attachment (\mathcal{A}_2^+) process. The density $c_{s_0}^+$ is a new variable that we introduce in order to make the evolution equation for $\dot{c}_1(t)$ take the same form as Eq. (3.44). We therefore assume that

$$D[c_1(1 - \phi_+) + (k/a)\phi_+ - c_{s_0}^+] - D \sum_{\alpha \in \mathcal{F}_d} k\phi_+ \tilde{p}_\alpha + D \sum_{\alpha \in \mathcal{F}_a^+} \phi_+ \tilde{p}_\alpha = 0, \tag{3.52}$$

which determines the boundary condition for c_1 at the right of the step; we group the correction terms associated with forbidden processes with the kinetic relation Eq. (3.52), since these are the same correction terms appearing in Eq. (3.40). We identify $c_{s_0}^+$ as the discrete analogue of c^+ appearing in Eq. (3.2), i.e. as the adatom density at the right of the step edge.

Similarly, by applying a time derivative to $c_{-1}(t)$ we find

$$\begin{aligned}
\dot{c}_{-1}(t) &= D[c_{s_0}^- - 2c_{-1} + c_{-2}] + D[c_{-1}(1 - \phi_-) + (k/a)\phi_- - c_{s_0}^-] \\
&\quad - D \sum_{\alpha \in \mathcal{F}_d} k\phi_- \tilde{p}_\alpha + Da \sum_{\alpha \in \mathcal{F}_a^+} \phi_- \tilde{p}_\alpha + D \sum_{\alpha \in \mathcal{U}_{-1}} \tilde{p}_\alpha - D \sum_{\alpha \in \mathcal{U}_{-1}^-} \tilde{p}_\alpha \\
&\quad + D \sum_{\alpha \in \mathcal{D}_{-2}} k\phi_+ \tilde{p}_\alpha - D \sum_{\alpha \in \mathcal{A}_{-1}^+} \phi_+ \tilde{p}_\alpha. \tag{3.53}
\end{aligned}$$

The correction terms in the second and third lines of Eq. (3.53) have similar interpretations as those appearing in Eq. (3.51); we use $c_{s_0}^-$ in the same way as $c_{s_0}^+$, i.e. to make Eq. (3.53) have the same form as Eq. (3.44). To find a boundary condition for $c_{-1}(t)$, we set

$$D[c_{-1}(1 - \phi_-) + (k/a)\phi_- - c_{s_0}^-] - D \sum_{\alpha \in \mathcal{F}_d} k \phi_- \tilde{p}_\alpha + Da \sum_{\alpha \in \mathcal{F}_a^+} \phi_- \tilde{p}_\alpha = 0. \quad (3.54)$$

Remark 3.5.3 All of the correction terms appearing in Eqs. (3.40)–(3.54) contain either probabilities p_α in which $|\alpha| \geq 2$ or are proportional to kp_α , with $|\alpha| \geq 1$. By the maximum principle of Sec. 3.5.3, these corrections are all negligibly small.

3.5.3 Maximum principle for the m-particle model

In this section, we determine a set of near-equilibrium conditions ensuring that the correction terms appearing in Eqs. (3.44)–(3.53) remain small for all times $t > 0$.

Proposition 3.5.1 *Assume that $p_\alpha(t)$ is the solution to $\dot{p}_\alpha(t) = T_{\alpha, \alpha'} p_{\alpha'}(t)$, where $T_{\alpha, \alpha'}$ is given by Eqs. (3.5)–(3.10) (summation is implied over repeated multi-sets). Moreover, assume that $|\alpha| \leq m$ for all α , where m is some positive integer, and define $\hat{p}_\alpha(t) := p_\alpha(t)/k^{|\alpha|}$. Then $\hat{p}_\alpha(t)$ satisfies the maximum principle that $\max_{\alpha} \{\hat{p}_\alpha(t)\} \leq \max_{\alpha} \{\hat{p}_\alpha(0)\}$ for all times $t > 0$.*

Proof We proceed by *reductio ad absurdum*. Written in terms of the rescaled probabilities \hat{p}_α , Eq. (3.4) becomes

$$k^{|\alpha|} \frac{d\hat{p}_\alpha}{dt} = \sum_{\alpha'} \mathcal{T}_{\alpha, \alpha'} k^{|\alpha'|} \hat{p}_{\alpha'}(t) \quad (3.55)$$

(we now write summations explicitly to avoid confusion). Suppose that there is a maximum $\hat{p}_\alpha(t)$ at some time t , i.e. $\hat{p}_\alpha(t) \geq \hat{p}_{\alpha'}(t)$ for all $\alpha' \neq \alpha$ and $d\hat{p}_\alpha/dt \geq 0$. Recalling Eq. (3.10), we conclude that

$$\sum_{\substack{\alpha' \\ \alpha' \neq \alpha}} \mathcal{T}_{\alpha, \alpha'} \mathfrak{b}_{\alpha'} k^{|\alpha'|} \leq k^{|\alpha|} \sum_{\substack{\alpha' \\ \alpha' \neq \alpha}} \mathcal{T}_{\alpha', \alpha}, \quad (3.56)$$

where $\mathfrak{b}_{\alpha'} := \hat{p}_{\alpha'}/\hat{p}_\alpha \leq 1$ by assumption. We now compare elements of each sum term by term in Eq. (3.56). In view of Eqs. (3.5)–(3.10), we consider three possible cases, (i)–(iii) (summation is not implied over repeated indices):

- (i) if $|\alpha| = |\alpha'|$, then $\mathcal{T}_{\alpha, \alpha'} = \mathcal{T}_{\alpha', \alpha}$;
- (ii) if $|\alpha| = |\alpha'| + 1$, then $\mathcal{T}_{\alpha, \alpha'} k^{|\alpha'|} = \mathcal{T}_{\alpha', \alpha} k^{|\alpha|}$; and
- (iii) if $|\alpha| = |\alpha'| - 1$, then $\mathcal{T}_{\alpha, \alpha'} k^{|\alpha'|} = \mathcal{T}_{\alpha', \alpha} k^{|\alpha|}$.

Comparing the right- and left-hand sides of Eq. (3.56), we therefore see that the inequality only holds when $\mathfrak{b}_{\alpha'} = 1$ for every α' , which concludes the proof.

Corollary 3.5.1 *Assume that $p_\alpha(0) \leq \mathcal{O}(k^{|\alpha|})$. Then $p_\alpha(t) \leq \mathcal{O}(k^{|\alpha|})$ for all times t .*

Definition 3.5.2 *Whenever the initial data satisfies $p_\alpha(0) \leq \mathcal{O}(k^{|\alpha|})$ according to Corollary 3.5.1, we define the state of the system to be near equilibrium. We refer to the hypotheses of Corollary 3.5.1 as “near-equilibrium conditions.”*

Remark 3.5.4 Corollary 3.5.1 defines the conditions under which the discrete BCF equations are valid to $\mathcal{O}(k)$ for all times.

3.5.4 Continuum limit of the m-particle model

In this section, we formally derive the continuum limit of Eqs. (3.40)–(3.53) in 1+1 dimensions. We begin with the assumption that as $a \rightarrow 0$, the function $\hat{p}_\alpha(t) \rightarrow \hat{p}(\mathfrak{r}, t)$, where \mathfrak{r} is an unordered multiset whose elements (which have units of length) may take any continuous value from 0 to L . We further assume that $\hat{p}_\alpha(t) - \hat{p}_{\alpha'}(t) = \mathcal{O}(a)$ for all $t > 0$ and all pairs α and α' (with $\alpha \neq \alpha'$) for which $\mathcal{T}_{\alpha, \alpha'} \neq 0$.¹⁰

Under these assumptions, $c_j(t) \rightarrow c(x, t)$ where x is a continuous variable, $0 \leq x \leq L$. Furthermore, as $a \rightarrow 0$ we find

$$\frac{c((j+1)a, t) - c(ja, t)}{a} = \partial_x c(x, t) + \mathcal{O}(a), \quad (3.57)$$

$$\frac{c((j+1)a, t) - 2c(ja, t) + c((j-1)a, t)}{a^2} = \partial_{xx} c(x, t) + \mathcal{O}(a). \quad (3.58)$$

Next, we set $\mathcal{D} = Da^2$, where \mathcal{D} is a macroscopic diffusivity that should remain bounded as $N \rightarrow \infty$. We also impose the condition $0 < \mathcal{K} = Nk \ll 1$ as $N \rightarrow \infty$ and assume that the system is near-equilibrium (cf. Remark 3.5.4). Under these assumptions, we find that step velocity law Eq. (3.40) is recast in the form

$$\dot{c}(t) = \mathcal{D}\phi_+(c^+ - c^{\text{eq}}) + \mathcal{D}\phi_-(c^- - c^{\text{eq}}) + (\mathcal{D}/L)\mathcal{O}(\mathcal{K}k). \quad (3.59)$$

In Eq. (3.59), we therefore identify $\mathcal{D}\phi_\pm$ as $a\kappa_\pm$, where a is the atomic length in the BCF model. In order to show that the correction is $\mathcal{O}(\mathcal{K}k)$, consider the second

¹⁰A rigorous proof of this claim would require a study of *a priori* estimates for the discrete equations, which we do not pursue here.

line of Eq. (3.40); for example, the term

$$Da \sum_{\alpha \in \mathcal{F}_a^+} \phi_+ p_\alpha \leq DaC \sum_{n=2}^{n=m} N^{n-2} k^n = (\mathcal{D}/L) \mathcal{O}(\mathcal{K}k), \quad (3.60)$$

where C is some constant that is independent of \mathcal{K} and k ; see also Remarks 3.5.3 and Proposition 3.5.1.

Under these assumptions, Eq. (3.44) becomes

$$\partial_t c(x, t) = \mathcal{D} \partial_{xx} c(x, t) + (\mathcal{D}/L^3) \mathcal{O}(\mathcal{K}^2). \quad (3.61)$$

To verify the size of the $\mathcal{O}(\mathcal{K}^2)$ correction, note that all of the corrections to Eq. (3.44) contain differences $p(\alpha a, t) - p(\alpha' a, t) = \mathcal{O}(ak^{|\alpha|})$ for which $T_{\alpha, \alpha'} \neq 0$. Consequently, we may write, for example,

$$-D \sum_{\alpha \in \mathcal{U}_j^-} \tilde{p}_\alpha + 2D \sum_{\alpha \in \mathcal{U}_j} \tilde{p}_\alpha - D \sum_{\alpha \in \mathcal{U}_j^+} \tilde{p}_\alpha \leq C(\mathcal{D}/L^3) \sum_{n=2}^{n=m} (Nk)^n = (\mathcal{D}/L^3) \mathcal{O}(\mathcal{K}^2), \quad (3.62)$$

where C is a constant.

By applying the same arguments to Eqs. (3.52) and (3.54), we find

$$J_\pm = -\mathcal{D} \partial_x c(x, t) = \mp \kappa_\pm (c^\pm - c^{\text{eq}}) + (\mathcal{D}/L^3) \mathcal{O}(\mathcal{K}k), \quad (3.63)$$

where we identify $\kappa_\pm = Da\phi_\pm = \mathcal{D}\phi_\pm/a$ and $c^{\text{eq}} = \mathcal{K}/L$.

As $a \rightarrow 0$, we find that $\kappa_\pm \rightarrow \infty$ provided ϕ_\pm remains bounded. Hence, our analysis implies that in the absence of an attachment barrier, i.e. $\phi_\pm = 1$, the system is in a diffusion limited regime, in which detachment from the step is a fast process relative to diffusion. If $\phi_\pm = \mathcal{O}(N^{-1})$ as $N \rightarrow \infty$, then κ_\pm remains bounded, and the system moves into an attachment/detachment limited regime in which diffusion is the fastest process [95].

The two regimes for κ_{\pm} also suggest that the timescale on which the step moves depends critically on the behavior of ϕ_{\pm} as $N \rightarrow \infty$. In particular, if $\phi_{\pm} = \mathcal{O}(N^{-1})$, then multiplying both sides of Eq. (3.59) by N implies that $Nd\zeta(t)/dt$ is $\mathcal{O}(1)$; that is, the step moves on a macroscopic timescale for which $t/N = \mathcal{O}(1)$. In studies of the BCF theory, this regime is typically called the *quasi-static regime* [8]; physically, the system is able to equilibrate on a timescale much shorter than the step motion.

Remark 3.5.5 *The identity $c^{\text{eq}} = k/a \propto \exp(-E_b/k_B T)$ suggests that $-E_b = \mu$, where μ is the step chemical potential, i.e. the energy of adding an adatom to the step [8].*

Remark 3.5.6 In Fig. 3.7, we compare kMC simulations (described in Sec. 2.2) with the linear kinetic relation Eq. (3.63). Notably, the simulations are in excellent agreement with our definitions of κ_{\pm} and c^{eq} when c^+ is within about 20% of the value of c^{eq} . This range is consistent with our prediction that the BCF theory should approximate the kMC model whenever the system is near-equilibrium, i.e. when $c = \mathcal{O}(c^{\text{eq}})$.

3.6 Discussion

In this section, we (i) consider our results in the context of experimental systems, (ii) review key assumptions underlying our SLG model and indicate why they are physically acceptable, and (iii) discuss limitations of our model.

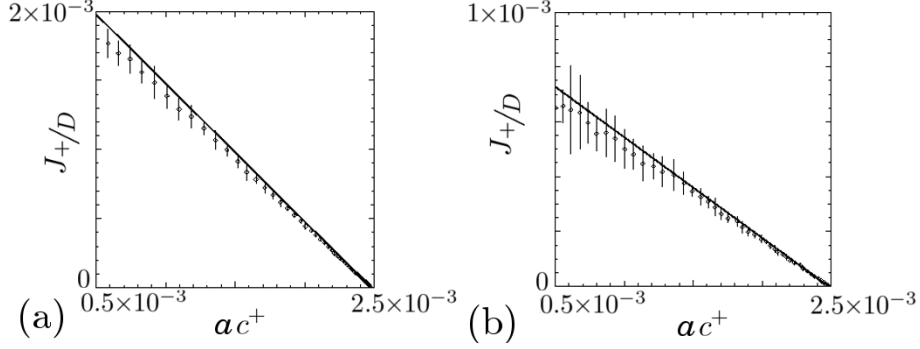


Figure 3.7: Linear kinetic relation Eq. (3.63) versus kMC simulations. (a) Simulations with $\phi_+ = 1$. (b) Simulations with $\phi_+ = 1/e$. In both plots, we take $k \approx 0.025$, $D = 10^{10} \text{ s}^{-1}$, and $N = 30$ (so $a = L/30$); note that $ac^{\text{eq}} = k$. The slopes of the solid lines are (a) $J_+/[D(ac^+ - k)] = -1$ and (b) $J_+/[D(ac^+ - k)] = -1/e$, in agreement with our BCF-type model.

3.6.1 Comparison with real material parameters

In our analysis, we require that $D = \mathcal{O}(N^2)$ and $Nk \ll 1$ as $N \rightarrow \infty$ in order to derive BCF equations in the continuum limit. The second condition ($Nk \ll 1$) in particular allows us to invoke the low-density approximation. In this section, we discuss the validity of these conditions in the context of real material systems.

The hopping rate D is defined as the Arrhenius function $D := f e^{-E_h/k_B T}$, where $f = 10^{13} \text{ s}^{-1}$ is the attempt frequency and E_h is an activation energy that is extracted from measurements [56]. Typical values for E_h range from 0.04 eV for Al(111) to 0.97 ± 0.07 eV for Si(111) [8]. At temperatures between 300 K and 1000 K, we estimate that $10^{12} \text{ s}^{-1} \geq D \geq 10^6 \text{ s}^{-1}$, depending on the material. As an example, we consider Ni(110), for which $E_h = 0.41$ eV [8, 96]; taking $T \approx 500$ K (or $k_B T \approx 1/24$ eV), we estimate that $D = 10^8 \text{ s}^{-1}$. For a terrace with $N = 1000$ lattice sites and $L = 0.1 \text{ } \mu\text{m}$ (i.e. atomic length $a = 0.1$ nm), we find $\mathcal{D} = D/(a^2) = 1 \text{ } \mu\text{m}^2 \text{ s}^{-1}$.

Experiments can also estimate the energy E_b [cf. Eq. (2.7)]. Typical values range from approximately 0.3 eV for Ni(110) [96]¹¹ up to 1 or 2 eV for Si(111) [97–99]. The use of the value $E_b = 0.3$ eV for Ni(110) [cf. Eq. (2.7)] yields $k \approx 10^{-4}$ at 500 K. By combining this result with the assumption that $N = 1000$ (corresponding to L that is a few hundred nanometers), we find that $Nk \approx 10^{-1}$, which suggests that the low-density approximation is reasonable for this system at 500 K. In addition to these formal estimates, both experimental and numerical results have verified that Ni(110) is in a low-density regime at this temperature; see [96]. In this work, significant adatom detachment on Ni(110) only began when the temperature was raised above 650 K; at 900 K, simulations show that roughly 1.5% of the lattice sites are occupied by adatoms (see also [91]).

Experimental estimates of E_{\pm} are also available [cf. Eq. (2.6)]. Often (but not always) the Ehrlich-Schwoebel barrier [64,65] E_- is larger than the attachment barrier E_+ . See, e.g., Table 6 in [8] for a detailed list of attachment/detachment barriers.¹² For Ni(110), one finds $E_- = 0.9$ eV and $E_+ \approx 0$ eV, which implies $\phi_- \ll 1/N$ and $\phi_+ = 1$ at 500 K. In a BCF model for this system, we therefore expect that $\kappa_- \approx 0$ and $\kappa_+ = \mathcal{O}(N)$, corresponding to $\mathcal{J}_- = 0$ and $c_+ = c^{\text{eq}}$ (see Sec. 3.5.4). Therefore for this system, our analysis predicts different boundary conditions on each side of the step edge.

¹¹In [96], the activation energy E_a for creating an adatom is equal to $E_h + E_b$ in our model. Noting that $E_a \approx 0.7$ eV in [96] and $E_h \approx 0.4$ eV in [8,96] yields $E_b \approx 0.3$ eV.

¹²The attachment/detachment barriers in Table 6 of [8] are not the same as E_{\pm} in Eq. (2.6). In Ref. [8], the definitions of $E_{a,u}$ and $E_{a,l}$ correspond to $E_h + E_-$ and $E_h + E_+$ in our model. Our E_{\pm} is the *excess* energy, relative to the hopping barrier, required for adatom attachment/detachment.

3.6.2 Consequences of dimensionality

Rules 2.2.1–2.2.5 impose several restrictions on the allowed atomistic transitions. In this section, we briefly discuss the physical motivation of these restrictions as well as implications of relaxing them.

In both the kMC simulations of Sec. 2.2 and master equation (3.5)–(3.10) of the m-p model, we ignore adatom-pair interactions; see Remark 2.2.2. If we relax this assumption by allowing nearest-neighbor adatom interactions, then the energy cost to make any *single* island should be constant, irrespective of its size (cf. Fig. 3.8); by Boltzmann statistics, all island sizes are equally probable at equilibrium (for a fixed number of islands and a single step). On the other hand, in 2+1D the probability of finding an island should decrease with its size (i.e. the number of broken bonds); see Fig. 3.8. Therefore, we exclude adatom interactions in our 1D model on the grounds that such interactions do not capture the physics of island formation. Our model also neglects processes that allow steps to move by more than one lattice site at a time; see Remark 2.2.3. If we relax this assumption by allowing a step atom to move while still forbidding adatom interactions, the step atom must break $n + 1$ bonds, where n is the number of atoms to the right of the moving atom. We forbid such processes on the grounds that they are unphysical, since the step atom only has two nearest neighbor bonds. In a 2D setting where it is reasonable to allow adatom interactions, the detachment of step atoms is a physically acceptable process because it only breaks nearest-neighbor bonds.

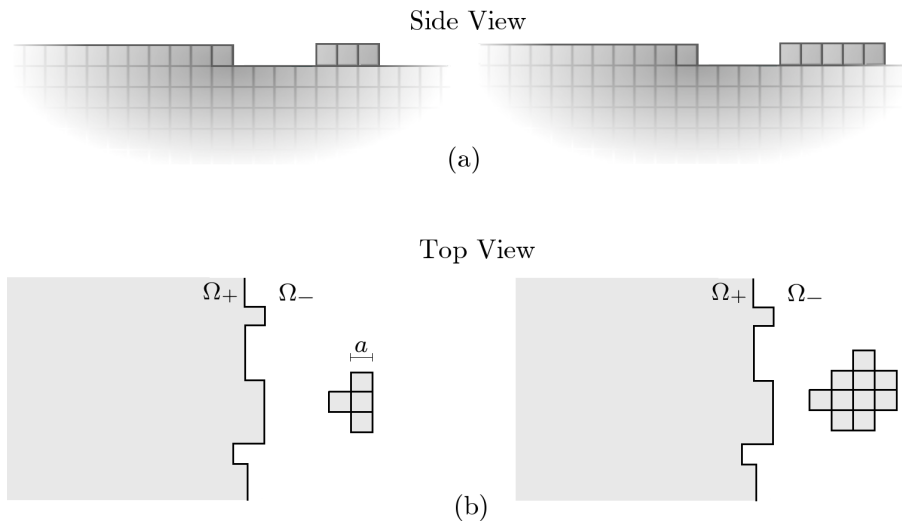


Figure 3.8: Islands in 1D versus 2D. In this figure, we assume that adatoms interact (i.e. form bonds) with their nearest neighbors. (a) 1D: all islands have 2 broken bonds. (b) 2D: smaller islands (left) have less broken bonds than larger islands (right). The symbol Ω_{\pm} denotes the upper (+) and lower (-) terraces. Since the energy cost to create an island increases with the number of broken bonds, larger islands are typically less probable than small islands.

3.6.3 Limitations of the atomistic model

Our SLG model has limitations due to the fact that we only consider a single step in 1D. In this setting, it is not possible to derive step interactions. In many formulations of the BCF theory, such interactions introduce an additional energy into the step chemical potential, so that the energy cost of adatom detachment depends on the widths of the terraces adjacent to the step [8,24,26,40]. We speculate that in an appropriate multi-step SLG model, this energy penalty should appear as an additional, configuration dependent contribution to E_b .

Because our SLG model is only 1D, we cannot account for the effects of anisotropy in the crystal lattice. Such effects could be important in systems such as Si(001), where diffusion rates are both direction and position dependent [97,98]. We speculate that an appropriate SLG model incorporating these features would lead to a BCF model with an anisotropic and (potentially) position dependent diffusion coefficient.

Our analysis is also unable to determine the role that kinks play in the derivation of BCF-type models. In 2D SLG models, it is known that kinks, which alter the microscopic step profile, play an important role in determining the rates of adatom attachment/detachment processes. Moreover, in 2D BCF-type models, the chemical potential (i.e. the energy cost to remove an adatom from a step), and consequently the linear kinetic relations are typically assumed to depend on the local step curvature [40]. However, a derivation that expresses this dependence remains an open question.

3.7 Summary

In this chapter, we formally derived a BCF-type model, with correction terms, from a SLG master equation for a single step in 1D. The central idea of our approach was to exploit the fact that, in the atomistic model, the number of adatoms on the surface is typically small. By invoking near-equilibrium statistical mechanics and the Boltzmann distribution, we showed how to interpret the basic ingredients of the BCF theory (i.e. the step position and adatom density) as arising from the notions of ensemble averages of appropriate microscopic quantities. In addition, we studied corrections to the BCF theory, which account for adatom correlations. In the low-temperature regime, we used a maximum principle to show that the corrections remain small for all times, provided they are initially small; we identified this restriction on the initial data as a near-equilibrium condition (cf. Definition 3.5.2). Our analysis (i) revealed the regions of parameter space in the SLG model that lead to diffusion-limited kinetics and attachment/detachment-limited kinetics in the BCF-type model, and (ii) indicated the atomistic origin (coming from the energy barriers of the SLG model) of the step chemical potential for the step-continuum system.

In the context of our atomistic perspective, we believe that our averaging procedure implied by (3.38) is the first instance of an analytic definition of a step. This definition allowed us to derive a BCF-type model, specifically the step velocity law and linear kinetic relations at the step edge.

Our analysis leaves several open questions. Because our SLG model contains a single step, we are not able to account for step interactions or study step bunching

instabilities. Moreover, the 1D nature of our analysis prohibits us from determining the roles that lattice anisotropy and kinks play in the derivation of BCF-type models. In particular, an important task is to derive the 2D step chemical potential and the Bales-Zangwill instability, which are expected to depend on the step curvature.

Chapter 4

Terrace-width fluctuations: stochastic Burton-Cabrera-Frank model

Stochastic fluctuations are ubiquitous in material systems. Such phenomena, when coupled with non-linear evolution laws, can lead to rich, but complicated behavior. Because vicinal surfaces can be experimentally probed over a wide range of length scales,¹ these systems provide a fertile testing ground on which to develop analytic methods that can be applied to non-equilibrium statistical mechanics.

In this chapter, we use the BCF theory to study the interplay between such non-linear evolution laws and fluctuations. Our main goal is to derive a formula for the terrace-width distribution (TWD), the probability that a terrace has a given width.² A related goal is to develop asymptotic methods that are useful for solving systems of stochastic differential equations (SDEs). Similar problems have been the subject of extensive studies, both experimental and theoretical [8, 40, 43, 104, 110].

This chapter is organized as follows. Section 4.1, we discuss the main ideas and context surrounding this problem. In Sec. 4.2, we (i) introduce a stochastic BCF model, which is a generalization of the model considered Chapter 3, and (ii) derive non-linear stochastic differential equations (SDEs) for the time-evolution of terraces.

¹Scanning-tunneling microscopes have sub-nanometer resolution, while tools such as low energy electron microscopy can resolve length scales as large as a few microns [8].

²Mathematically speaking, the TWD is actually a probability *density*, not a distribution. However, the word distribution is conventionally used in the context of vicinal surfaces.

In Sec. 4.3, we use the notion of BBGKY hierarchies to formulate a self-consistent, mean-field (MF) equation for the TWD. In Sec. 4.4, we discuss an approximation scheme for solving the mean-field equation, and in Sec. 4.5, we discuss extensions and limitations of our treatment. Section 4.6 summarizes our results.

4.1 Key ideas

In this chapter, we consider a generalization of the BCF-type theory of Chapter 3; in particular, we study a 1D system of $N > 1$ monotonic steps that interact entropically or as elastic dipoles; these interactions are introduced via the step chemical potential (cf. Rem 3.5.5). We derive a system of non-linear evolution equations for the terrace widths $\mathbf{w} = (w_0, \dots, w_{N-1})$ and add to these equations a noise term. This procedure yields a system of coupled, stochastic differential equations for the TWD, which has the form

$$\dot{\mathbf{w}}(t) = \mathbf{A}(\mathbf{w}) + \mathbf{Q} \cdot \boldsymbol{\eta}(t) . \quad (4.1)$$

Here the symbol \mathbf{A} is an N -dimensional vector encapsulating step-step interactions and in principle depending on \mathbf{w} non-linearly; \mathbf{Q} is the $N \times N$ diffusion coefficient, and $\boldsymbol{\eta} = (\eta_0, \dots, \eta_{N-1})$ is the vector-valued Gaussian white noise [100], which we use to model thermal fluctuations and couplings with the environment. *Our main goal is to develop asymptotic methods of solving this system of SDEs.*

The key idea of our analysis is to reduce this large system of SDEs to a pair of equations via a mean-field approximation. Specifically, we isolate the SDE for an arbitrary terrace width and assume that a single unknown function f may

replace all other terrace widths in that equation. Then, on the basis of kinetic Bogoliubov-Born-Green-Kirkwood-Yvon (BBGKY)-type hierarchies [6] for terrace-terrace correlation functions, we derive a self-consistency equation for this unknown function.³

However, the self-consistency equation alone does not reduce the dimensionality of the SDEs; the former depends not only on the TWD, but also on higher-order correlation functions, i.e. joint probabilities for adjacent terrace widths. We employ a *decorrelation ansatz* in which we assume that joint probability densities can be written as products of TWDs. Importantly, this assumption allows us to write the consistency equation entirely in terms of the mean field f and the TWD, effectively closing the system of two equations. The decorrelation ansatz is ultimately justified by comparing our results with kMC simulations, which have two free parameters (cf. Appendix B).

In contrast to the previous chapter, we do not derive the multi-step BCF model that we employ here; neither do we derive the form of the noise in Eq. (4.1). In general, extending the analysis of Chapter 3 to accomplish these tasks is an open challenge. However, our *ad hoc* approach, where the model equations and form of noise are assumed (rather than derived by first principles) has been motivated by [43, 101]. Therefore, to allow for some flexibility in modeling, we consider three forms of \mathbf{Q} amounting to: (i) $(\mathbf{Q} \cdot \boldsymbol{\eta})_j = \eta_j(t)$, i.e., the usual non-conservative white noise; (ii) $(\mathbf{Q} \cdot \boldsymbol{\eta})_j = \eta_{j+1} - \eta_j$, a first-order conservative scheme; and (iii)

³More accurately, the function f is a self-consistent field. However, we use the terminology mean field since there is some precedent for its use in the context of the BCF theory [104].

$(\mathbf{Q} \cdot \boldsymbol{\eta})_j = \eta_{j+1} - 2\eta_j + \eta_{j-1}$, a second-order conservative scheme.⁴ We show that only choice (iii) is compatible with the requirements of a fixed system size and finite TWD variance.

As in the previous chapter, the analysis here is limited by the 1D character of the geometry. In particular, meandering and curvature are not considered. This simplification yields, as an artifact, a singularity of the TWD at zero terrace width, which mathematically enforces a step noncrossing condition. Another limitation comes from the application of a mean-field, whose existence we assume but do not prove. In using the MF, we are also compelled to apply the decorrelation ansatz. This hypothesis is not strictly satisfied in step systems, but interestingly, we find agreement of our MF solution with 1D kMC simulations for moderate to strong step interactions; see also Appendix B. Open questions remain regarding the best way to improve the predictive power of our MF approach in the weak-interaction limit.

Notation and terminology. Throughout the chapter, we adhere to certain notation conventions, which differ somewhat from the previous chapter.

- Vectors are lowercase and matrices uppercase; both objects are boldface unless we indicate otherwise.
- For any *circulant* matrix $\mathbf{\Lambda}$, the (nonnegative) quantity $|\mathbf{\Lambda}|^2$ is the sum of the magnitudes squared of elements of the first row of $\mathbf{\Lambda}$.
- The symbol \mathbb{R}_n^+ denotes the region of the n -dimensional Euclidean space (\mathbb{R}_n)

⁴In this context, conservative means that the sum of elements in any row or column of \mathbf{Q} is zero.

with nonnegative coordinates.

- We do *not* distinguish the terms “distribution” and “probability density.”
- We reserve the symbol $P(s, t)$ for the TWD and $p_{(n)}(s, t)$ for the joint probability density of any n consecutive terraces (if $n \geq 2$).
- We use $P_n(s, t)$ (but not $P_{(n)}(s, t)$!) to represent the n th term in a perturbation series for $P(s, t)$.
- We again adopt the Einstein summation convention.

4.2 Burton-Cabrera-Frank model of interacting steps

In this section, we present the BCF-type model used in this chapter.

4.2.1 Deterministic equations

We start by considering a 1D train of N steps which have (constant) height a and are descending in the positive x direction (see Fig. 4.1).⁵ For simplicity of notation, we take the lattice to be simple cubic, with terraces in an $\{001\}$ direction, so that the in-plane square lattice also has lattice constant a . Let the step positions be labeled by an (integer) index, j , where $j = 0, 1, \dots, N - 1$. Define the j th terrace width by $w_j = x_j - x_{j-1}$; see Fig. 4.1. We apply screw periodic boundary conditions, so that the steps are mapped onto particles on a ring [43, 101].

⁵Here we take a to be a non-zero constant even though we took the limit $a \rightarrow 0$ to derive our BCF-type theory in the previous chapter.

Let \tilde{t} be the physical (dimensional) time. The number density, $c_j(x, \tilde{t})$, of adatoms on the j th terrace solves the equation [16]

$$\mathcal{D}\partial_{xx}c_j(x, \tilde{t}) = \partial_{\tilde{t}}c_j(x, \tilde{t}) \quad \text{for } x_{j-1} < x < x_j, \quad (4.2)$$

subject to the boundary conditions [8, 102, 103]

$$\begin{aligned} \mathcal{J}_j^- &= \kappa_- [c_j(x_j) - c_j^{\text{eq}}], \\ \mathcal{J}_{j-1}^+ &= \kappa_+ [c_j(x_{j-1}) - c_{j-1}^{\text{eq}}]. \end{aligned} \quad (4.3)$$

As in Chapter 3, \mathcal{D} is the terrace diffusivity and \mathcal{J}_j^\pm is the mass flux impinging on the j th step from right (+) or left (−) with kinetic rates κ_\pm [64, 65]. The quantity c_j^{eq} is the equilibrium adatom concentration at the j th step edge, and is given by the near-equilibrium relation [8]

$$c_j^{\text{eq}} = c_s \exp\left(\frac{\mu_j}{k_B T}\right) \simeq c_s \left(1 + \frac{\mu_j}{k_B T}\right), \quad (4.4)$$

if $|\mu_j| \ll k_B T$. Note that μ_j is the j th-step chemical potential, c_s is a material-dependent constant, and $k_B T$ is the Boltzmann energy. For entropic and elastic-dipole step interactions, μ_j is expressed as [8]

$$\mu_j = \tilde{g}a^3 \left(\frac{1}{w_{j+1}^3} - \frac{1}{w_j^3}\right), \quad \tilde{g} > 0, \quad (4.5)$$

where the coupling constant \tilde{g} has units of energy.⁶

To solve Eq. (4.2), we adopt the *quasi-static approximation*, by which each $c_j(x, \tilde{t})$ is assumed to reach its steady state much faster than steps move (cf. Sec. 3.5.4).⁷

⁶For no step interactions, $\mu_j = 0$, which leads us to speculate that $c_s = k/a$ as defined in the previous chapter.

⁷The use of the quasi-static approximation in the stochastic setting that follows is justified when the amplitude of noise is weak, so that steps still move slowly relative to adatom diffusion.

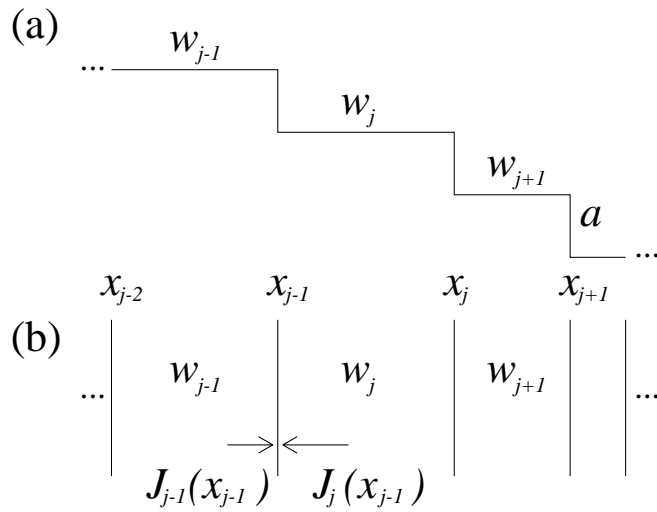


Figure 4.1: Side and top views of step system. Steps have height a and positions x_j , and $w_j = x_j - x_{j-1}$. (a) Side view: Steps descend for increasing x . (b) Top view: The directions and magnitudes of adatom fluxes $J_{j-1}(x)$ and $J_j(x)$ at $x = x_{j-1}$ are represented by arrows; by Eq. (4.7), the $(j - 1)$ th step edge moves to the right.

Hence, set $\partial_{\tilde{t}}c_j(x, \tilde{t}) \equiv 0$ for every j . Accordingly, the adatom flux on the j th terrace, $J_j(x, \tilde{t}) = -\mathcal{D}\partial_x c_j(x, \tilde{t})$, is a constant,

$$J_j(x) = \mathcal{D} \frac{c_{j-1}^{\text{eq}} - c_j^{\text{eq}}}{\frac{\mathcal{D}}{\kappa_-} + \frac{\mathcal{D}}{\kappa_+} + w_j} \quad \text{for } x_{j-1} < x < x_j . \quad (4.6)$$

By Eq. (4.3), in the quasi-static approach we use $\mathcal{J}_{j-1}^+ = -J_j(x_{j-1})$ and $\mathcal{J}_j^- = J_j(x_j)$ since any convective contributions to \mathcal{J} due to the step velocity are negligible.

By mass conservation, the j -th step velocity is [8, 16]

$$\dot{x}_j(\tilde{t}) = \frac{dx_j}{d\tilde{t}} = \frac{\Omega}{a}(J_j - J_{j+1}) = a(J_j - J_{j+1}) , \quad (4.7)$$

where $\Omega = a^2$ is the surface atomic area. Equation (4.7), combined with Eqs. (4.4)–(4.6), leads to the following (deterministic) equations of motion for terrace widths:

$$\begin{aligned} \dot{w}_j &= \dot{x}_j - \dot{x}_{j-1} \\ &= 2\check{g}H(w_j; w_{j-1}, w_{j+1}) - \check{g}H(w_{j+1}; w_j, w_{j+2}) - \check{g}H(w_{j-1}; w_{j-2}, w_j), \end{aligned} \quad (4.8)$$

where

$$H(x; y, z) = \frac{1}{\check{c} + x} \left[\frac{2}{x^3} - \left(\frac{1}{y^3} + \frac{1}{z^3} \right) \right]. \quad (4.9)$$

For a vicinal surface, we take the initial condition $w_j(0) = \langle w \rangle$ (although in principle we could start more generally with N constants with average value $\langle w \rangle$).

Here, the parameter $\check{g} = \mathcal{D}c_s\tilde{g}a^4/k_B T$ is a measure of the interaction strength, and $\check{c} = \mathcal{D}(k_+^{-1} + k_-^{-1})$ is a kinetic length expressing the interplay of diffusion and attachment-detachment processes. We render Eq. (4.8) dimensionless by setting $s_j = w_j/\langle w \rangle$ and $t = \tilde{t}/t^*$ where t^* is some time scale, e.g., $t^* = \langle w \rangle^2/\mathcal{D}$. We also define $g = \check{g}t^*/\langle w \rangle^5$ and $c = \check{c}/\langle w \rangle$. We have $\langle s_j \rangle = 1$, which fixes the crystal size.

4.2.2 Interpretation of the interaction parameter

In this subsection, we propose a physical interpretation of the parameter g by discussing how our 1D model may be used to describe “quasi 1D“ systems, i.e. 2D systems in which steps remain relatively straight (see Ref. [8]). If two neighboring, 2D steps remain straight along some length \mathcal{L} , then in order for one step to advance by an amount dw with respect to the other, every element of the moving step must move by the same amount dw . In this sense, we choose to represent quasi 1D systems with Eq. (4.8). In our interpretation, the chemical potential (cf. Eq. (4.5)) is the energy required to simultaneously add an adatom to every site along the length \mathcal{L} of a moving step. Hence, the parameter \tilde{g} is the step interaction energy for an *entire* step to interact with another *entire* step.

In Refs. [8, 42], values of the interaction energy per length are given for several metals and semiconductors in units of $\text{eV}\cdot\text{\AA}^{-1}$. The values in these references account for the interactions between individual *elements* of neighboring steps, as opposed to interactions between entire steps. Typical values for silicon range from a few hundred $\text{meV}/\text{\AA}$ to $1000 \text{ eV}/\text{\AA}$, depending on the orientation of the miscut angle. For $\langle w \rangle = 100 \text{ \AA}$, $c_s \sim 10^{-2} \text{\AA}^{-1}$, $a \sim 5 \text{ \AA}$, and $k_B T \sim 0.1 \text{ eV}$, our model predicts an interaction energy per length $\tilde{g}/\mathcal{L} \sim (g/\mathcal{L}) \cdot 10^5 \text{ eV}$. Hence, the values $g = 1$ and $\mathcal{L} = 10^5 \text{\AA}$ corresponds to a vicinal surface whose steps remain straight for approximately 10^5\AA and have an interaction energy of $1 \text{ eV}/\text{\AA}$, well within the range of values found for different orientations of silicon.

4.2.3 Stochastic equations

To model fluctuations, we add a Gaussian white noise term to Eq. (4.8). Since our approach is ad hoc (i.e., the noise form is assumed and not derived from first principles), we allow for some flexibility in the choice of the noise term. We write

$$\dot{s}_j = \frac{ds_j}{dt} = gA(s_{j-2}, s_{j-1}, s_j, s_{j+1}, s_{j+2}) + Q_{j,l} \eta_l, \quad (4.10)$$

where summation is implied over repeated indices, η_l ($l = 0, \dots, N - 1$) is the Gaussian white noise at the l th step, and $\mathbf{Q} = [Q_{j,l}]$ is some $N \times N$ circulant matrix to be specified below.⁸ Note that before non-dimensionalizing, the coefficient multiplying η_l is $(\mathcal{D}/\langle w \rangle)Q_{j,l}$, which has units of length over time. We also define

$$A(s_{j-2}, s_{j-1}, s_j, s_{j+1}, s_{j+2}) = 2H(s_j; s_{j-1}, s_{j+1}) - H(s_{j-1}; s_{j-2}, s_j) - H(s_{j+1}; s_j, s_{j+2}), \quad (4.11)$$

i.e., the right-hand side of Eq. (4.8) divided by g , where \check{c} is now replaced by c in H [see Eq. (4.9)]. Note that in Eq. (4.10) we single out the constant g . This g influences the time and length scales for the dynamical system. In Secs. 4.4, we show analytically how the singular character of A prohibits step crossing.

4.2.4 Form of noise: relation to a linearized model

In order to solve Eq. (4.10), we require a specific choice for \mathbf{Q} , which is constrained by the physical requirement that the total size of the vicinal crystal be fixed. This requirement implies that summing Eqs. (4.10) over all j should yield a

⁸The restriction that $\mathbf{Q} =$ implies that all terraces experience the same noise.

deterministic evolution equation. Summing Eqs. (4.10) over all j therefore rules out the possibility that $\mathbf{Q} = \mathbf{1}$ (identity matrix).

The finite system-size requirement, however, is not enough to uniquely determine the form of \mathbf{Q} . Here we resort to a linearized version of Eq. (4.10) in order to study the implications of two other possible choices. Later, we will also use this linearized model as a benchmark for the MF approximation developed in Sec. 4.3.

Hence, proceeding under the assumption that $g \gg 1$, we treat the stochastic fluctuation process $\varpi_j = s_j - 1$ as small in the sense that $1 - \text{Prob}\{|\varpi_j| < \epsilon\} \ll 1$ for sufficiently small $\epsilon > 0$ (where the Prob denotes the probability). It is then reasonable to expand the governing Eqs. (4.10) around $\varpi_j = 0$ ($j = 0, \dots, N - 1$). Defining $g_c = 3g/(c + 1)$, we derive the linear SDE system

$$\begin{aligned} \dot{\varpi}_j(x) = & -g_c[6 \varpi_j - 4(\varpi_{j-1} + \varpi_{j+1}) \\ & + \varpi_{j-2} + \varpi_{j+2}] + Q_{j,l} \eta_l, \end{aligned} \quad (4.12)$$

where (abusing notation) we keep the same symbol, ϖ_j , for the approximate solution. In contrast to Refs. [43, 101], where the discrete scheme is of second order, SDEs (4.12) introduce *fourth-order* couplings.

Equation (4.12) is straightforward to solve (cf. Ref. [24] for a full treatment). For the initial condition $\varpi(0) = 0$, the solution is a vector of Gaussian stochastic processes whose variances are all equal and given by⁹

$$\sigma_{\text{lin}}^2(t) = g_c^{-1} \int_0^{g_c t} |e^{-\tau' A} \mathbf{Q}|^2 d\tau'. \quad (4.13)$$

This equation gives a second criterion by which to choose \mathbf{Q} ; specifically, we impose

⁹The solution to Eq. (4.12) has the unphysical property that steps can cross.

the restriction that the variance of any terrace width be finite for all times. In [24], we showed that a first-order conservative noise, corresponding to the circulant matrix \mathbf{Q} with the first row $[1, -1, 0, 0, \dots]$, violates the finite variance condition. The second most simple (yet nontrivial) choice for \mathbf{Q} that gives a finite variance is a *second-order* scheme for a conservative noise. Accordingly, we set the first row of the circulant matrix \mathbf{Q} equal to $[2, -1, 0, \dots, 0, -1]$, which yields

$$\sigma_{\text{lin}}^2(t) = g_c^{-1} \int_0^{g_c t} \frac{4}{N} \sum_{k=0}^{N-1} \left\{ \left[1 - \cos\left(\frac{2\pi k}{N}\right) \right]^2 \times e^{-4\tau' [3 - 4 \cos(\frac{2\pi k}{N}) + \cos(\frac{4\pi k}{N})]} d\tau' \right\} . \quad (4.14)$$

In the limit $N \rightarrow \infty$, this formula may be simplified to yield

$$\sigma_{\text{lin}}^2(t) = \frac{1}{2g_c} \left[1 - \int_0^1 e^{-8g_c t [1 - \cos(2\pi y)]^2} dy \right] , \quad (4.15)$$

which is the variance referred to by the term “linearized model“ (LM) in figures.

We note that together, the fixed system size and finite variance requirements still do not determine \mathbf{Q} uniquely. Hence, while our second-order conservative noise scheme is consistent with the stated constraints, higher-order conservative noise will also yield a finite variance in the long-time limit. Here we make the simplest choice that works.¹⁰

Equation (4.10), with the choice of \mathbf{Q} , are the main results of this section; they form the basis of our subsequent calculations. In Sec. 4.4, we develop techniques for extracting statistical properties of the terrace widths by further analyzing Eq. (4.10) via stochastic calculus and kinetic hierarchies.

¹⁰Specifying the precise conditions needed to define a consistent, unique noise term is an open problem.

4.3 Mean-field formalism

In this section, we introduce a systematic procedure to approximately decouple SDEs (4.10), i.e., reduce them to a single nonlinear SDE, taking into account the full nonlinearity of the step interactions. Our scheme relies on the use of an effective mean field, f , which in principle depends on the dimensionless terrace-width variable, s , and time.

We first consider each of Eqs. (4.10), for fixed j , and replace $s_{j\pm 1}$ and $s_{j\pm 2}$ by $f(s_j, t)$ [43,101,104]. The field f is *not* known a priori but must be determined consistently with the assumption that the resulting SDE generates a TWD sufficiently close to the particular TWD that would arise from solving Eq. (4.10) *exactly*, were this possible [101].¹¹ Our aim in adopting this procedure is to simplify the computations without altering the essential physics of the interactions. While the existence of a field $f(s, t)$ consistent with the original SDEs (4.10) is not guaranteed, our procedure generates results that compare well with simulations (cf. Figs. 4.2 and 4.4.3, as well as Appendix B).

Thus, in brief our goals for this section are: (i) to find heuristically the Fokker-Planck equation (FPE) for the MF TWD (Sec. 4.3.1); (ii) to derive an exact evolution equation for the TWD in terms of joint probability densities (Sec. 4.3.2); and (iii) to determine by self-consistency an equation for the mean field $f(s, t)$ (Sec. 4.3.3). In Sec. 4.4, this MF formalism is used to analytically describe the

¹¹We require that only the TWDs of the exact and MF models, and not higher-order correlation functions, be identical.

TWD in the steady-state and time-dependent cases under the hypothesis of statistical independence for terrace widths.

4.3.1 Mean-field Burton-Cabrera-Frank equations

Consider Eq. (4.10) for fixed j . By the above prescription [43, 101, 104], i.e., replacement of $s_{j\pm 1}$ and $s_{j\pm 2}$ by $f(s_j, t)$ for each j , we obtain the effective SDE

$$\frac{d\hat{s}_j}{dt} = gA(\hat{s}_j, f) + \hat{q}\eta , \quad (4.16)$$

where the hat indicates the MF approximation and $A(s, f)$ is used in place of $A(f, f, s, f, f)$:

$$A(s, f) \equiv A(f(s, t), f(s, t), s, f(s, t), f(s, t)) ;$$

see definition (4.11). Note the coefficient \hat{q} in Eq. (4.16): this \hat{q} is a number, within the MF approximation, that comes from the matrix \mathbf{Q} via treatment of the noise components η_j as statistically independent of each other. For \mathbf{Q} with first row equal to $[2, -1, 0, \dots, 0, -1]$ (second-order conservative scheme), we will determine that $\hat{q}^2 = 6$ (see Sec. 4.3.3). For the time being, we distinguish the MF TWD, $\hat{P}(s, t)$, from the (exact) $P(s, t)$.

Equation (4.16) yields a corresponding FPE for the MF TWD, $\hat{P}(s, t)$ [105]:

$$\partial_t \hat{P}(s, t) + g \partial_s [A(s, f) \hat{P}(s, t)] = \frac{\hat{q}^2}{2} \partial_{ss} \hat{P}(s, t) , \quad (4.17)$$

with the initial and boundary conditions

$$\hat{P}(s, 0) = \delta(s - 1) , \quad (4.18a)$$

$$\frac{\hat{q}^2}{2} \partial_s \hat{P} - gA(s, f) \hat{P} \rightarrow 0 \quad \text{as } s \rightarrow 0^+ , \infty . \quad (4.18b)$$

The initial condition (4.18a) describes a vicinal crystal: the surface slope is constant and all terraces have the same width (scaled to unity). Boundary conditions (4.18b) state that the *probability flux* must vanish as $s \rightarrow 0$ from above and $s \rightarrow \infty$. Thus, steps are prohibited from crossing or moving infinitely far apart.

In Refs. [43, 101, 104], MF descriptions for 1D step models are derived under the assumption that $f(s, t)$ is equal to the *average* terrace width for all times $t > 0$. In Ref. [101], this assumption is shown to be self consistent only for the case of linear SDEs. In the present case, we do not expect the mean field f to coincide with the average terrace width. The determination of f constitutes a complicated problem. The argument that views f as an average of the stochastic process (terrace width) foreshadows the true role of f , namely, to reconcile the asymmetries introduced by the nonlinear step-step interactions with the requirement of fixed system size. In Sec. 4.4, we show how corrections for f in the steady state shift the peak of the TWD to the left of $s = 1$ (average), in agreement with kMC simulations.

4.3.2 Evolution law for terrace-widths via BBGKY hierarchy

In this subsection, we derive an evolution equation for the exact TWD, $P(s, t)$, on the basis of a kinetic hierarchy for joint probability densities of consecutive terraces. This equation serves our purpose of defining a self-consistent $f(s, t)$ (Sec. 4.3.3).

Following the formalism of Ref. [101], we define the N -terrace distribution $p_{(N)}(\mathbf{s}, t)$, where $\mathbf{s} = (s_0, s_1, \dots, s_{N-1})$; hence, $p_{(N)}(\mathbf{s}, t) d\mathbf{s}$ is the probability that N terraces have widths with values in the intervals $(s_k, s_k + ds_k)$ where $k = 0, \dots, N-1$

and $d\mathbf{s} = ds_0 \cdots ds_{N-1}$. The probability density for *any* n consecutive terraces ($n = \mathcal{O}(1) \geq 2$) is defined by

$$p_{(n)}(\mathbf{s}_{(n)}) = \frac{1}{N} \sum_{k=0}^{N-1} \int_{\mathbb{R}_{N-n}^+} d\mathbf{s}_{(N-n)} p_{(N)}(\mathbf{s}_{(n)}, \mathbf{s}_{(N-n)})_k^c, \quad (4.19)$$

where $\mathbf{s}_{(n)} = (s_0, \dots, s_{n-1})$, $\mathbf{s}_{(N-n)} = (s_n, \dots, s_{N-1})$, and \mathbf{z}_k^c denotes the vector formed after k cyclic permutations of coordinates of $\mathbf{z} = (\mathbf{s}_{(n)}, \mathbf{s}_{(N-n)})$. In the above, we do not write the time dependence explicitly. The desired TWD is

$$P(s, t) = \frac{1}{N} \sum_{k=0}^{N-1} \int_{\mathbb{R}_{N-1}^+} d\mathbf{s}_{(N-1)} p_{(N)}((s, \mathbf{s}_{(N-1)})_k^c, t). \quad (4.20)$$

Using Eq. (4.10) we write down the (N -dimensional) FPE for the N -terrace probability density [100, 105]:

$$\begin{aligned} g\partial_{s_l} [A(s_{l-2}, s_{l-1}, s_l, s_{l+1}, s_{l+2}) p_{(N)}(\mathbf{s}, t)] \\ = -\partial_t p_{(N)}(\mathbf{s}, t) + \frac{1}{2} \partial_{s_l} \partial_{s_k} [\mathbf{Q}^2]_{l,k} p_{(N)}(\mathbf{s}, t), \end{aligned} \quad (4.21)$$

where $A(s_{l-2}, s_{l-1}, s_l, s_{l+1}, s_{l+2})$ is defined by Eq. (4.11) and $\mathbf{Q} = \mathbf{Q}^T$ is the circulant matrix whose first row is $[2, -1, 0, \dots, 0, -1]$. Recall that we pick this \mathbf{Q} since the TWD must approach a steady state [see Eq. (4.15)].

To find an evolution equation for $P(s, t)$, apply ∂_t to Eq. (4.20) and use Eq. (4.21). Thus, P satisfies [101]

$$\partial_t P(s, t) = -g\partial_s \int_{\mathbb{R}_4^+} \mathcal{A}(s, \vec{y}) p_{(5)}(s, \vec{y}, t) d\vec{y} + 3\partial_{ss} P(s, t), \quad (4.22)$$

where for notational economy we use $\mathcal{A}(s, \vec{y})$ in place of $A(y_{N-2}, y_{N-1}, s, y_1, y_2)$ and we employ $p_{(5)}(s, \vec{y})$ to mean $p_{(5)}(y_{N-2}, y_{N-1}, s, y_1, y_2)$; $\vec{y} = (y_{N-2}, y_{N-1}, y_1, y_2)$ and $d\vec{y} = dy_{N-2} dy_{N-1} dy_1 dy_2$. Equation (4.22) suffices for defining the mean field, f .

Evolution equations for $p_{(n)}$ ($n \geq 2$) can be written in a similar fashion, but lie beyond our scope.

4.3.3 Self-consistency equation for the mean field

In this subsection, we combine Eqs. (4.17) and (4.22) in order to extract a formula for the mean field, $f(s, t)$. Thus, we assume there exists an f such that [101]

$$\hat{P}(s, t) \equiv P(s, t) . \quad (4.23)$$

This equation expresses the hypothesis that the exact TWD, $P(s, t)$, coincides with the MF TWD. We choose $\hat{q} = \sqrt{6}$ since then subtracting Eq. (4.22) from Eq. (4.17) yields the formula

$$A(s, f(s, t)) P(s, t) = \int_{\mathbb{R}_4^+} \mathcal{A}(s, \vec{y}) p_{(5)}(s, \vec{y}, t) d\vec{y} . \quad (4.24)$$

This is the desired formula for $f(s, t)$. It simply states that in order to compute f one must in principle know the 5-terrace joint probability density. Equation (4.24) may be simplified via the 3-terrace probability density, $p_{(3)}$, by taking into account the particular form of A , Eq. (4.11):

$$\begin{aligned} A(s, f(s, t)) P(s, t) = & \\ & 2 \int_{\mathbb{R}_2^+} H(s; y_2, y_1) p_{(3)}(y_2, s, y_1, t) dy_1 dy_2 \\ & - \int_{\mathbb{R}_2^+} H(y_2; y_1, s) p_{(3)}(y_1, y_2, s, t) dy_1 dy_2 \\ & - \int_{\mathbb{R}_2^+} H(y_1; s, y_2) p_{(3)}(s, y_1, y_2, t) dy_1 dy_2 . \end{aligned} \quad (4.25)$$

In the remainder of this chapter, we apply a hypothesis of statistical independence for terraces (if $N \gg 1$), which simplifies Eq. (4.25) by reducing its right-hand side

to integrals involving the product $P(y_1)P(y_2)$.

4.4 Mean-field terrace-width distribution

In this section, we develop an approximation scheme in order to find the mean-field TWD. We focus primarily on the steady state, i.e., when $\partial_t P(s, t) \equiv 0$. At the end of this section, we discuss how our results are generalized to the time dependent TWD. Our primary task is to propose a *closure* for and then solve Eqs. (4.17) and (4.25) for the TWD P and mean field f . These equations must in principle be complemented with the entire BBGKY hierarchy. We avoid the complication of the kinetic hierarchy by applying approximations, which come from: (i) a decorrelation hypothesis for terraces, so that the $p_{(3)}$ in Eq. (4.25) is written as $p_{(3)}(y_2, s, y_1) \approx P(y_2)P(s)P(y_1)$, which automatically implies invariance of $p_{(3)}$ under permutations of its arguments (s , y_1 and y_2); and (ii) subsequent expansions of $f(s)$ and $P(s)$ in power series in the interaction strength g for $g \gg 1$. We compare our analytical results for the steady-state TWD with kMC simulations. Details of our 1D kMC algorithm are provided in [24].

4.4.1 Formulation of the asymptotics

We start with a remark on Eq. (4.25). If we naively set $p_{(3)}(s, y_1, y_2) = \delta(s - 1)\delta(y_1 - 1)\delta(y_2 - 1)$ and $P(s) = \delta(s - 1)$, Eq. (4.25) is satisfied trivially by $f = 1$. This property is reminiscent of the approach adopted within the linearized model in Ref. [43], where the mean field is the average terrace width (and thus coincides

with the initial width for a vicinal crystal). By contrast, in our nonlinear setting the approximation $f \approx 1$ can only be justified in the limit of strong enough step interactions ($g \gg 1$). In this case, deviations of the terrace widths from their average (and initial, deterministic) values become energetically unfavorable, and step fluctuations tend to be suppressed.

Based on these observations, we fix $g \gg 1$ and enforce a closure for Eqs. (4.24) and (4.25) via the *ansatz* $p_{(3)}(s, y_1, y_2) \approx P(s)P(y_1)P(y_2)$. For independent terraces moving in an “external potential” (i.e., loosely speaking, a force field *not* related to neighboring terraces), this expression becomes exact. In the presence of step interactions, this approximation is reasonable as will be shown by comparison to kMC simulations. Step correlations are *ipso facto* not included in our MF scheme. Accordingly, in our asymptotic calculations we assume that corrections to P and f resulting from terrace-terrace correlations are of order less than $O(g^{-1})$. In Sec. 4.5 we further discuss this assumption.

Accordingly, Eq. (4.25) becomes (with $\partial_t \equiv 0$)

$$A(s, f) \approx \int_{\mathbb{R}_2^+} \tilde{\mathcal{A}}(s, y_1, y_2) P(y_1)P(y_2) dy_1 dy_2, \quad (4.26)$$

where $\tilde{\mathcal{A}}(s, y_1, y_2) = A(y_2, y_1, s, y_1, y_2)$ (cf. Eq. (4.11)), and

$$A(s, f) = \left[\frac{4}{s+c} + \frac{2}{f(s)+c} \right] \left[\frac{1}{s^3} - \frac{1}{f(s)^3} \right],$$

$$\tilde{\mathcal{A}}(s, y_1, y_2) = \frac{4}{c+s} \left[\frac{1}{s^3} - \frac{1}{y_1^3} \right] - \frac{2}{c+y_1} \left[\frac{2}{y_1^3} - \frac{1}{y_2^3} - \frac{1}{s^3} \right].$$

Recall that $c = \check{c}/\langle w \rangle$ expresses the interplay of adatom diffusion and attachment-detachment (see Sec. 4.2.1). Here, by abusing notation, we set $f(s) = f(s, t \rightarrow \infty)$ assuming $f(s, t)$ settles to a steady state.

To enable analytical treatment, we apply the ansatz

$$f(s) = f_0 + g^{-\alpha} f_1(s) + o(g^{-\alpha}) , \quad \alpha > 0 , \quad (4.27)$$

where α is determined in Appendix A to be unity, and $f_0 = \mathcal{O}(1)$ is a *constant* independent of g in anticipation of a *uniform* mean field in the limit of strong interactions. Equation (4.27) is viewed as a formal expansion for $f(s)$ when g is large within our decorrelation ansatz. In the same vein, we expand the TWD as

$$P(s) = P_0(s; g) + g^{-\alpha} P_1(s; g) + o(g^{-\alpha}) . \quad (4.28)$$

In this expansion, we indicate that the P_k (where k denotes the expansion order) may depend on g . This distinction is made for later convenience, as the P_k bear a g -dependence of exponential type. We also invoke Eq. (4.17), with $\partial_t P(s, t) = 0$:

$$\frac{g}{3} \frac{d}{ds} [A(s, f) \hat{P}(s)] = \frac{d^2}{ds^2} \hat{P}(s) , \quad (4.29)$$

which will be used to determine $P(s)$.

Equations (4.26)-(4.29) now form a closed system of equations, which in principle may be solved for f and P .

4.4.2 Zeroth-order approximation and composite expression

In this subsection, we describe the underlying methodology used to solve the system of equations (4.26)-(4.29) up to some appropriate order in the interaction g .

We also give expressions for the mean field and TWD up to $\mathcal{O}(g^{-1})$. Details of the calculations are carried out in Appendix A.

We begin by noting that substitution of the expansions (4.27) and (4.28) into Eqs. (4.26) and (4.29) yields a cascade of equations for f and P . Furthermore, if the TWD is sharply peaked at, say, $s = \zeta \approx 1$ and decays rapidly to zero away from ζ , then Eq. (4.26) can be simplified via asymptotics [106]. The idea is to expand $\tilde{\mathcal{A}}(s, y_1, y_2)$ about $y_1 = y_2 = \zeta$. This reduces the consistency equation for f to an expression relating the mean field to the moments of the TWD. The asymptotic approximation of the right-hand side of Eq. (4.26) is motivated by the linearized model of Sec. 4.2.4, which indicates that the standard deviation of the TWD is $\mathcal{O}(g^{-1/2})$. This scaling with g of the standard deviation should also hold for the present case since the linear analysis is expected to capture the behavior of the TWD peak.

To leading-order in g , one finds that $f_0 = 1$. The zeroth-order TWD, $P_0(s)$, is given by,

$$P_0(s; g) = \mathcal{N}_0 \frac{s^{\frac{4g}{3c^3}}}{(s+c)^{\frac{4g}{3}(\frac{1}{c^3}+1)}} \times \exp \left[-\frac{2gs}{3(c+1)} + \frac{4g}{3c^2s} - \frac{g(3c+2)}{3c(c+1)s^2} \right], \quad (4.30)$$

where $\mathcal{N}_0(g, c)$ is a normalization constant (see Ref. [24]). A noteworthy feature of this P_0 , referred to by the term “zeroth-order” (ZO) in Fig. 4.2, is an essential singularity at $s = 0$, which forces P_0 and *all* its derivatives to *vanish* as $s \rightarrow 0^+$. This singularity is viewed as an artifact of the 1D character of the present model.

For large g , the leading-order variance σ_0^2 , associated with $P_0(s; g)$ is given by

(cf. Appendix A.2),

$$\sigma_0^2 = \frac{c+1}{6g} + o(g^{-1}). \quad (4.31)$$

This formula is consistent with the long-time limit of the variance for the linearized model; cf. Eq. (4.15) with $g_c = 3g/(c+1)$. One finds that the leading-order variance sets the value $\alpha = 1$.

The first-order correction, $f_1(s)$, to the mean field is found to be (Appendix A.1)

$$\begin{aligned} f_1(s) &= -\frac{c+1}{3} \\ &\times \left[\frac{12}{s+c} + \frac{6}{c+1} + \frac{6}{(c+1)^2} - \frac{1}{(c+1)^3 s^3} + \frac{1}{(c+1)^3} \right] \\ &\div \left[\frac{12}{s+c} + \frac{6}{c+1} - \frac{2}{(c+1)^2 s^3} + \frac{2}{(c+1)^2} \right]. \end{aligned} \quad (4.32)$$

We choose not to compute $P_1(s)$ explicitly. The form of the requisite $f_1(s)$ is already complicated, rendering further computations for P unwieldy. Instead, we resort to Eq. (4.29) with $f(s) \approx 1 + f_1(s)/g$. By direct integration we derive a formula for $P(s)$, called “composite expression” (CE) in Figs. 4.2–4.4, which is valid to $\mathcal{O}(g^{-1})$:

$$P(s) \approx \mathcal{N}(g, c) \exp \left[\frac{g}{3} \int_1^s A \left(z, 1 + \frac{f_1(z)}{g} \right) dz \right], \quad (4.33)$$

where $f_1(s)$ is given by Eq. (4.32) (via Eq. (4.26)), and $\mathcal{N}(g, c)$ is a normalization constant subject to $\int_0^\infty P(s) ds = 1$.

In Fig. 4.2 we plot our MF zeroth-order approximation and composite expression versus the analytical prediction of the linearized model of Sec. 4.2.4 and 1D kMC simulations for the TWD at sufficiently long times (practically, as $t \rightarrow \infty$); see Appendix B for details of the simulations. For large g , which causes fluctuations

to be small, the deviations of a given terrace width from the mean are small, and hence we expect the asymmetry of the TWD to be suppressed. The property that the TWD tends to become Gaussian can be seen for the case $g = 8400$. For this large value of g , the prediction of the linearized model is in good agreement with both the kMC and MF results.

As fluctuations increase (i.e. g becomes smaller), terraces significantly wider than the mean become favored over those significantly smaller than the mean, due to the singular step repulsion that prohibits neighboring steps from touching each other. Hence, as g becomes smaller, the TWD should become both wider and more asymmetric. The linearized model inherently fails to capture the asymmetry, which becomes important for decreasing step interaction strength, g . The zeroth-order MF approximation captures the asymmetry of the TWD. Without the first-order term f_1 , the mean of the ZO TWD is greater than unity. Of the three analytic predictions (LM, ZO, CE), the CE provides the best approximation to the kMC TWD, *even for moderate fluctuations, where the asymmetry of the step interaction becomes important.*

The correction $f_1(s)/g$ to the mean field f has a singularity in the interval $(0, 1/2)$ for s , as can be shown from Eq. (4.32) via algebraic inequalities. This singularity does not cause any pathology to the moments associated with P , and is viewed as a consequence of asymptotic approximations leading to Eq. (A.2). For $g \gg 1$, this singularity lies far away from the location of the TWD peak, and the MF correction $f_1(s)$ improves the accuracy for $P(s)$ by Eq. (4.33) (see Fig. 4.2).

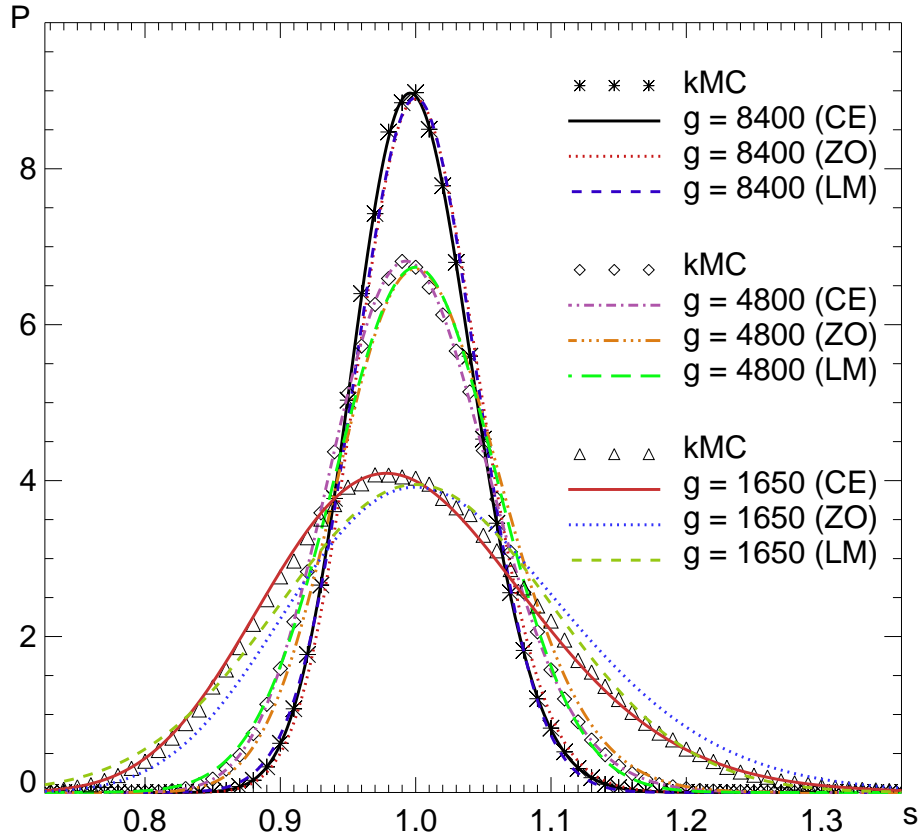


Figure 4.2: Steady-state TWD, $P(s)$, by: kMC simulations; and MF zeroth-order (ZO) approximation (4.30), MF composite expression (CE) (4.33), and linearized model (LM) for $g = 1650, 4800, 8400$ and $c = 100$. Note that the linearized model fails to capture the asymmetry of the kMC TWD, particularly for $g = 4800$ and $g = 1650$. The ZO approximation reproduces the asymmetry of the kMC TWD but not the correct location of the TWD maximum. The CE agrees best with the kMC TWD.

4.4.3 Time-dependent terrace-width distribution

Calculation of the time-dependent TWD does not differ significantly from the time independent case. Here we state the main ideas and results; a full treatment may be found in Ref. [24].

Our formulation relies on extending the main hypotheses of Sec. 4.4 (for the steady state) to the present, time-dependent setting under $g \gg 1$. So, we assume that for finite times the strong step interactions suppress terrace fluctuations, cause narrowing of the TWD, and favor terrace decorrelation. As before, we assume that $f = f(t)$ may be asymptotically expanded in inverse powers of g .

In order to determine the TWD, we first write it in the factorized form

$$P(s, t) = \check{P}(s, t) \psi(s, t) , \quad (4.34)$$

$$\check{P}(s, t) = \mathcal{N}(g, c) \exp \left[\frac{g}{3} \int_1^s A(z, f(z, t)) dz \right] , \quad (4.35)$$

where $\psi(s, t)$ is to be determined. Asymptotically expanding $\psi(s, t)$ in inverse powers of g leads to a cascade of equations for ψ and f , which can be determined perturbatively; see Ref. [24].

In terms of the rescaled variables

$$\xi = \sqrt{g}(s - 1) , \quad \tau = 3gt ,$$

one finds that to leading order

$$\begin{aligned} \psi(\xi, \tau) &= \left(\frac{6g}{c+1} \right)^{1/2} \check{P}(1, 0)^{-1} [2\pi \left(1 - e^{\frac{-12\tau}{c+1}} \right)]^{-1/2} \\ &\times \exp \left[- \frac{3\xi^2 e^{\frac{-12\tau}{c+1}}}{(c+1)(1 - e^{\frac{-12\tau}{c+1}})} \right] + \mathcal{O}(g^{-1}). \end{aligned} \quad (4.36)$$

A corresponding formula for the TWD follows from Eq. (4.34) with $f \approx f_0 = 1$.

The first-order correction f_1 to the time dependent mean field is given by

$$\begin{aligned}
 f_1 &= -2g\sigma_0(\tau)^2 \\
 &\times \left[\frac{12}{s+c} + \frac{6}{c+1} + \frac{6}{(c+1)^2} - \frac{1}{(c+1)^3 s^3} + \frac{1}{(c+1)^3} \right] \\
 &\div \left[\frac{12}{s+c} + \frac{6}{c+1} - \frac{2}{(c+1)^2 s^3} + \frac{2}{(c+1)^2} \right], \tag{4.37}
 \end{aligned}$$

which follows the steady-state case. Here, $s = 1 + g^{-1/2} \xi$, $t = (3g)^{-1} \tau$ and $\sigma_0^2(\tau)$ is the variance for the TWD $P(s, t)$ of Eq. (4.34) under $\psi \approx \psi_0$ and Eq. (4.35) with $f \approx f_0 = 1$. By the same method used to derive Eq. (4.31), we obtain

$$\sigma_0(\tau)^2 = \frac{c+1}{6g} \left(1 - e^{\frac{-12\tau}{c+1}} \right). \tag{4.38}$$

In the limit $t \rightarrow \infty$, this result agrees with both the MF steady-state variance, Eq. (4.31), and the variance from the linearized model, Eq. (4.15).

In Fig. 4.4.3, we plot the variance as a function of time using different approximation schemes, i.e., the linearized model (LM) and the MF scheme, and include results of kMC simulations (cf. Appendix B). We observe that the MF approximation for the variance approaches a finite limit (in steady state) at nearly the same time as the kMC simulation, with improved accuracy for larger g . In contrast, the linearized model fails to capture the correct asymptotic, long time behavior of the variance *for any* value of g . In Fig. 4.4, we show plots of the time-dependent TWD for some fixed, intermediate time t . We see that by increasing g , the validity of the CE is extended in time.

Qualitatively, the TWD evolves as follows: For sufficiently small times, the

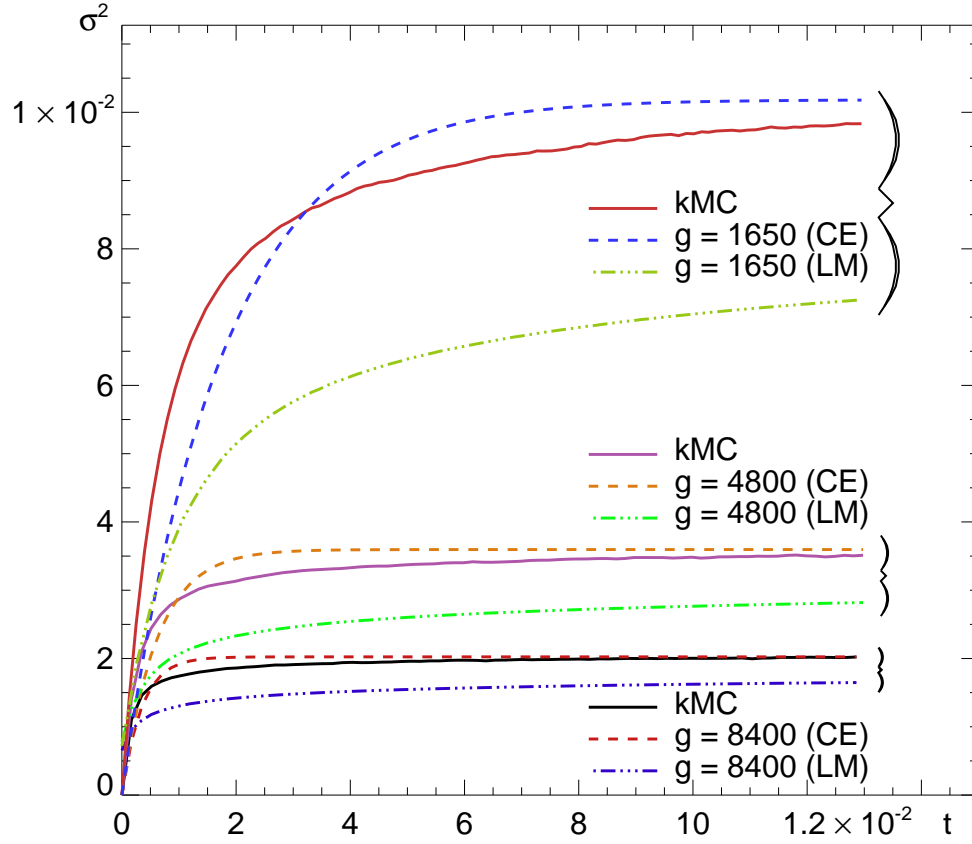


Figure 4.3: Variance of TWD as a function of dimensionless time by: kMC simulations; integration of MF composite expression (CE) (4.34) with Eq. (4.35) and $f = f_0 + f_1/g$, and Eq. (4.15) of linearized model (LM), for $g = 1650, 4800, 8400$ and $c = 100$. For stronger step interactions (lower part of figure), the TWD becomes narrower. The variance of the time-dependent CE agrees with the asymptotic, long-time limit of the kMC variance, while the variance of the linearized model does not.

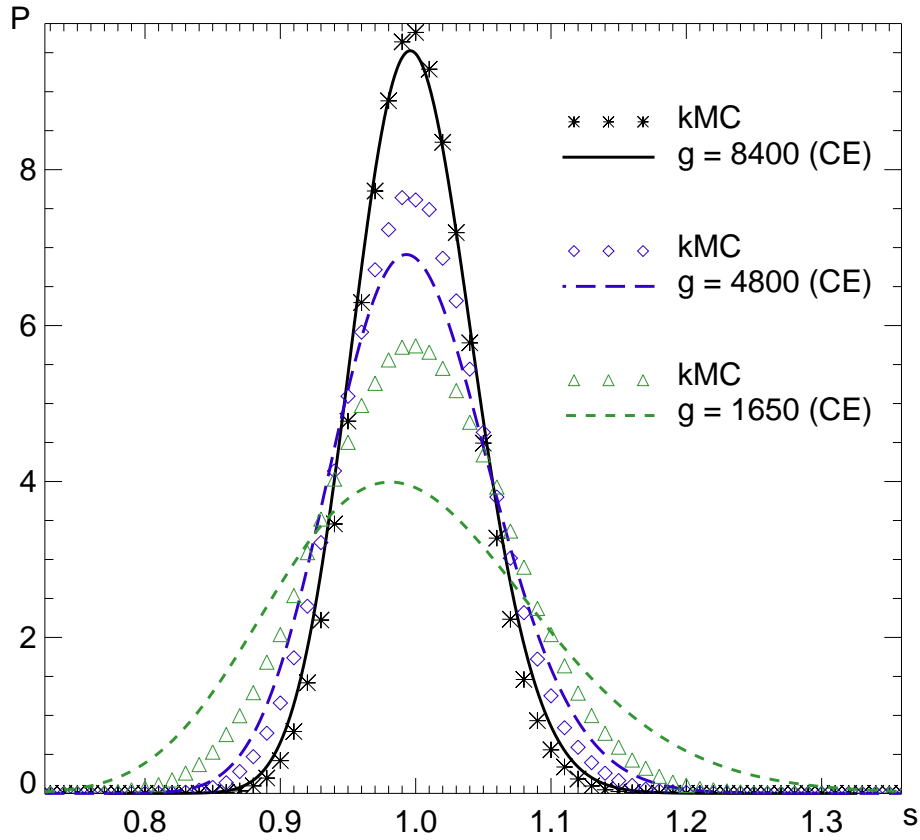


Figure 4.4: Time-dependent TWD as a function of terrace width variable, s , for fixed intermediate time t by: kMC simulations; and MF time-dependent composite expression (CE) by Eq. (4.34) with Eq. (4.35) and $f = f_0 + f_1/g$ for $g = 1650, 4800, 8400$ with $c = 100$. In kMC simulations, the TWD is computed after 2500 iterations of the algorithm. As g increases, the time-dependent CE reproduces the behavior of the kMC TWD more accurately for intermediate times.

TWD is approximately Gaussian, due to the delta-function initial condition, affected slightly by an asymmetric contribution from the steady state. As time increases, the asymmetry becomes more pronounced, and the Gaussian behavior gives way to the steady state, Eq. (4.30). Simultaneously, the correction f_1 to the average value $f_0 = 1$ grows larger, causing a consistent shift of the peak of the TWD to the left [see Eqs. (4.33) and (4.37)].

4.5 Discussion

4.5.1 Comparison of the mean-field and linearized models

Our main goal in this chapter is the development of analytical techniques for the approximate solution of stochastic equations for fluctuations of interacting steps on vicinal surfaces. To enable some analytical treatment of the governing equations, we restrict attention to 1D geometries. A crucial quantity used to describe such systems is the TWD, which we calculate for the case of force dipole and entropic step repulsion. In this context, we examine the relative merits of a linearized (LM) and mean field (MF) model.

A major aspect of our analysis is the addition of second-order, conservative white noise to the equations of terrace motion, Eq. (4.8). For the linearized model in particular, this choice of noise is determined partly by the symmetry conditions of the system. This noise is the least conservative noise for which the TWD variance approaches a finite limit in agreement with the MF model. We point out that the substitution of a higher-order conservative noise in the derivations leading to

Eq. (4.15) can yield a variance that converges to the same limit as Eq. (4.15), but at a faster (albeit, algebraic) rate. Hence, the *form* of the noise itself is not unique, and we choose the simplest possibility for comparison of the linearized and MF models.¹²

In the MF case, the mean field f is invoked to decouple the system of equations. To find the mean field, we make use of formal expansions in (negative) powers of the interaction strength, g , and apply a decorrelation ansatz for terraces. While we do not provide rigorous justification for this ansatz, its validity is justified in part by comparison of the MF TWD with the kMC and LM TWDs (Figs. 4.2–4.4).

Specifically, correlations are present in the linearized model since couplings are retained, while nonlinear effects (but no correlations) are accounted for in the MF model. Therefore, comparison between the two analytic models and kMC (which contains both effects) indicates the *relative importance of nonlinearities over correlations* for the system at hand. The agreement between the kMC and MF models suggests that nonlinear effects are more important than correlations when fluctuations increase (i.e. as g decreases).

The modification of the FPE for the TWD by terrace correlation effects is not considered here. To include correlations, one needs to update the 5-terrace joint probability density via the corresponding evolution equation of the BBGKY hierarchy and possible application of a partial decorrelation ansatz.

¹²Application of the fluctuation-dissipation theorem in order to determine the noise is based on the existence of an *a priori* connection between the mechanisms causing fluctuations and dissipating energy [107]. In our system, where the noise has been introduced ad hoc, no such connection is apparent. See, for example, the discussion on open systems in Ref. [108].

Our analysis shows in a *minimal (1D) setting* how the mean field f is influenced by *nonlinearities* stemming from the step interaction energy. Because of the interaction, the self-consistent mean field does *not* in principle coincide with the average terrace width. In fact, corrections for this f beyond the terrace width average are shown here to be important. In this vein, the use of a linearized model has shortcomings, which we detect via comparisons with kMC simulations. In particular, we find that as fluctuations increase (i.e. as the interaction strength, g , decreases), the linearized model fails to account for both the asymmetry of the TWD (induced by the step non-crossing condition) and the correct long-time asymptotic evolution of the system. Moreover, we find that our composite MF expression *does* account for asymmetries of the TWD over all times, but only for sufficiently large interaction strengths, g . This inadequacy of the MF approximation can be attributed to the influence of terrace-terrace correlations at finite times.¹³

4.5.2 Limitations and applications of our approach

Our model and analysis have limitations. A fundamental question is to what extent our 1D model can be connected to the 2D dynamics of actual surfaces, and hence what observable phenomena it can account for. One indication of the inadequacy of the 1D model to fully describe 2D step fluctuations is the appearance of a singularity of the TWD, $P(s, t)$, at zero terrace width ($s = 0$). Since this singularity is integrable (i.e. $P(s, t)$ decays faster than exponentially as $s \rightarrow 0$), it does not cause any problems in computing the moments of P . Furthermore, this

¹³For a discussion of whether or not correlations persist at long times, see Ref. [26].

behavior forces the TWD and all its space derivatives to vanish as the terrace width approaches zero. However, step meandering in 2D is expected to “regularize” the behavior of the TWD near $s = 0$.

Despite the above limitations, our analysis may be useful in understanding quantitative features of certain “quasi-1D” step systems similar to those in Refs. [8, 109]. The time dependent, composite TWD (4.34) expresses the interplay between mass transport and step interactions via the parameters $c = \mathcal{D}\langle w \rangle^{-1}/(\kappa_-^{-1} + \kappa_+^{-1})$ and g , respectively. Hence, for systems in which step-step interactions drive evolution [8], fitting experimental data with Eq. (4.33) should indicate the mass transport mechanism via the parameter c , and the interaction strength parameter, g . We find that our simulation corresponds to the case $c \geq 100$, and hence the kMC algorithm amounts to an attachment-detachment limited (ADL) system [8].

We expect that our analysis is also useful in understanding more general, qualitative features of 2D step systems. For example, the asymmetry of the TWD resulting from step interactions, as well as the narrowing of the TWD with the increase of the step interaction strength, g , should persist in 2D. Since narrowing and asymmetry appear in opposite limits of interaction strength, g , the relative asymmetry of TWD is an indication of the relative step repulsion; i.e. as step repulsion is increased, the TWD should approach a Gaussian distribution (see Fig. 4.2). Conversely, as g is decreased, the nonlinearity of the interaction should manifest as an asymmetry in the TWD. Since the non-crossing condition for steps implies asymmetry of the TWD, our analysis provides a quantitative description of how the non-crossing manifests probabilistically within the BCF framework. Our prediction

that the terrace width variance scales as $1/g$ should hold in a 2D setting.

4.5.3 Open questions

It should be stressed that modeling noise in 2D introduces subtle issues and more elaborate governing equations [40, 110]. Reconciling the BCF picture with noise in 2D is a largely unexplored area. In the same vein, an issue not addressed here is the possible dependence of the diffusion coefficient on the terrace width in 1D. This would require choosing between, e.g., Stratonovich and Itô stochastic calculus [100]. Our relatively simple model of noise circumvents this complication.

The starting step-flow model and approximation schemes are amenable to direct extensions in 1D. For example, the effect of material deposition can be included in the step motion laws. In this case, the increase of deposition flux causes narrowing of the TWD [43] and, hence, contributes qualitatively in a fashion similar to an increase in the step interaction strength, g . Further, a contribution to the noise terms stems from fluctuations in the number of deposited atoms [111]. The joint effect of deposition and dipolar step interactions is expected to result in an asymmetry of the TWD (in s), in contrast to the Gaussian TWD found via a linearized model in Refs. [43, 101]. Richer kinetics such as evaporation and step permeability [112] can be included in the formulation.

4.6 Summary

In this chapter, we formulated and analyzed a 1D stochastic model of interacting steps on a vicinal crystal. The starting point was the BCF theory, enriched with elastic-dipole step interactions and ad hoc conservative white noise. First, we linearized the governing equations of terrace motion and derived the TWD for the resulting, coupled system of SDEs. Second, by perturbation theory for strong step interactions, we considered the effect of nonlinearities by employing, within a terrace decorrelation hypothesis, a MF formalism that decouples the SDEs. In the case of the steady state, Eq. (4.30) describes the zeroth-order (ZO) approximation for the TWD, while Eq. (4.33) provides a more accurate composite expression (CE). Within the MF approximation, the time dependent TWD is described by Eqs. (4.34) and (4.35).

Through comparison with kMC simulations, our analysis indicates that, as fluctuations increase, linearized systems fail to capture asymmetries of the TWD induced by (nonlinear) step repulsion. In contrast, our MF analysis predicts a TWD that agrees with kMC simulation results over a wider range of step interaction strengths. We indicated how our model may be used to determine physical parameters of “quasi-1D systems” [8].

Part II

Phase-field model of block-copolymers

Chapter 5

Physics of block-copolymers: an unhappy marriage

In recent years, the popularity of block-copolymers (BCPs) has increased dramatically due to their potential industrial applications. In particular, BCPs self-assemble into microdomains that resemble patterns found on modern microprocessors [10–13, 44–47]. The goal of industrial applications is therefore to control the morphological properties of BCPs in order to use them as templates for microchip manufacturing (cf. Fig. 5.1) [13, 14].

The physics of BCP self-assembly can be understood by considering their molecular structure. On the microscale, BCPs are chains of repeated subunits called monomers; these chains have the structure AA...AA-BB...BB, where A and B are different monomers. In general, the monomers are molecules such as polystyrene (PS) or polymethyl methacrylate (PMMA). The subchains generally contain tens of monomers to thousands of monomers, depending on the application.

The two key properties that dictate the behavior of BCPs are: (i) the A and B subchains are connected at a single point; and (ii) the A and B monomers repel one another. As a consequence of this second property, the subchains tend remain as far apart from one another as possible. But like an unhappily married couple, they can only separate so much. In large systems of BCPs, this competition leads to a microphase separation into A-rich and B-rich domains with widths that depend

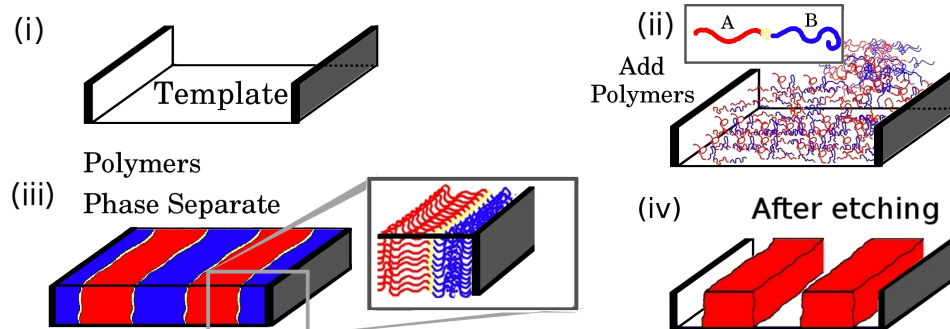


Figure 5.1: A simplified cartoon showing how template directed self assembly (TDSA) can be used to pattern semiconductor devices: (i) a template is etched into a substrate using conventional lithographic techniques; (ii) block-copolymers are added to the template; (iii) polymers self organize into microdomains; (iv) by removing one of the polymer components (B components in this image) one is left with a template that can be used to guide the formation of straight wires, for example. Note that the roughness of the A-B interfaces will in principle affect the roughness of the template after etching.

on the A and B subchain lengths; see Fig. 5.1.

In many applications, one is ultimately interested in etching away the B monomers (for example). This process leaves behind a template of A monomers that can guide the nanofabrication of other features (cf. Fig. 5.1). In such cases, one therefore wishes to control the shape of the A-B interface, since this will ultimately determine the morphology of the template after etching. In contrast to the previous chapters on vicinal crystals, however, there is no lattice or discrete grid that we can use to measure the position of a suitably defined interface. Moreover, in the region separating A-rich and B-rich domains, the A and B monomers intermix slightly due to the fact that the BCPs are able to diffuse and wrap around one another. Consequently, the interfacial region will have some finite width that can

depend on the strength of the A-B repulsion (i.e. stronger repulsions lead to less mixing between microdomains).

This observation therefore motivates a phase-field approach to modeling interfaces. The key idea of such an approach is to represent the system in terms of the relative density of A and B monomers. In the regions separating A-rich and B-rich domains, this density should go through a sharp transition or boundary layer. Our approach is to define the interface in terms of this boundary layer and subsequently use the phase-field model to study the interface morphology. In the following sections, we make these ideas more precise.

5.1 Leibler-Ohta-Kawasaki phase-field model

The theory of phase-field models for BCPs has been well developed over the past thirty years. As numerous works exist on the derivations of such models, we only summarize the key points that are relevant for an understanding of our work; cf. also Refs. [17, 18, 115]. The key goal of these approaches, however, is to formulate a coarse-grained model of the energy of the system, from which the statistical properties of the melt can be derived.

5.1.1 Microscopic Gaussian-chain model

As the previous section suggested, BCP melts are complicated systems. In principle, a full treatment requires that one model interactions between many large and often complex monomers. For context, PMMA ($C_5O_2H_8$), a molecule often used

as one of the monomer species, has 17 atoms total. Given that a single subchain may contain as many as 10^3 monomers, and a BCP melt may easily have 10^{12} polymers, an atomistic treatment of such a system would need to account for as many as 10^{16} particles total! Many simplifications are thus introduced at the microscopic scale in order to render the analysis more tractable.

The first such simplification is to replace each polymer with a continuous curve $\mathbf{r}(\tau)$, where τ is some variable that parameterizes the arc length and $\mathbf{r}(\tau)$ is confined in some domain \mathcal{D} . The domains $0 \leq \tau < \hat{f}$ and $\hat{f} < \tau \leq \mathcal{N}$ correspond to the A and B subchains of the polymer, where \mathcal{N} is index of parameterization (effectively the length of the chain or total number of monomers). Any curve \mathbf{r} is an allowed shape for the polymer provided that it is continuous (derivatives of \mathbf{r} need not be continuous). This view of polymers is often called a Gaussian-chain model.

The energy of a Gaussian-chain system is typically written in the form

$$H\{\mathbf{r}_i\} = \frac{1}{2} \sum_{i=1}^n \int_0^{\mathcal{N}} d\tau \left(\frac{d\mathbf{r}_i(\tau)}{d\tau} \right)^2 + \mathfrak{V}\{\mathbf{r}_i\}, \quad (5.1)$$

where \mathbf{r}_i is the position vector of the monomer parameterized by τ in the i th chain, n is the total number of polymers, and H and \mathfrak{V} are functionals of the set of \mathbf{r}_i .¹

¹This energy assumes that the length between adjacent monomers is the same for both the A and B species; see [18].

The potential \mathfrak{V} characterizes the repulsion between monomers and has the form

$$\begin{aligned}
\mathfrak{V}\{\mathbf{r}_i\} = & E_{AA} \sum_{i=1}^n \sum_{j=1}^n \int_0^{\hat{f}} d\tau \int_0^{\hat{f}} d\tau' \delta(\mathbf{r}_i(\tau) - \mathbf{r}_j(\tau')) \\
& + E_{BB} \sum_{i=1}^n \sum_{j=1}^n \int_{\hat{f}}^{\mathcal{N}} d\tau \int_{\hat{f}}^{\mathcal{N}} d\tau' \delta(\mathbf{r}_i(\tau) - \mathbf{r}_j(\tau')) \\
& + E_{AB} \sum_{i=1}^n \sum_{j=1}^n \int_0^{\hat{f}} d\tau \int_{\hat{f}}^{\mathcal{N}} d\tau' \delta(\mathbf{r}_i(\tau) - \mathbf{r}_j(\tau')), \tag{5.2}
\end{aligned}$$

where $\delta(\mathbf{r})$ is the Dirac delta function and E_{AA} , E_{BB} , and E_{AB} are the interaction energies associated with AA, BB, and AB crossings. In order for phase microphase separation to occur, we require that $E_{AB} > E_{AA} + E_{BB}$ (i.e. A-B interactions must be disfavored over A-A and B-B interactions; cf. Eq. (5.8)).

In principle, all of the statistical information about the system can be gleaned from Eq. (5.1). The difficulty, however, lies in computing expectation values over the sets $\{\mathbf{r}_i\}$. Consequently, we are motivated to consider a coarse-grained version of Eq. (5.1) in which the system is characterized by the local density of monomers and not the polymer positions.

5.1.2 Coarse-graining the Gaussian-chain model

In their original work [18], Ohta and Kawasaki defined the densities

$$\rho_A(\mathbf{r}) = \sum_{i=1}^n \int_0^{\hat{f}} d\tau \delta(\mathbf{r} - \mathbf{r}_i(\tau)), \tag{5.3}$$

$$\rho_B(\mathbf{r}) = \sum_{i=1}^n \int_{\hat{f}}^{\mathcal{N}} d\tau \delta(\mathbf{r} - \mathbf{r}_i(\tau)), \tag{5.4}$$

$$\phi(\mathbf{r}) = \rho_A(\mathbf{r}) - \rho_0 \hat{f} / N = -\rho_B + \rho_0 (N - \hat{f}) / N, \tag{5.5}$$

where ρ_A and ρ_B are the densities of A and B monomers and $\rho_0 = \rho_A + \rho_B$ is assumed to be constant. The density ϕ is interpreted as the relative density of A versus B monomers. When $\hat{f} = \mathcal{N}/2$ (i.e. when the two subchains have the same length), ϕ takes the especially convenient form

$$\phi = \rho_A - \rho_B. \quad (5.6)$$

Using these definitions, Ohta and Kawasaki recast Eq. (5.1) into a functional of the density ϕ . Here I discuss only the main ideas behind their derivation. For a formal, physics-based approach, see Ref. [18]; for a mathematically rigorous derivation of their functional, see Ref. [115].

The main idea of LOK's approach was to model the polymer-polymer interactions in terms of a monomer density interacting with a background potential, which must be determined self-consistently.² They proceeded by first realizing that the potential \mathfrak{V} in Eq. (5.1) can be written in the form

$$\mathfrak{V}\{\mathbf{r}_i\} = -\chi \int_{\mathcal{D}} d\mathbf{r} \phi(\mathbf{r})^2 + C, \quad (5.7)$$

where C is a constant and

$$\chi = E_{AB} - E_{AA} - E_{BB} \quad (5.8)$$

is the Flory-Huggins parameter, a positive constant that characterizes the strength of the repulsion between A and B monomers. In passing, we note that experimentally, $\chi = \mathcal{O}(1)$ is considered to be a large value of the Flory-Huggins parameter [15, 116–118].³

²In these regards, the mean-field approach of Chapter 4 resembles that of LOK.

³This fact will become extremely important in Chapter 6 when we discuss line-edge roughness

Next, they wrote the partition function in the form $Z = \sum_{\{\mathbf{r}_i\}} \exp[-H\{\mathbf{r}_i\}]$.

Using the closure relation (where $D[\phi]$ is a functional measure over ϕ)

$$1 = \int D[\phi] \prod_{\mathbf{r}} \delta \left(\phi(\mathbf{r}) + \hat{f}\rho_0/\mathcal{N} - \sum_{i=1}^n \int_0^{\hat{f}} d\tau \delta(\mathbf{r} - \mathbf{r}_i(\tau)) \right), \quad (5.9)$$

they recast the partition function in the form

$$Z = \int D[\phi] e^{-\mathcal{H}[\phi]}. \quad (5.10)$$

LOK approximated the functional \mathcal{H} to be [18]

$$\frac{\mathcal{H}[\phi]}{k_B T} = \frac{\chi}{\mathcal{V}} \int_{\mathcal{V}} dV \left\{ \frac{\xi^2}{2} (\nabla\phi)^2 - \frac{\phi^2}{2} + \frac{\phi^4}{4} + \frac{\varsigma}{2} \int_{\mathcal{D}} dV' \phi(\mathbf{r}) g(\mathbf{r}, \mathbf{r}') \phi(\mathbf{r}') \right\}, \quad (5.11)$$

$$\xi^2 = \frac{a^2}{3\hat{f}(1-\hat{f})\chi} \quad \varsigma = \frac{36}{\hat{f}^2(1-\hat{f})^2 a^2 \chi \mathcal{N}^2}, \quad (5.12)$$

where \mathcal{V} is a unit volume, the Kuhn length a measures the average distance between two adjacent monomers,⁴ $g(\mathbf{r}, \mathbf{r}')\phi(\mathbf{r}')$ is the Green's function of the Laplacian, and the \mathbf{r}_i are again treated as continuous curves. (We specify boundary conditions for g in the next chapter.)

Importantly, this theory is based on several simplifying assumptions. First, the Gaussian chain model does not account for differences between the A and B monomers except through the interaction energies E_{AA} , E_{BB} , and E_{AB} . Second, the approximations leading to Eq. (5.11) are based on the assumption that ϕ is close to its mean value of 0. In principle, this suggests that the LOK Hamiltonian should only be valid when χ is suitably small, i.e. when A-B crossings are only slightly

in the context of manufacturing specifications set forth by the International Technology Roadmap for Semiconductors.

⁴This length is considered to be extremely small relative to the system size.

disfavored over A-A and B-B crossings. Nonetheless, several works have suggested that the LOK theory is still useful for studying line-edge roughness, and we take it as a suitable starting point for our analysis of melts that are of interest to industry.

5.2 Defining microdomain interfaces via the phase-field model

Equation (5.11) is the main result of Leibler, Ohta, and Kawasaki [17, 18]. By approximately minimizing Eq. (5.11) for an infinite system, LOK were able to predict the morphology of a bulk BCP melt as functions of \hat{f} and $\chi\mathcal{N}$. For a given unit length $0 \leq x \leq 2\ell$, they found

$$\phi_0(x, y, z) = -1 + \tanh \left[\frac{x - (1/2)\ell}{\sqrt{2}\xi} \right] - \tanh \left[\frac{x - (3/2)\ell}{\sqrt{2}\xi} \right], \quad (5.13)$$

where $\ell = (16\sqrt{2}/3\xi)^{1/3}(R_g)^{4/3}$ is the width of a microdomain for a copolymer whose volume fraction $\hat{f} = 1/2$; see Fig. 5.2. Here $R_g = \sqrt{\mathcal{N}/2}$ is the radius of gyration, the average end-to-end length of the BCPs [18]. Periodically extending this solution gives ϕ_0 for \mathbb{R}^3 (all space).⁵

Equation (5.13) has two boundary layers whose zeros are located at $\ell/2$ and $3\ell/2$. *We identify these zeros as the location of the microdomain interfaces.* The microdomain interface width (i.e. the boundary layer width) is $2\sqrt{2}\xi \ll \ell$. These

⁵More accurately, $\phi_0 = \sum_{j=1}^2 \Theta[x - \ell(j-1)] \Theta[j\ell - x] (-1)^{j-1} \tanh \left[\frac{x - (j-1/2)\ell}{\sqrt{2}\xi} \right]$ in Ref. [18], where $\Theta(x)$ is the Heaviside step function; the forms we give above are equal to within exponentially small corrections (when $\xi \ll \ell$) and are notationally more convenient. By “exponentially small corrections,” we mean the error in an expression is smaller than the next largest term by at least a factor of $\mathcal{O}(e^{-\ell/\xi})$. For perspective, a 10 nm microdomain width with $\xi = 1$ nm would yield corrections to ϕ_0 that are at most about $e^{-10} \approx 5 \times 10^{-5}$.

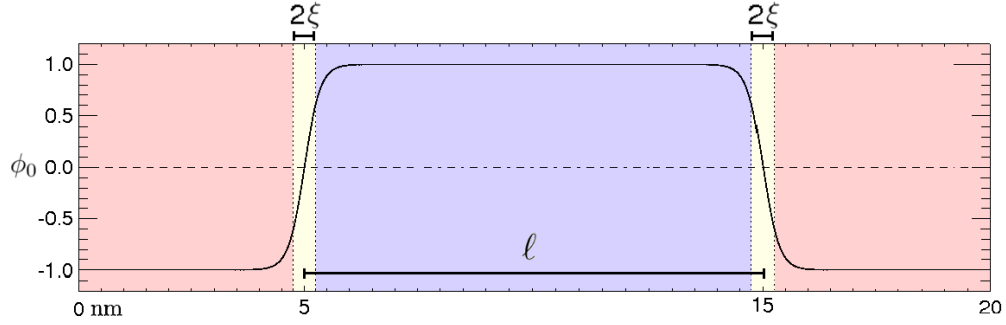


Figure 5.2: The mean field density $\phi_0(x)$ [cf. Eq. (5.13)] for lamellar microdomains with a 10 nm half-pitch and an interface thickness $\xi = 0.25$ nm. Regions where $\phi_0 \approx +1, -1$ correspond to A-rich and B-rich microdomains, respectively. The *boundary layer* (yellow) separating A and B-rich domains has a width characterized by $\xi \ll \ell$.

definitions are motivated by experimental measurements of BCPs, which can only determine a region within which to find the interface; see for example, Fig. 1.1 and Ref. [15]. In the next chapter, we will use this phase-field approach of modeling interfaces in order to characterize fluctuations in interface positions.

Chapter 6

Line-edge roughness of block-copolymer microdomain interfaces

A critical task in assessing the usefulness of block-copolymers is to characterize the fundamental limitations on the roughness of the patterns that they form. If the roughness cannot be controlled to within specification, devices fabricated using template-directed self-assembly (TDSA) will have soft defects, sufficient to preclude the use of block copolymers in many semiconductor manufacturing settings.

Our goal in this chapter is to *analytically* predict the line edge roughness (LER) of block copolymer microdomain interfaces (cf. Fig. 5.1) as a function of the Flory-Huggins parameter χ and the index of polymerization \mathcal{N} . Here we consider a graphoepitaxial system, i.e. one in which a solid template orders the microdomains (cf. Fig. 5.1); in the present analysis, we focus on lamellar systems in the strong segregation regime (SSR). Similar tasks have been pursued by, e.g. Semenov [119], Detcheverry and de Pablo, [120–122] and Bosse [113, 114], among others [28]; however, to the best of our knowledge, these treatments either (i) relied heavily on numerical methods and computer simulations (which we do not use here), or (ii) considered geometries and physical parameters corresponding to systems in a weak segregation regime (in which BCPs do not separate into well-defined microdomains). In the context of these studies, our work is therefore motivated by two main considerations.

First, melts in the SSR are the polymer systems most relevant to a semiconductor manufacturing process. In the SSR, different types of monomers mix poorly; microdomain boundaries are therefore sharp and well defined, which allows the microdomains to be effectively used as a template for features on microprocessors (for example). On the other hand, polymers in the weak segregation regime exhibit significant mixing of their different monomer components, so that the geometry of microdomains becomes difficult to resolve. Second, while simulations are an invaluable tool for exploring the behavior of many complicated polymer systems, there is significant computational overhead associated with exploring the parameter space available for industrial applications. While analytic models and results do not always provide the same level of detail as simulations, they nonetheless yield insight into the physical processes affecting a system over a broad range system parameters without the computational expense associated with numerical methods. Our work therefore (i) aims to complement simulations with formulas that predict the values of χ and \mathcal{N} needed to bring the LER within acceptable levels (ii) for systems that are of direct interest to the semiconductor industry.

The rest of the chapter is organized as follows. In Sec. 6.1 we give the main ideas of this chapter. In Sec. 6.2 we define the elements and key length scales of our system, review the basic principles of the LOK model, and derive the energy functional \mathcal{H}_1 describing fluctuations. In Sec. 6.3 we use perturbation theory to approximately diagonalize the energy functional \mathcal{H}_1 and identify the fluctuation modes responsible for LER and SAV. In Sec. 6.4 we define and calculate the LER and SAV. In Sec. 6.5 we discuss the physics of LER (Sec. 6.5.1), compare our results to

experiments (Sec. 6.5.2) and other models (Sec. 6.5.3), and consider our main results in the context of the LER requirements set forth by the International Technology Roadmap for Semiconductors (ITRS) (Sec. 6.5.4). In Sec. 6.6, we briefly summarize our work.

6.1 Main ideas

6.1.1 Background

The starting point of our analysis will be the LOK phase-field model of the previous chapter [17, 18], which gives the energy $\mathcal{H}[\phi]$ of a polymer melt as a functional of the relative density ϕ of the monomer species. In their original work, Ohta and Kawasaki determined that the lowest energy configuration (for equal molecular weights of the two monomer components) was indeed a lamellar phase-separated system, but with zero LER [18]. Our main tasks will be to (i) determine the fluctuation eigenmodes of the system about that ground state configuration, and then (ii) construct the total LER as a weighted sum of the roughness associated with each mode; the weighting function $P[\phi]$ is given by the Boltzmann distribution,¹

$$P[\phi] \propto e^{-\mathcal{H}[\phi]/k_B T}, \quad (6.1)$$

where k_B is the Boltzmann constant and T is the temperature. Interestingly, we will show that our analysis also provides estimates for the *sidewall angle variation* (SAV),

¹The Boltzmann distribution is sometimes referred to as the Gibbs distribution or Gibbs measure. The key idea, however, is that the statistics of our system will be given by an appropriate Canonical Ensemble.

another quantity that must be minimized in order to control feature width variation across a semiconductor wafer; see Sec. 6.4 for more discussion on the definition and importance of the SAV.

We note that while the LOK model is amenable to analytic computation, it is nonetheless complicated enough that we do not find exact expressions for the LER; rather, we arrive at our final results through a series of asymptotic approximations that become increasingly accurate as the product $\chi\mathcal{N}$ increases, i.e. when the system moves further into the SSR. As a secondary benefit of this approach, the approximations we invoke will reveal the dominant physical processes that contribute to (or rather, *limit*) the LER. When possible, we will estimate the error of our approximations in terms of physical parameters describing the system.

A salient feature of the LOK model is that it describes a system of string-like molecules (polymers composed of monomers) that *interact with each other* in terms of a macroscopic monomer density that *only interacts with a background potential* [115]. The connection between the A and B subchains contributes a non-local term (which resembles an electrostatic potential) to the energy functional. As we will show, this non-local term plays an important role in limiting low frequency LER modes; the low frequency behavior of our results will be one of the main features distinguishing them from simpler, capillary wave type models [119,123].

6.1.2 Notation and terminology

- Unless otherwise noted, italicized variables will represent quantities having dimensions, whereas non-italicized versions of the same variables will be dimensionless. For example, if x represents a length in some units (e.g. nm), the variable x will be a rescaled, dimensionless version of x . *The scaling of non-italicized variables will always be defined at their first appearance.*
- The term *pitch* (which is commonly used in lithography) refers to the average period of the polymer domain spacings; see Fig. 6.1, for example.
- By abusing notation slightly (cf. Chap 5), we use ϕ to represent the normalized relative density of A and B monomers. That is, we impose $0 \leq \phi_A(\mathbf{x}), \phi_B(\mathbf{x}) \leq 1$, so that $-1 \leq \phi \leq 1$. We furthermore impose the incompressibility condition $\phi_A(\mathbf{x}) + \phi_B(\mathbf{x}) = 1$.
- We also use \hat{f} ($0 \leq \hat{f} \leq 1$) to represent the normalized relative length of the A and B subchains. In other words, $\hat{f} = 1/2$ (as opposed to $\hat{f} = \mathcal{N}/2$) corresponds to A and B chains that are equal in length.

6.2 Perspective: system geometry and model of fluctuations

The system we wish to describe is a lamellar, diblock copolymer melt in the SSR (cf. Fig. 6.1). For simplicity, we take the molecular weights of the A and B subchains to be equal (i.e. $\hat{f} = 1/2$) and denote ℓ as the average width of A (or B) domains, i.e. ℓ is the so called half-pitch. We consider lamellae that have aligned

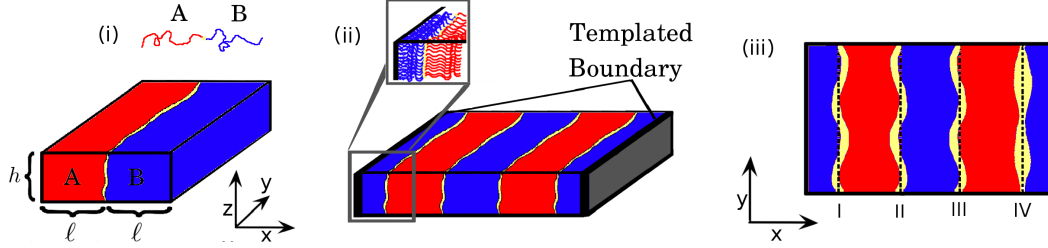


Figure 6.1: Three views of a polymer melt in the lamellar phase. Inset (i) shows a single block copolymer with A (red) and B (blue) components above two microdomains comprising a full pitch; a boundary (yellow) separates regions of different monomer species. We assume that the microdomains extend to $\pm\infty$ in the y direction. Inset (ii) shows a system with two full pitches. Boundaries are located at half-integer values of ℓ . The closeup (gray box) illustrates how the polymers organize within the microdomains. Inset (iii) shows a top down view of a system with different types of fluctuating boundaries. The black dotted lines indicate the average positions of the microdomain boundaries. Boundaries I - III exhibit LER fluctuations corresponding to f_1 [cf. Eq. (6.9)]; boundaries I and II are out of phase, whereas II and III are in phase. Boundary IV exhibits SAV fluctuations, corresponding to f_2 [Eq. (6.10)].

themselves with parallel, template walls separated by integer multiples of the width ℓ (cf. Fig. 6.1).² The parameter h denotes the height of the melt, and we assume that the system is infinite in the y direction.³ Since the system is in the SSR, the boundaries (yellow regions in Fig. 6.1) between the A and B domains are small compared to ℓ .

²Our present analysis will be concerned with grapho-epitaxial systems, whose ordering is induced by physical template walls. In principle one could modify our starting point to account for the effects of chemo-epitaxial patterning; this modification could be achieved by adding a suitable surface integral to Eq. (5.11); see Ref. [30].

³By converting the appropriate integrals to sums, our analysis is trivially generalized to systems that are finite in the y direction. In Sec. 6.3 we indicate where these changes should be made.

We describe this system with the Leibler-Ohta-Kawasaki energy functional. In specializing their Hamiltonian to our system, we impose periodic boundary conditions on ϕ and g in the y and z directions, which amounts to the assumption that we study the bulk behavior of the system in these two dimensions. At the left and right x boundaries, we set $\phi = \pm 1$. More specifically ϕ has the same sign at both boundaries if the number of microdomains is odd, but opposite signs for an even number of microdomains; the physics is otherwise insensitive to the signs we choose, provided that the above rules are followed. Physically, these boundary conditions mean that only one monomer species will be present at any given domain wall. Experimentally this condition can be realized by making the length of the system in the x direction to be an integer value of ℓ .⁴

We also assume that the normal derivative of g vanishes at the x boundaries, i.e. we impose Neumann boundary conditions on the Green's function. Physically, this choice is motivated by the observation that fluctuations at the domain boundary will have a higher energy penalty than those in the interior of the melt; at the domain wall, there are few polymers available to relieve strain caused by a fluctuation. With this in mind, we note that the Neumann condition describes the physics of the system more appropriately than a Dirichlet condition, for which $g = 0$ at the boundary.

⁴In actuality, ordered microdomains will still self-organize even if this condition is not strictly satisfied. However, this fact does not significantly affect the analysis that follows, since we will show that the spacing of the boundary only affects the LER to first order in perturbation theory; see Secs. 6.3 and 6.5.1.1.

We assume that the minimizer of Eq. (5.11) can be written in the form

$$\begin{aligned}\phi_0 &= \sum_{j=1}^N (-1)^j \tanh \left[\frac{x - (j - 1/2)\ell}{\sqrt{2}\xi} \right], & N \text{ odd} \\ \phi_0 &= -1 - \sum_{j=1}^N (-1)^j \tanh \left[\frac{x - (j - 1/2)\ell}{\sqrt{2}\xi} \right] & N \text{ even}\end{aligned}\quad (6.2)$$

where N (not to be confused with \mathcal{N} , the index of polymerization) is the number of interfaces. This solution simply extends the result of LOK to a system that is finite in the x direction.⁵

If ψ is some perturbation of the mean field density, then we write $\phi = \phi_0 + \psi$ and expand Eq. (5.11) to second order in ψ ; doing so yields,

$$\mathcal{H}[\phi] \approx \mathcal{H}[\phi_0] + \mathcal{H}_1[\psi] + \mathcal{O}(\psi^3) \quad (6.3)$$

$$\frac{\mathcal{H}_1[\psi]}{k_B T} = \frac{\chi}{\mathcal{V}} \int_{\mathcal{V}} dV \left\{ \frac{\xi^2}{2} (\nabla \psi)^2 - \frac{\psi^2}{2} + \frac{3}{2} \phi_0^2 \psi^2 + \frac{\varsigma}{2} \int_{\mathcal{D}} dV' \psi(\mathbf{r}) g(\mathbf{r}, \mathbf{r}') \psi(\mathbf{r}') \right\}, \quad (6.4)$$

where \mathcal{H}_1 is the approximate energy of a fluctuation ψ . We require that ψ satisfy periodic boundary conditions in the y and z directions; on the x boundaries, we set $\psi = 0$. Since fluctuations with large energies should occur rarely [via Eq. (6.1)], the above approximation is justified for small enough temperatures by noting that the statistics of the system will be dominated by those states whose energies are near that of the ground state; in essence, we treat $|\psi|$ as a small parameter that allows for the expansion given by Eq.(6.4).

In general, a given state ψ of the system can be represented as a linear combination of fluctuation modes ψ_j having energy E_j (with j simply indexing the modes).

⁵Technically speaking, Eq. (6.2) only minimizes (up to exponentially small corrections) the local part of Eq. (5.11). However, the variational approach of LOK determines the (approximate) value of ℓ that minimizes Eq. (5.11) when Eq. (6.2) is taken as a trial function of ℓ [18].

In principle, however, two arbitrary fluctuation modes ψ_j and $\psi_{j'}$ will almost always be correlated, so that the amplitude of the ψ_j expressed by the system will depend on the amplitude of $\psi_{j'}$. Hence our main task is to diagonalize Eq. (6.4) in terms of its eigenmodes, which vary independently from one another (i.e. are uncorrelated). We can then define the LER as a linear combination of the LERs associated with each of the relevant eigenmodes.

In anticipation of this task, we examine Eq. (6.4) to gain insight into the types of fluctuations allowed by our model, especially since we are looking for fluctuations of *boundary layers*. The term $\xi^2(\nabla\psi)^2$ yields a (small) energy penalty for non-constant fluctuations, while the non-local term multiplying ς promotes oscillations. The pair of terms $(1/2)(3\phi_0^2 - 1)\psi^2$ yields an energy penalty for non-zero fluctuations *except* in the boundary layers [i.e. when $|x - (n - 1/2)\ell| \leq \mathcal{O}(\xi)$], where these terms promote fluctuations. This last observation foreshadows the existence of eigenmodes localized within the microdomain interfaces, which are responsible for LER and SAV.

6.3 Characterizing interface fluctuations

In this section, our goal is to diagonalize Eq. (6.4) and find the eigenmodes corresponding specifically to interface fluctuations. We begin by non-dimensionalizing space via $dV \rightarrow d\tilde{V} = dV/\xi^3$ and $\tilde{\mathbf{r}} = \mathbf{r}/\xi$. Equation (6.4) then becomes

$$\frac{\mathcal{H}_1[\psi]}{k_B T} = \frac{\chi\xi^3}{\mathcal{V}} \int_{\mathcal{V}} d\tilde{V} \left\{ \frac{1}{2}(\tilde{\nabla}\psi)^2 - \frac{\psi^2}{2} + \frac{3}{2}\phi_0^2\psi^2 + \frac{\xi^2\varsigma}{2} \int_{\mathcal{D}} d\tilde{V}' \psi(\tilde{\mathbf{r}})\tilde{g}(\tilde{\mathbf{r}}, \tilde{\mathbf{r}}')\psi(\tilde{\mathbf{r}}') \right\}, \quad (6.5)$$

where $\tilde{g}(\tilde{\mathbf{r}}, \tilde{\mathbf{r}}')$ is the rescaled, dimensionless Green's function [note that $g(\mathbf{r}, \mathbf{r}')$ has units of inverse length]. If ς is sufficiently small, then to leading order we may diagonalize Eq. (6.5) by solving the eigenvalue problem,

$$-\tilde{\nabla}^2\psi - [1 + 3\phi_0^2]\psi = E^{(0)}\psi, \quad (6.6)$$

where $E^{(0)}$ is a dimensionless, leading-order energy eigenvalue. We may then use standard perturbation techniques to calculate corrections to $E^{(0)}$ and ψ . At the end of our analysis, we will determine the values of ς for which our perturbation theory is valid.

For a system having a single interface, Eq. (6.6) can be solved (up to exponentially small corrections⁵) if we cast it into the standard form,⁶

$$\psi(x, y, z) = \sum_{k_z} \int \frac{dk_y}{2\pi} f(x, k_y, k_z) e^{ik_y y + ik_z z} \quad (6.7)$$

$$0 = \partial_{xx}f + \lambda^2 f + l(l-1) \operatorname{sech}^2(x)f, \quad (6.8)$$

where $\lambda^2 = 2E^{(0)} - 2q_{\parallel}^2 - 4$ and $q_{\parallel}^2 = k_y^2 + k_z^2$ is a wave-vector parallel to the mean field interface profile. The constant l (not to be confused with ℓ) is an integer;⁷ for the model here, $l = 3$, which is determined in the steps leading from Eq. (6.6) to Eq. (6.8). The above expressions are written in terms of the rescaled variables

⁵Note that we have shifted the center of the domain to $x = 0$, so that $-\ell/2 \leq x \leq \ell/2$.

⁷We write Eq. (6.8) in terms of arbitrary l to emphasize a deeper connection between our model and that of Semenov [119]. In the latter, an effective Hamiltonian significantly different from Eq. (5.11) leads to an equation describing interface fluctuations that has the form of Eq. (6.8) with $l = 2$. As we will show later, the value of l plays a significant role in determining the type and number of interface fluctuations that our model can describe. In the present section we also discuss an important connection with quantum mechanics.

$x = x/(\sqrt{2}\xi)$, $y = y/\xi$, and $z = z/\xi$. The wave-vector k_y is a continuous parameter (in units of ξ^{-1}), whereas $k_z = 2\pi n\xi/h$, $n = 0, \pm 1, \pm 2, \dots$ may only take discrete values.⁸

Equation (6.8) is in fact the well-studied Pöschl-Teller equation used to model diatomic molecules in quantum mechanics [124]; exact solutions for any l can be expressed in terms of hypergeometric functions [124]. When l takes a simple integer value, these solutions reduce to products and sums of hyperbolic and trigonometric functions. For $l = 3$, there are two “bound” state solutions (one even and one odd), which approach zero away from the interface [for $|x| > \mathcal{O}(\xi)$], and a continuous spectrum of “scattering” states that asymptote to trigonometric functions away from an interface [125]. Specifically,

$$f_1(x) = \operatorname{sech}^2(x),$$

$$E^{(0)} = q_{\parallel}^2, \tag{6.9}$$

$$f_2(x) = \operatorname{sech}(x) \tanh(x),$$

$$E^{(0)} = q_{\parallel}^2 + 3/2, \tag{6.10}$$

$$f_e(x) = \frac{1}{1+\lambda^2} \{ [1+\lambda^2 - 3 \tanh^2(x)] \cos(\lambda x) - 3\lambda \tanh(x) \sin(\lambda x) \}$$

$$E^{(0)} = q_{\parallel}^2 + 2 + \lambda^2/2, \tag{6.11}$$

$$f_o(x) = \frac{1}{1+\lambda^2} \{ [1+\lambda^2 - 3 \tanh^2(x)] \sin(\lambda x) + 3\lambda \tanh(x) \cos(\lambda x) \},$$

$$E^{(0)} = q_{\parallel}^2 + 2 + \lambda^2/2, \tag{6.12}$$

where f_1 and f_2 are the bound states and f_o (f_e) are the odd (even) scattering

⁸If the system is finite in the y direction, then Eq. (6.7) is appropriately modified by changing the integral over k_y to a sum and allowing k_y to only take discrete values, in the same manner as k_z .

states; the associated dimensional energies $E^{(0)}$ are given by $E^{(0)} = k_B T \chi \xi^3 E^{(0)} / \mathcal{V}$. The parameter λ is nonnegative, $\lambda \geq 0$. Each of these states is normalized so that the amplitude of the fluctuation is equal to one when $x = 0$.

Since both f_1 and f_2 are localized in the boundary layer, we identify these modes as being responsible for interface fluctuations. In particular, a fluctuation of the form $\psi = f_1(x)e^{ik_y y + ik_z z}$ corresponds to an oscillation of the interface about its mean position without a broadening of the width of the boundary layer; see Fig. 6.2(iv) and Sec. 6.4. On the other hand, a fluctuation $\psi = f_2(x)e^{ik_y y + ik_z z}$ will lead to a variation of the boundary layer (or interface) thickness; see Fig. 6.2(v-vi). We refer to these two modes as LER and SAV fluctuations, respectively.

The solutions f_o and f_e remain non-zero over (essentially) the entire length of the system; they should be relatively high energy states, and consequently improbable. The f_o and f_e modes are fluctuations of the *composition profile*, as opposed to the interface profile.

For a system with $N > 1$ interfaces, Eq. (6.8) takes the approximate form,

$$0 = \partial_{xx} F + \lambda^2 F + l(l-1)F \sum_{j=1}^N \text{sech}^2[x - (j-1/2)L], \quad (6.13)$$

where $L = \ell/(\sqrt{2}\xi)$; corrections to the above expression are exponentially small. In the limit that $\xi \rightarrow 0$, we observe that Eq. (6.13) reduces to N copies of Eq. (6.6) on the domains $0 \leq x \leq \ell$, $\ell \leq x \leq 2\ell$, ..., $(N-1)\ell \leq x \leq N\ell$. Asymptotically, we may then solve Eq. (6.13) separately on each of these domains and paste the solutions together at the boundaries. This yields the (asymptotic) bound state eigenfunctions,

$$F_i(x; m) = \sum_{j=1}^N \Xi_j(m) f_i[x - (j-1/2)L], \quad (6.14)$$

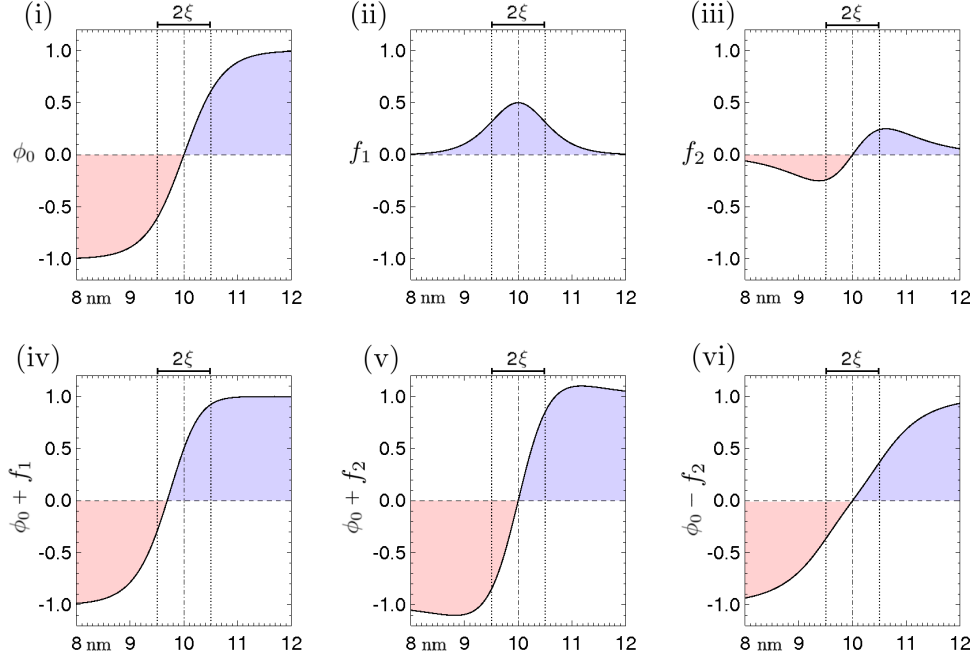


Figure 6.2: The effect of fluctuation modes f_1 and f_2 on ϕ_0 . In inset (i), we plot ϕ_0 for a single interface located at 10 nm with $\xi = 0.5$ nm. Insets (ii) and (iii) show the functions f_1 and f_2 localized at the interface. Inset (iv) shows that f_1 displaces the interface (i.e. the boundary layer) away from its mean position. Insets (v) and (vi) show that f_2 contracts [(v)] or expands [(vi)] the mean field interface width. As in the previous figures, red and blue shading indicates regions A and B monomer microdomains, respectively. Fluctuations of the type f_1 determine the LER, while fluctuations of the type f_2 affect the sidewall thickness or SAV. In each inset, the vertical, dotted lines remain unchanged in order to facilitate comparison.

where $i = 1$ or 2 , and the sets $\{\Xi_j(m)\}$ are phase factors chosen to ensure that we have a complete basis of states; there are N such sets, and m is an (as of yet unspecified) quantum number. Since f_1 and f_2 are approximately zero at the points $x = \ell, 2\ell, \dots, N\ell$, any orthonormal basis $\{\Xi_j(m)\}$ will yield eigenfunctions $F_i(x; m)$ that solve Eq. (6.13) up to exponential corrections. An obvious choice is the Kronecker delta function basis $\Xi_j(m) = \delta_{j,m}$, i.e. $\Xi_j = 1$ for $j = m$ and zero otherwise, where $1 \leq m \leq N$. This choice yields

$$F_i(x; m) = f_i(x; m) \equiv f_i[x - (m - 1/2)L]. \quad (6.15)$$

This basis is a set of eigenmodes corresponding to the N cases in which only one of the interfaces fluctuates.

The most natural generalization of f_o and f_e is

$$f_o(x; \lambda) = \frac{1}{1+\lambda^2} \left\{ (1 + \lambda^2 - 3\phi_0^2) \cos(\lambda x) - 3\lambda\phi_0 \sin(\lambda x) \right\}, \quad (6.16)$$

$$f_e(x; \lambda) = \frac{1}{1+\lambda^2} \left\{ (1 + \lambda^2 - 3\phi_0^2) \sin(\lambda x) - 3\lambda\phi_0 \cos(\lambda x) \right\}, \quad (6.17)$$

where we restrict λ to values for which $f_{o(e)}(0) = f_{o(e)}(NL) = 0$. These solutions solve Eq. (6.13) up to exponentially small corrections. Since we are interested solely in fluctuations of the boundary layer, we will omit the f_o and f_e modes when writing Eq. (6.5) in diagonal form. Moreover, it can be shown that the amplitude of these modes will have little effect on the boundary layer since they are suppressed by a factor of ξ/ℓ relative to the f_2 fluctuations.

From perturbation theory, it is well known that the first order correction to the energy eigenvalues can be written in general as $\int dV \Psi \hat{H} \Psi$, where \hat{H} is some

perturbing potential, and Ψ is a (real) eigenfunction of the leading order problem [126]. In our case, we find,

$$E_1^{(1)}(m, q_{\parallel}) \approx G(m\ell, m\ell) = \frac{\pi}{hq_{\parallel}} \left\{ \frac{\cosh[q_{\parallel}\ell N] + \cosh[q_{\parallel}\ell(N+1-2m)]}{\sinh(\ell N q_{\parallel})} \right\}, \quad (6.18)$$

$$E_2^{(1)}(m, q_{\parallel}) \approx 0, \quad (6.19)$$

where $E_1^{(1)}$ and $E_2^{(1)}$ are the first order energy corrections for the f_1 and f_2 states. In calculating Eqs. (6.18) and (6.19), we approximate $f_1(x; m) \approx \sqrt{2}\xi\delta(x - \ell(m - 1/2))$ and use the definition

$$\tilde{g}(\tilde{\mathbf{r}}, \tilde{\mathbf{r}}') = \sum_{m=-\infty}^{\infty} \sum_{\mathbf{k}_z} \int \frac{d\mathbf{k}_y}{2\pi} \frac{e^{i\mathbf{k}_z(z-z') + i\mathbf{k}_y(y-y')} \cos(\pi m x/LN) \cos(\pi m x'/LN)}{k_z^2 + k_y^2 + (\pi m/LN)^2}. \quad (6.20)$$

The first-order energy correction for f_2 modes is approximately zero because this mode is odd and changes rapidly compared to g . It is possible to continue perturbation theory indefinitely, computing corrections to the energy eigenfunctions and eigenvalues, but for our present purposes, Eqs. (6.18) and (6.19) suffice to approximate corrections to the LER.⁹

Considering only the contributions from f_1 and f_2 fluctuations, a given state of the system is now characterized by the respective amplitudes $|C_1^{(m)}(q_{\parallel})|^2$ and

⁹In the multiple interface problem, eigenstates $f_1(x; m)$ are degenerate, i.e. all $f_1(x; m)$ have the same energy for a fixed value of q_{\parallel} (the same applies to f_2 modes). From the perspective of degenerate perturbation theory, we therefore cannot use the Kronecker basis $\Xi_j(m) = \delta_{j,m}$ when looking for energy corrections beyond first order, or eigenfunction corrections beyond leading order; rather it is necessary to rewrite the $f(x; m)$ in a basis that is orthogonal in the non-local term. Applying the approximations that yield Eqs. (6.18) and (6.19), this procedure is achieved by solving the eigenvalue problem $\lambda \Xi_i = \sum_j G(\ell i, \ell j) \Xi_j$ which yields an orthogonal set of $\{\Xi_j(m)\}_{j=1}^N$ different from the Kronecker basis we chose here.

$|C_2^{(m)}(q_{\parallel})|^2$ of these eigenmodes; Eq. (6.5) is consequently written to first order in diagonal form as,

$$\mathcal{H}_1 = \frac{k_B T h \chi \xi^2}{\sqrt{18\mathcal{V}}} \sum_n \int \frac{dk_y}{2\pi} \sum_{m=1}^N \left\{ 2[q_{\parallel}^2 + G(m\ell, m\ell)] |C_1^{(m)}(q_{\parallel})|^2 + [q_{\parallel}^2 + 3/2] |C_2^{(m)}(q_{\parallel})|^2 \right\}, \quad (6.21)$$

where we have approximated $\int_{(m-1/2)\ell}^{(m+1/2)\ell} dx f_i^2(x; m) \approx \int_{-\infty}^{\infty} dx f_i^2(x; m)$, since the $f_i(x; m)$ are localized at the microdomain interfaces. Inserting Eq. (6.21) into Eq. (6.1), gives the probability of a given fluctuation mode.

6.4 Defining the line-edge roughness

In Figs. 5.2 and 6.2 we show heuristically how the f_1 modes give rise to the line edge roughness. It is also possible to show this analytically by deriving Eq. (6.4) in a way that manifestly yields f_1 modes as LER fluctuations. Specifically, we assume that $\phi = \phi_0[x + \xi\zeta(y, z)]$, where $\xi\zeta(y, z)$ is a sufficiently small fluctuation of the equilibrium interface profile; expanding ϕ in powers of ξ gives

$$\phi = \phi_0[x + \xi\zeta(y, z)] \approx \phi_0(x) + \xi\phi_0'(x)\zeta(y, z) + \frac{\xi^2}{2}\phi_0''(x)\zeta(y, z)^2, \quad (6.22)$$

where ϕ_0' , ϕ_0'' denote the first and second derivatives of ϕ_0 . Substitution of Eq. (6.22) into Eq. (5.11) (with $\varsigma = 0$) then yields,

$$\mathcal{H}[\zeta] \approx \frac{k_B T \chi}{\mathcal{V}} \int dV \left\{ \frac{\xi^2}{2} \left[(f_1')^2 \zeta^2 + \frac{f_1^2}{2} (\nabla_{\parallel} \zeta)^2 \right] - \frac{1}{2} f_1^2 \zeta^2 + \frac{3}{2} \phi_0^2 f_1^2 \zeta^2 \right\}. \quad (6.23)$$

Up to a scaling of the argument of ζ , Eq. (6.23) is in fact just Eq. (6.4) with $\psi = f_1 \zeta$. Comparison to Eq. (6.7) reveals that Eq. (6.23) can be diagonalized if ζ is written

as the product of Fourier modes in the y and z directions. Therefore, we may conclude that f_1 modes correspond to a *shift in position* of the interface, where ξ is the physical amplitude of the actual fluctuation.¹⁰ In passing we note that for arbitrary q_{\parallel} , the direction of the interface shift will depend on z ; however, when the film thickness h is small enough, the discrete k_z modes will be high energy, so that most fluctuations will be uniform throughout the height of the melt.

Based on the above analysis, we define the LER per Fourier mode q_{\parallel} and interface m as

$$\langle \zeta_m^2(q_{\parallel}) \rangle = \int D[\psi] \xi^2 |C_1^{(m)}(q_{\parallel})|^2 P[\psi] = \frac{\mathcal{V}}{h\chi} \left[\frac{3}{2\sqrt{2}\xi q_{\parallel}^2 + 6\varsigma h G(\ell m, \ell m)} \right], \quad (6.24)$$

where $D[\psi]$ is a functional measure over ψ and \mathcal{V} is a unit volume. We may define the LER of the m th interface in real space by integrating Eq. (6.24) with respect to q_{\parallel} ; specifically,

$$\sigma^2(m) = \sum_n \int \frac{dk_y}{2\pi} \langle \zeta_m^2(q_{\parallel}) \rangle = \sum_n \int \frac{dk_y}{2\pi} \frac{\mathcal{V}}{h\chi} \left[\frac{3}{2\sqrt{2}\xi q_{\parallel}^2 + 6\varsigma h G(\ell m, \ell m)} \right]. \quad (6.25)$$

Note that when $\varsigma = 0$, Eq. (6.25) *does not* depend on m ; since the f_1 modes asymptotically satisfy the homogeneous boundary conditions at $x = 0, N\ell$, the template can only affect interface fluctuations through the non-local term. Physically this makes sense; in the strong segregation regime, we expect polymer fluctuations to depend largely on the local behavior of the (mean-field) interface.

¹⁰While this procedure is useful for physically interpreting the f_1 modes, we cannot assume that an expansion having the form of Eq. (6.22) will yield all of the possible interface fluctuation modes; in fact, the assumptions underlying Eq. (6.22) completely neglect the possibility of the f_2 dilations. Hence, our original analysis based on Eq. (6.4) is necessary to account for the full behavior of the system.

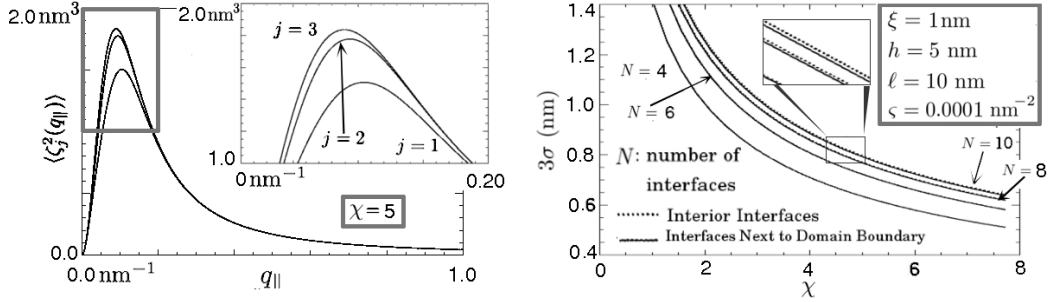


Figure 6.3: LER in frequency and real space. Inset (i) shows the amplitude $\langle \zeta_j^2(q_{\parallel}) \rangle$ for a system with 6 interfaces, a 10 nm half-pitch, and an interface thickness $\xi = 1$ nm. Note that $\langle \zeta_j^2(q_{\parallel}) \rangle = \langle \zeta_{7-j}^2(q_{\parallel}) \rangle$. Interfaces closer to the domain boundary in general have a smaller LER than interfaces in the middle of the domain; the figure shows, however, that only the low frequency fluctuations differ significantly among interfaces. Inset (ii) shows values of 3σ given by Eq. (6.25); at the 11 nm node, industrial specifications require that $3\sigma \leq 1.1$ nm. Our results therefore predict that χ must be increased by at least a factor of three or four above previous limits in order to bring copolymers within reach of industrial specifications. This figure also shows that the *number* of microdomains has a larger impact on LER than the *position* of an interface relative to the system boundary.

In a similar manner, we may define the SAV in Fourier space as

$$\langle [\Delta\vartheta_m(q_{\parallel})]^2 \rangle = \int D[\psi] \frac{\xi^2}{h^2} |C_2^{(m)}(q_{\parallel})|^2 P[\psi] = \frac{\mathcal{V}}{h^3 \chi} \frac{3\sqrt{2}\xi}{\xi^2 q_{\parallel}^2 + 3/2}. \quad (6.26)$$

In real space,

$$\langle (\Delta\vartheta_m)^2 \rangle = \sum_n \int \frac{dk_y}{2\pi} \langle [\Delta\vartheta_m(q_{\parallel})]^2 \rangle = \sum_n \int \frac{dk_y}{2\pi} \frac{\mathcal{V}}{h^3 \chi} \left[\frac{3\sqrt{2}\xi}{\xi^2 q_{\parallel}^2 + 3/2} \right]. \quad (6.27)$$

Equations (6.26) and (6.27) are motivated by the following picture. After removing the A monomers (for example), the height should be approximately zero in the (previously) A rich domains and roughly h in the B rich domains. Within the boundary layer, however, A and B components are mixed, so that any process that removes only A monomers will leave some residual amount of B. Consequently, we expect the height to be on average a decreasing (or increasing) function of position within this region; we assume that the width over which this fall (or rise) takes place is equal to the width of the boundary layer before etching, which is affected by the f_2 modes.

We therefore define the equilibrium sidewall angle, relative to the substrate normal, as $\vartheta \approx 2\xi/h$, namely as the ratio of the boundary layer width over the height of the melt. We may similarly approximate the change of the sidewall angle as $\Delta\vartheta = \Delta\xi/h$, where $\Delta\xi$ is a small change in width of the boundary layer due to an f_2 fluctuation. The variance of $\Delta\vartheta$ is then given by expressions (6.26) and (6.27). Although the SAV is not our main focus in this work, we note that controlling this quantity is nonetheless important for suppressing feature size variation across a semiconductor wafer.

We note that Eqs. (6.25) and (6.27) diverge logarithmically if we allow n and k_y to go to infinity. Following Semenov [119], we define a cutoff frequency such that $0 \leq q_{\parallel} \leq 2/\xi$, which renders the integral finite and bounded; this cutoff occurs because the mean field theory breaks down for fluctuation wavelengths that are the same order of magnitude as the interface thickness ξ .

6.5 Discussion

Our goals in this section are twofold. In Sec. 6.5.1, we explain the physics of LER on the basis of Eqs. (6.24) and (6.25); in the process, we discuss key approximations and limitations of our approach. In Secs. 6.5.2 and 6.5.3 we compare our analysis to experimental results and other models of LER. In Sec. 6.5.4 we consider the implications of Eq. (6.25) in the context of manufacturing specifications set forth by the ITRS.

6.5.1 Line-edge roughness from a mean-field perspective

6.5.1.1 Physics of line-edge roughness

Equation (6.24) can be viewed as a consequence of the equipartition of energy law, which states that for a system in thermal equilibrium, the amplitude squared of a given eigenmode is *inversely proportional* to the energy of that mode. In essence, the LER is *limited* by the energy cost of deforming the interface. From that perspective, we may view the two terms in the denominator of Eq. (6.24) as accounting for different physical *processes* that add to this total cost.

The first of these terms, $\chi h \xi q_{\parallel}^2$, is an interface tension arising from the repulsive interaction between A and B monomers. This is seen by appropriately factoring the product, since, (i) ξh is the area scale associated with a x - z cross section of the interface, while (ii) for mode q_{\parallel} , the average increase in length of the interface is proportional to q_{\parallel}^2 (under a small fluctuation approximation). Therefore, a mode q_{\parallel} will increase the number of repulsive A-B crossings (which occur in the interface region) by a factor of $h \xi q_{\parallel}^2$ (in a mean-field sense), with the additional factor of χ in Eq. (6.24) accounting for the energy cost of these crossings.

The second process described by $\chi \varsigma G(m\ell, m\ell) \sim \mathcal{N}^{-2}$ depends on the radius of gyration $R_g \sim \mathcal{N}^{1/2}$, but not χ ; we conclude that this product accounts for the energy penalty of stretching or compressing the polymers in the vicinity of a fluctuating interface. This interpretation is consistent with Ohta and Kawasaki's original reason for including the non-local term $\varsigma g(\mathbf{r}, \mathbf{r}')$ in Eq. (5.11), namely, to account for correlations arising from the connected nature of the polymers. The fact that only the diagonal elements of G appear in Eq. (6.24) indicates that the first order response of the system is determined only by local re-ordering of the polymers near an interface. Continuing to higher orders in perturbation theory will in principle yield corrections proportional to $G(m\ell, m'\ell)$, i.e. energy costs associated with correlated stretching of polymers at different interfaces.

6.5.1.2 Limitations of the approach

We stress that while this mean-field model provides simple physical pictures of and analytic expressions for the LER, caution should be exercised when considering systems whose half-pitch is of the order of a few nanometers. At such length scales, close examination of the parameters entering the model reveals that we push it to the limits of its validity. Notably, for a physical system in which $\xi = 1$ nm and $\ell = 10$ nm, we find that $a^2 = 3\chi\xi^2/4$, which is $\mathcal{O}(1)$ nm² for $\chi = 1$. Since we expect that the Kuhn length is the smallest meaningful length scale in our model, it is unclear that our analysis will be valid when $a/\xi > \mathcal{O}(1)$, or $\chi > \mathcal{O}(1)$.

The perturbation methods we use, while approximate, pose less of a problem with regard to the validity of our analysis. We noted in Sec. 6.2 that the parameter ς must be small. We can estimate how small it must be from dimensional analysis; specifically, the product $\ell^2\varsigma$ should be the largest combination of terms involving ς in our perturbation analysis, so that whenever $\ell^2\varsigma \ll 1$, our analysis should be valid. We can estimate ς from its definition in Eq. (5.12). Taking $\xi = 1$ nm and letting $\mathcal{N} \approx 300$, we find that $\varsigma \approx (7.5 \times 10^{-3})/\chi^2$ nm⁻². If we use $\chi = 10$ as an upper limit suggested by our analysis, then we find $\ell^2\varsigma \approx 7.5 \times 10^{-3}$ is sufficiently small in the regimes we consider. Values as low as $\chi \approx 3$ yield $\ell^2\varsigma \approx 10^{-1}$.

6.5.2 Comparison of our results to experiments

In the previous section, we showed that the LER (as predicted by the LOK mean-field model) is limited by an effective surface tension and a stretching energy.

It is useful to consider the scaling behavior of these energies in a generic sense; i.e.

$$\langle \zeta^2(k) \rangle \sim (k^2 + c/k^2)^{-1}, \quad (6.28)$$

with c some constant and k a frequency. The second term c/k^2 is the Fourier space scaling of the Green's function (which can be understood as $g \sim \nabla^{-2}$ in real space). In the two asymptotic limits $k \rightarrow 0$ and $k \rightarrow \infty$, the LER is dominated by the stretching energy and surface tension, respectively. However, our perturbation approach implies that $c \sim \mathcal{N}^{-1/2}$, so that the contribution to the LER from the stretching energy is only apparent for very long wavelength fluctuations, for which it quickly becomes dominant. Figure 6.3(i) shows, for example, the asymptotic behavior of the LER power spectral density (PSD) for a 10 nm half-pitch system; the maximum occurring at $q_{\parallel} = \mathcal{O}(0.1) \text{ nm}^{-1}$ is the approximate length scale at which the stretching energy becomes important.

Many experiments have demonstrated a power law decay in the LER PSD with the long wavelength behavior $\langle \zeta^2(k) \rangle \sim k^{-1.6}$, as opposed to the scaling given by Eq. (6.28) [or Eq. (6.29) discussed below] [123, 127]. Previous works noted the disagreement between experimental and theoretical results, although to the best of our knowledge the reasons for this disagreement are still not understood [123]. Moreover, these experiments did not indicate a sharp drop as $q_{\parallel} \rightarrow 0$. However, in the case of Reference (26), for example, estimates of c appearing in Eq. (6.28) suggest that the PSD maximum should occur near $q_{\parallel} = \mathcal{O}(1) \mu\text{m}^{-1}$, i.e. the smallest value of q_{\parallel} that was resolved by their experiments; hence, we do not expect the $q_{\parallel} \rightarrow 0$ behavior of the PSD to be evident in the analysis of their data. In general, the

stretching energy should become more important as the half-pitch becomes smaller, since $\varsigma \sim \mathcal{N}^{-2}$ becomes larger in this limit (c.f. also Fig. 6.3).

6.5.3 Comparison of our results to other models

Starting from the LOK energy functional Eq. (5.11), Bosse studied the steady state (or equilibrium) LER of lamellar interfaces using a series of stochastic simulations based on a Cahn-Hilliard update equation for the density ϕ [113]; however, he introduced subtleties that affect the LER PSD. Specifically, his analysis is equivalent to solving the eigenvalue equation $E\phi = \nabla^2(\delta\mathcal{H}[\phi]/\delta\phi)$, where $\delta\mathcal{H}[\phi]/\delta\phi$ indicates a variational derivative of \mathcal{H} with respect to ϕ ; our analysis omits the extra factor of ∇^2 . The inclusion of this factor eliminates the singular behavior of PSD as $q_{\parallel} \rightarrow 0$; viz. his equilibrium PSD scales like

$$\zeta(k) \sim (k^4 + c)^{-1}, \quad (6.29)$$

which approaches a positive constant when $k \rightarrow 0$ (again, c is a constant). The differences between Eqs. (6.28) and (6.29) can be detected by experimentally, although, as we have indicated above, the $k \rightarrow 0$ behavior of the system can likely only be studied for systems with half-pitches less than about 10 nm.

When the stretching energy is negligible, our model of LER reduces to another well known phase field model derived by Semenov, who found a nearly identical expression to Eq. (6.24) (with $\varsigma = 0$) by starting from a free energy significantly different from Eq. (5.11) [119,123]. This fact suggests a deeper connection between the analysis of Refs. [9,21] and ours, which we explore here. Starting from his

expression,

$$F[\phi_A, \phi_B] = \frac{a^2}{4\mathcal{V}} \int d\Omega \frac{(\nabla\phi_A)^2}{\phi_A} + \frac{(\nabla\phi_B)^2}{\phi_B} + \frac{4\mathcal{V}\chi}{a^2} \phi_A \phi_B, \quad (6.30)$$

and noting that $\phi_B = 1 - \phi_A$ and $\phi = \phi_A - \phi_B$, it is possible to write Eq. (6.30) as

$$F[\phi] = c \int d\Omega \left[\frac{1}{1 - \phi^2} \right] \left\{ \xi^2 \frac{(\nabla\phi)^2}{2} + \frac{(1 - \phi^2)^2}{4} \right\}, \quad (6.31)$$

where c is some constant.

Equation (6.31) is of the same form as Eq. (5.11) (with $\varsigma = 0$) *except* for the factor of $(1 - \phi^2)^{-1}$ appearing in the integrand. This similarity ensures that both Eqs. (5.11) and (6.30) *have the same minimum*, as can be seen by taking a variational derivative of Eq. (6.30) with respect to ϕ . Specifically, if $\mathcal{L}_1 = (1 - \phi^2)^{-1}$, $\mathcal{L}_2 = (\xi^2/2)(\nabla\phi)^2 + (1 - \phi^2)^2/4$, and $\mathcal{L} = \mathcal{L}_1\mathcal{L}_2$, then

$$\left. \frac{\delta\mathcal{L}}{\delta\phi} \right|_{\phi=\phi_0} = \mathcal{L}_2 \left. \frac{\delta\mathcal{L}_1}{\delta\phi} \right|_{\phi=\phi_0} + \mathcal{L}_1 \left. \frac{\delta\mathcal{L}_2}{\delta\phi} \right|_{\phi=\phi_0} = 0, \quad (6.32)$$

by virtue of the fact that ϕ_0 minimizes \mathcal{L}_2 and $\mathcal{L}_2[\phi_0] = 0$; therefore, ϕ_0 is also a minimum of Eq. (6.30).

The factor of $(1 - \phi^2)^{-1}$ appearing in Eq. (6.30) necessarily leads to a different equation for the fluctuations of the system around the configuration ϕ_0 . Remarkably, however, Semenov's free energy yields an equation for ψ that has the exact form of Eq. (6.8), but with $l = 2$ (as opposed to $l = 3$ for the LOK model). For $l \geq 2$ it is known that the Pöschl-Teller equation has bound states analogous to the f_1 fluctuation modes, which allowed Semenov to define the LER on the basis of these interface fluctuations [124]. The $l = 3$ case differs notably from the $l = 2$ case in

that the former also predicts the existence of f_2 fluctuations while the latter does not.

6.5.4 Line-edge roughness in a manufacturing setting

The ITRS specifies that the LER must satisfy $3\sigma < 1.1$ nm at the 11 nm node. In Fig. 6.3 we estimate values of χ that will be required to reach these goals. Using the the values $\mathcal{N} = 300$, $\xi = 1$ nm, $\ell = 10$ nm [44], Eq. (6.25) predicts that values of $\chi \approx 3$ or greater will be required to reduce the LER to within acceptable limits. These values of χ are extremely large relative to what is seen in many experiments, where typical values range from roughly 10^{-2} for PS-PMMA [poly(styrene-*b*-methyl methacrylate)] to 10^{-1} for PS-PDMS [poly(styrene-*b*-dimethylsiloxane)] [15, 116–118, 128]. Although effective values of χ as large as 1 have been reported in some systems [15], our results suggest that at least a three-fold increase in χ is necessary to reach target goals at the 11 nm node.

Our analysis reveals a connection between the LER and the number and position of microdomains between template boundaries. Figure 6.3(ii) provides a representative illustration showing that for fixed χ and ℓ , decreasing the number of microdomains can reduce the LER by a factor of 10% or more. On the other hand, the position of the individual microdomains within the actual system has a much smaller effect on the LER.

While the values of χ that we report here are relatively large, we caution that the analysis herein should be taken more as a qualitative estimate of the necessary

system parameters as opposed to a strict, quantitative prediction. As noted in Sec. 6.5.1, we begin to push the model to the limits of its validity when $\chi \gg 1$ and the half-pitch approaches 10 nm or less.

We end this section by noting that the Eqs. (6.25) and (6.27) reveal an interesting, although not entirely unexpected, connection between the LER and the SAV. Specifically, the mean-field interface width ξ sets the length scale of both the LER and the SAV. Physically, this is reasonable, since both quantities refer to properties of the interface itself. However, in the context of a continuum theory, where the notion of an interface itself does not arise explicitly, it is gratifying to find that all of its associated length scales are nonetheless determined by the single parameter ξ . This internal consistency suggests that despite its possible shortcomings, the LOK phase-field model can provide significant physical insight into the behavior of block copolymer systems.

6.6 Summary

In this chapter, we used the Leibler-Ohta-Kawasaki phase field model to calculate the LER and SAV of microdomain interfaces for a system of lamellar block copolymers whose order is established by straight, parallel template walls; we showed how the LER depends on the Flory-Huggins parameter, index of polymerization, and position of the interface relative to the template walls. Our analysis reveals that the main contributions to LER arise from (i) a surface tension resulting from the A-B monomer repulsion, and (ii) an energy associated with stretching the polymers in

the vicinity of an interface fluctuation. Using values of the \mathcal{N} (the index of polymerization) and ξ the (interface thickness) that correspond roughly to an 11 nm half-pitch, we predict that the Flory-Huggins parameter χ must be increased by roughly a factor of three or four above current experimental values in order to reach target goals for the LER set forth in the ITRS. As our analysis is concerned primarily with fluctuations in the bulk of the film (i.e. away from the top and bottom of the system), an important extension of our work would be to include the effects of polymer interactions with both the substrate and the material bounding the film from above; we speculate that one can account for such effects by the introduction of a suitable surface integral to the LOK Hamiltonian.

Chapter 7

Conclusion

7.1 Summary of main results

Asymptotic methods are powerful tools for studying morphological and statistical properties of interfaces in condensed matter systems. In this dissertation, I showed how such techniques can be applied to steps on vicinal surfaces and microdomain interfaces in block-copolymers.

A critical task is to define what one means by an interface, especially since the goal of modeling is to compare theoretical predictions with experimental results, which are always subject to interpretation. In the context of steps on a vicinal surface, our definition of a step was motivated by measurements of step fluctuations and terrace-width distributions. Starting with a stochastic, lattice-gas model of the surface, we defined the *mesoscale* step position as an ensemble average over a corresponding microscopic step position and showed that the evolution of the former is described by a free-boundary, BCF-type theory. The notion of averaging, in particular, was the key idea that allowed us to bridge the two length scales. By modifying the BCF theory to account for interactions between multiple steps and stochastic fluctuations, we were also able to formulate and solve an analytic model for the TWD.

For block-copolymers, our notion of an interface was motivated by SEM images

of the BCP microdomains. We interpreted the interface position in the context of the LOK phase-field model as corresponding to the locations where the relative density of the monomer species changes sign. In contrast to vicinal surfaces, this definition was imposed after coarse-graining, not during the derivation of the LOK functional. By using variational principles and ideas from functional calculus, we determined the fluctuation spectrum of the BCP microdomain interfaces and predicted values of the Flory-Huggins parameter that are necessary to bring LER within industrial specifications.

It is interesting to observe that despite significant differences in the modeling and microscopic physics of vicinal surfaces and BCPs, the two systems can nonetheless often be described by similar mesoscale principles. In particular, we noted in Sec. 6.5.1.1 that the LER of BCPs is limited by an effective surface tension that arises from the repulsive A-B interactions; this observation has led to capillary-wave models that describe fluctuations of BCP microdomain interfaces [123]. While we did not consider 2D crystal surfaces here, other works have characterized 2D step fluctuations using the related concept of line tension [40, 41]; cf. also Ref. [8].

Significant differences also exist between BCPs and vicinal surfaces. For one, the low-frequency behavior of BCP microdomain interfaces (which is dominated by the non-local interactions between polymers) differs from the predictions of capillary wave models that apply to steps. Another notable example includes the effect that the relative position of microdomains has on the interface fluctuations. Vicinal Si(100), for example, is composed of alternating A and B terraces, which are characterized by the presence of dimer rows that are parallel or perpendicular to

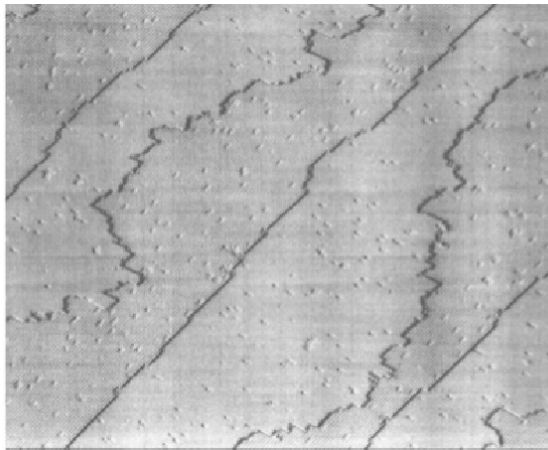


Figure 7.1: Scanning-tunneling microscope image of Si(100) surface (top-down). Note that the roughness of steps alternates depending on whether the A terrace is below or above the step. Taken from Ref. [129]

the mean step orientation, respectively [93, 129] (cf. Fig. 7.1). Importantly, the roughness of the step profile depends on whether or not the A terrace is above or below the step.¹ In BCP systems, however, the orientation of the microdomains relative to the interfaces does not affect fluctuations in the latter. In our analysis, this observation is a consequence of the fact that the LOK model treats the A and B monomers interchangeably.

7.2 Open problems

While the work in this dissertation shows that many problems can and have been solved in multiscale modeling of crystalline and polymer interfaces, many questions remain.

¹This fact can be traced back to the idea that the diffusion of adatoms is anisotropic and depends on the orientation of the dimer rows relative to the step [93, 129].

In the context of vicinal surfaces, an important task is to generalize the derivation of Chapter 3 to systems in 2+1D. The analysis of that chapter is unable to account for step curvature, which is expected to modify the step chemical potential appearing in the linear kinetic relation. We speculate that the key difficulty in generalizing this result will be to establish an appropriate analytical framework within which to perform the derivation. Additional questions concern the atomistic origins of step interactions and noise, whose forms we did not derive from the SLG model.

In block-copolymer systems, an important task is to extend the results of Part II to BCP microdomains with more complicated geometries and systems with chemoepitaxial templates. Such systems are of great interest to the lithography industry, which is seeking to obtain as much information about BCPs as possible. To this end, finding analytic predictions for LER on the basis of self-consistent field theory (without the mean-field approximation) is also of use to industry.

7.3 Closing statements

The open problems discussed above fit into a broader class of questions that are of current interest to the scientific community. From the standpoint of non-equilibrium statistical mechanics, developing general techniques for coarse-graining stochastic, atomistic models [such as Eq. (2.2)] is largely unexplored, despite the emerging awareness that new approaches are needed for such problems. For example, master equation formulations of soft matter and biological systems have become increasingly popular [55]. These models often suffer from the complexity of having

large numbers of particles that interact with free boundaries and could benefit from coarse-graining techniques similar to the ones that we employ.

In the context of industrial applications, one of the key challenges that scientists face is how to solve problems with well-understood principles but exceedingly complicated geometries. For example, how does one calculate the electrical properties of aircraft wing constructed of a carbon nanotube/epoxy mixture? In principle, this problem can be formulated in terms of Maxwell's equations, but in practice even numerical simulations have difficulty solving it. Consequently, there is a need to improve the asymptotic approaches (based on physical insight) that are used in such applications.

Appendix A

Asymptotic calculations of the mean field and terrace-width distribution

A.1 Time independent terrace-width distribution and mean field

Our task in this section is to solve the system of Eqs. (4.26) and (4.29) in light of expansions (4.27) and (4.28). If the TWD is sharply peaked at, say, $s = \zeta$, and decays rapidly to zero away from ζ , then Eq. (4.26) can be simplified via asymptotics [106]. Thus, we expand $\tilde{\mathcal{A}}(s, y_1, y_2)$ about $y_1 = y_2 = \zeta$. Recall that the analysis of Sec. 4.2.4 indicates that, for $g \gg 1$, the standard deviation of the (Gaussian within the linear model) TWD is $O(g^{-1/2})$. This scaling with g of the standard deviation should also hold for the present MF case since the linear analysis is reasonably valid near the TWD peak.

Next, we comment on ζ . By setting $\partial_t P(s, t) = 0$ in Eq. (4.17), we obtain

$$P''(s) = \frac{g}{3} \times \left[\left(\frac{4}{c+s} + \frac{2}{c+f(s)} \right) \left(\frac{1}{s^3} - \frac{1}{f(s)^3} \right) P(s) \right]', \quad (\text{A.1})$$

where the prime here denotes differentiation with respect to s , e.g., $P'(s) = dP(s)/ds$.

With $P(s) \geq 0$, we have $P''(\zeta) < 0$ and $P'(\zeta) = 0$ when $\zeta = f(\zeta)$ (which defines the maximum of P).

The substitution of formulas (4.27) and (4.28) into Eq. (4.26) along with the

Taylor expansion of $A(s, y_1, y_2)$ around $y_1 = y_2 = \zeta$ yield the expression

$$\begin{aligned}
& \left[\frac{4}{c+s} + \frac{2}{c+f_0} \left(1 - \frac{f_1(s)}{g^\alpha(c+f_0)} + \dots \right) \right] \\
& \quad \times \left[\frac{1}{s^3} - \frac{1}{f_0^3} \left(1 - \frac{3f_1(s)}{g^\alpha f_0} \right) \right] = \\
& \int_{\mathbb{R}_+^2} dy_1 dy_2 P(y_1) P(y_2) \\
& \times \left\{ \frac{4}{s+c} \left[\frac{1}{s^3} - \frac{1}{f_0^3} + \frac{3(y_1-f_0)}{f_0^4} - \frac{12(y_1-f_0)f_1(\zeta)}{g^\alpha f_0^5} + \dots \right] \right. \\
& \quad + 2 \left[\frac{1}{c+f_0} - \frac{y_1-f_0}{(c+f_0)^2} + \frac{2f_1(\zeta)(y_1-f_0)}{g^\alpha(c+f_0)^3} + \dots \right] \\
& \quad \times \left[\frac{1}{s^3} - \frac{1}{f_0^3} + \frac{3[2(y_1-f_0) - (y_2-f_0)]}{f_0^4} \right. \\
& \quad \left. \left. - \frac{12f_1(\zeta)}{g^\alpha f_0^5} [2(y_1-f_0) - (y_2-f_0)] + \dots \right] \right\}, \tag{A.2}
\end{aligned}$$

which, by dominant balance in g , leads to a cascade of equations for f_k . In deriving Eq. (A.2), we made extensive use of the binomial expansion, $(1+z)^\varsigma = 1 + \varsigma z + \dots$ ($|z| < 1$, $\varsigma \in \mathbb{R}$), as well as of the expansion for $f(\zeta)$ by Eq. (4.27). Note that expanding A gives rise to terms $(y_{1,2} - f_0)^n$, $n = 1, 2, \dots$, which yield an *implicit* dependence on g through the associated moments of P . A crucial goal with the perturbation scheme is to determine the expansion order in g of these moments. This in turn determines α .

By virtue of Eqs. (4.27) and (4.28), Eq. (4.29) entails

$$\begin{aligned}
& \frac{d^2}{ds^2} \left[P_0(s) + \frac{P_1(s)}{g^\alpha} + \dots \right] \\
&= \frac{g}{3} \frac{d}{ds} \left\{ \left(\frac{4}{c+s} + \frac{2}{c+f_0} - \frac{2f_1(s)}{g^\alpha(c+f_0)^2} + \dots \right) \right. \\
&\quad \times \left(\frac{1}{s^3} - \frac{1}{f_0^3} + \frac{3f_1(s)}{g^\alpha f_0^4} + \dots \right) \\
&\quad \left. \times \left[P_0(s) + \frac{P_1(s)}{g^\alpha} + \dots \right] \right\}. \tag{A.3}
\end{aligned}$$

Equations (A.2) and (A.3) form the basis of our approximation scheme for $f(s)$ and $P(s)$.

By dominant balance, from Eq. (A.2) we obtain an $O(g^0)$ equation for f_0 :

$$\begin{aligned}
A(s, f_0) = \int_0^\infty P(y_1) \left\{ A(s, f_0) + (y_1 - f_0) \left[\frac{12}{f_0^4(s+c)} \right. \right. \\
\left. \left. - \frac{2}{(c+f_0)^2} \left(\frac{1}{s^3} - \frac{1}{f_0^3} \right) + \frac{6}{f_0^4(c+f_0)} \right] \right\} dy_1. \tag{A.4}
\end{aligned}$$

Recall that $P(y)$ is normalized, and its mean is unity. Thus, Eq. (A.4) reduces to

$$\int_0^\infty P(y_1)(y_1 - f_0) dy_1 = 0, \tag{A.5}$$

which readily implies $f_0 = 1$.

By Eq. (A.3) with $f_0 = 1$, the zeroth-order TWD, $P_0(s)$, satisfies the differential equation

$$P_0''(s) = \frac{g}{3} \left[\left(\frac{4}{c+s} + \frac{2}{c+1} \right) \left(\frac{1}{s^3} - 1 \right) P_0(s) \right]', \tag{A.6}$$

subject to boundary conditions (4.18b). Equation (A.6) is integrated directly to give Eq. (4.30).

Next, we determine the α entering expansions (4.27) and (4.28). By Eq. (A.2), the value of α comes from balancing the $\mathcal{O}(g^{-\alpha})$ term on the left-hand side with the

$\mathcal{O}(g^{-1})$ term from the variance of P_0 , σ_0^2 (cf. Eq. (4.31)), on the right-hand side.

Thus, we find $\alpha = 1$.

Next we focus on $f_1(s)$, the coefficient of the $\mathcal{O}(g^{-1})$ term in the expansion for f . By use of Eqs. (A.2) and (4.31), we obtain Eq. (4.32). We add in passing that the location $\zeta = f(\zeta)$ of the TWD maximum cancels to $\mathcal{O}(g^{-1})$ in Eq. (A.2), and thus does not appear in expression (4.32).

A.2 Approximation of the mean-field variance

In this subsection, we derive Eq. (4.31), the leading-order variance for the steady-state TWD, $P_0(s)$. By Eq. (A.6), we write the MF variance from Eq. (4.30) as

$$\begin{aligned} \sigma_0^2 &= \mathcal{N}_0 \int_0^\infty (y-1)^2 \\ &\quad \times \exp \left\{ \frac{g}{3} \int_1^y \left[\frac{4}{\xi+c} + \frac{2}{c+1} \right] \left[\frac{1}{\xi^3} - 1 \right] d\xi \right\} dy \\ &= \mathcal{N}_0 \int_0^\infty (y-1)^2 \exp \left(\frac{g}{3} \int_1^y A(\xi, 1) d\xi \right) dy. \end{aligned} \quad (\text{A.7})$$

Next, we compute integral (A.7) by a change of variable. So, define the mapping $y \mapsto v$ where

$$v(y) = \frac{g}{3} \int_1^y A(\xi, 1) d\xi, \quad (\text{A.8})$$

$$v(y) \rightarrow 0 \quad \text{as } y \rightarrow 1, \text{ and}$$

$$v(y) \rightarrow -\infty \quad \text{as } y \rightarrow 0 \text{ or } y \rightarrow \infty.$$

Note that $y(v)$ is a double-valued function of v . To render $y(v)$ single valued, one must restrict y in $(0, 1)$ or $(1, \infty)$ (i.e., on the left or right of the maximum of $P_0(s)$),

as suggested by Fig. 3.1). Hence, we write Eq. (A.7) as

$$\begin{aligned}
\sigma_0^2 &= \mathcal{N}_0 \int_0^1 (y-1)^2 e^{v_-(y)} dy \\
&\quad + \mathcal{N}_0 \int_1^\infty (y-1)^2 e^{v_+(y)} dy \\
&= \frac{3}{g} \mathcal{N}_0 \left\{ \int_{-\infty}^0 [y(v_-) - 1]^2 \frac{e^{v_-}}{A(y(v_-), 1)} dv_- \right. \\
&\quad \left. - \int_{-\infty}^0 [y(v_+) - 1]^2 \frac{e^{v_+}}{A(y(v_+), 1)} dv_+ \right\}, \tag{A.9}
\end{aligned}$$

where $v_{+(-)}$ represents values of v if $y > 1$ ($0 < y < 1$).

Regarding the normalization constant \mathcal{N}_0 , we note that

$$\begin{aligned}
\mathcal{N}_0 &\left[\int_0^1 e^{v_-(y)} dy + \int_1^\infty e^{v_+(y)} dy \right] \\
&= \frac{3\mathcal{N}_0}{g} \left[\int_{-\infty}^0 \frac{e^{v_-}}{A(v_-, 1)} dv_- - \int_{-\infty}^0 \frac{e^{v_+}}{A(v_+, 1)} dv_+ \right] \\
&= 1. \tag{A.10}
\end{aligned}$$

The task is to compute \mathcal{N}_0 and thereby σ_0^2 . Since $dy = 3 dv_\pm / g A(y(v_\pm), 1)$, the transformed integrand as a function of v_\pm exhibits a singularity as $v_\pm \rightarrow 0$.

We first derive an explicit expression for y as a function of v_\pm . By the definition of $v(y)$, Eq. (A.8), for large g we expect that the major contribution to integration in Eq. (A.10) stems from a neighborhood of $v_\pm = 0$, or $y = 1$. Hence, by Taylor expanding the right-hand side of Eq. (A.8) around $y = 1$ we have

$$y - 1 = \pm \sqrt{\frac{-(c+1)v_\pm}{3g}} + \mathcal{O}(g^{-1}), \tag{A.11}$$

as $v_{\pm} \rightarrow 0$. So, we obtain the simplified expression

$$\begin{aligned}
\frac{gA(y(v_{\pm}), 1)}{3} &\sim \frac{g}{3} \left[\frac{4}{c+1 \pm \sqrt{\frac{-(c+1)v_{\pm}}{3g}}} + \frac{2}{c+1} \right] \\
&\quad \times \left[\left(1 + \sqrt{\frac{-(c+1)v_{\pm}}{3g}} \right)^{-3} - 1 \right] \\
&\sim \pm 2 \sqrt{\frac{-3gv_{\pm}}{c+1}} \quad \text{as } v_{\pm} \rightarrow 0 .
\end{aligned} \tag{A.12}$$

Thus, to leading-order in g , we assert that

$$1 = \int_0^{\infty} P_0(y) dy \sim \mathcal{N}_0 \int_{-\infty}^0 \sqrt{\frac{c+1}{-3gv}} e^v dv , \tag{A.13}$$

which in turn implies

$$\mathcal{N}_0 = \mathcal{N}_0(g, c) \sim \sqrt{\frac{3g}{\pi(c+1)}} . \tag{A.14}$$

The substitution of Eqs. (A.11), (A.12), and (A.14) into Eq. (A.9) yields formula (4.31).

Appendix B

1D kinetic Monte Carlo simulations for terrace-width distribution

In this appendix, we provide some details on the 1D kMC method used in Chapter 4. This algorithm describes the general methods set forth in Refs. [56, 66]. We consider a system of descending steps (Fig. 4.1), which are viewed as particles at positions x_j on a lattice with spacing Δx in 1D. We apply screw periodic boundary conditions, so that when a step moves off from one end, another step re-enters from the other end. The particles are only allowed to move to lattice sites, and overlaps and crossings are prohibited.

We proceed to prescribe the particle kinetics. The j th step is assigned two energy barriers, $E_j(\pm\Delta x)$: one for the step to move right (+) and another barrier for the step to move left (-). Each of these barriers forms a linear combination of four repulsive energies, each proportional to the inverse distance squared between a given step and one of its four nearest neighbors, i.e.,

$$E_j(\pm\Delta x) = \sum_{\substack{k=j-2 \\ k \neq 0}}^{j+2} \frac{b}{|x_j \pm \Delta x - x_{j+k}|^2} - \frac{b}{|x_j - x_{j+k}|^2}, \quad (\text{B.1})$$

where b is an adjustable parameter with units of area times energy. By Eq. (B.1), if a step is one lattice site (distance Δx) away from one of its nearest neighbors, the energy barrier for closer approach becomes infinite, prohibiting movement. Thus, for each of the two directions that a step is allowed to move to, we define the transition

rate

$$\mathcal{T}_j(\pm\Delta x) = \exp\left(\frac{-E_j(\pm\Delta x)}{k_B T}\right). \quad (\text{B.2})$$

We subsequently define two “movement classes” for right- and left-moving particles (steps). The corresponding total rate is taken to be

$$\mathcal{T}_{\text{tot}}^\pm = \sum_j \mathcal{T}_j(\pm\Delta x). \quad (\text{B.3})$$

Transitions requiring infinite energy do not contribute to this sum. After division by $\mathcal{T}_{\text{tot}}^+ + \mathcal{T}_{\text{tot}}^-$, Eq. (B.3) yields the probability that *some* step moves either left or right.

Three random numbers between 0 and 1 are generated and used in the following way. The first number determines from which movement class to select a particle to move according to the relative ratios of the two total class rates. The second random number picks the particle within the movement class that will move. Lastly, the third number, say r_3 , determines for how long (in simulation time) the transition occurs according to the relation $\Delta t = -f_{\text{attempt}} \ln(r_3)$, where f_{attempt} characterizes how often the step attempts to leave its lattice site. The constant f_{attempt} is kept at a fixed value (equal to 10 in our simulations), since the time scaling of the simulation can be chosen at will.

After performing these tasks, we update the position of each step and iterate the procedure for a specified number of times. For the b entering Eq. (B.1) we use values ranging from 1×10^0 to 2×10^6 . These high numbers might seem puzzling. However, our 1D model does *not* follow adatoms but steps. For the sake of comparisons with our analytical results, we fix the number of steps at 50, with a uniform, initial spacing of 100 lattice units (length $100\Delta x$). The large initial step spacing

is due to the need to have fine scale resolution of the kMC TWD peak in order to compare it with the analytically derived TWD.

To reach the steady state, we run simulations of 5×10^4 and 10^5 iterations; we average over 10^4 runs. A characteristic feature of these runs with $0 < b \leq \mathcal{O}(10^2)$ is a *tendency* exhibited by the TWD to approach a Poisson distribution for long times, with the TWD peak moving nearly to zero terrace width. The singular interaction, however, always prevents the steps from touching or crossing, and hence the TWD goes sharply to zero for zero terrace width. With increasing interactions, the peak tends not to move as far left (close to the origin), and the system equilibrates much more quickly.

Fitting the analytic TWD's (4.30) or (4.33) to the kMC TWD requires the determination of both the parameters c and g . Recall that g is a measure of the interaction strength, while c is a length expressing the interplay between diffusion and attachment-detachment processes *of adatoms*. We cannot estimate a priori what value of c corresponds to our kMC simulation because the algorithm follows steps and not adatoms.

Since the peak of the kMC TWD moves left of the initial width for all values of b studied, neither the LM nor the ZO TWD provides a good fit to the kMC results except when $b = \mathcal{O}(10^6)$ (when all of the analytic TWD's approach a Gaussian distribution). Hence, the composite TWD (4.33) is used in all cases to determine c and g . We find that for any *fixed* $c \geq \mathcal{O}(10)$, g may be used as the sole fitting parameter, and that for fixed b , changing the value of c ($c \geq \mathcal{O}(10)$) does not noticeably change the fit, provided the ratio g/c is constant. This last observation

is justified by examination of Eqs. (4.32) and (4.33); when $c \geq \mathcal{O}(10)$, the correction to the mean field f_1/g scales approximately as $c/3g$, and $gA(s, f) \approx (6g/c)(s^{-3} - f^{-3}(s))$. In the end, for our kMC simulation we have $1650 \leq g \leq 8400$.

For values of $c < \mathcal{O}(10)$, the peak of the analytic solution is to the left of the kMC TWD peak, and no value of g provides a good fit. Hence, our kMC simulation corresponds to a system in which attachment-detachment limited kinetics are the dominant mass transport mechanisms.

Bibliography

- [1] P. Nozières, in *Solids Far from Equilibrium*; C. Godrèche, Ed.; Cambridge University Press: Cambridge, UK, 1991.
- [2] Y. -C. Tseng and S. B. Darling, *Polymers* **2**, 470 (2010).
- [3] S. G. Davison and M. Stęślička, *Basic Theory of Surface States*; Oxford U Press: Oxford, 1996.
- [4] P. Han and P.S. Weiss, *Surf. Sci. Rept.* **67**, 19 (2012).
- [5] G. D. Mahan *Many-Particle Physics*, 3rd ed.; Kluwer Academic/Plenum Publishers: New York, 2000.
- [6] R. Balescu, *Equilibrium and Non-equilibrium Statistical Mechanics*; Wiley: New York, 1975.
- [7] R. C. Nelson, T. L. Einstein, S. V. Khare, P. J. Rous, *Surf. Sci.* **295**, 462 (1993).
- [8] H.-C. Jeong and E. D. Williams, *Surf. Sci. Rep.* **34**, 171 (1999).
- [9] C. Misbah, O. Pierre-Louis, and Y. Saito, *Rev. Mod. Phys.* **82**, 981 (2010).
- [10] C. Park, J. Yoon, and E. L. Thomas, *Polymer* **44**, 6725 (2003).
- [11] R. A. Segalman, *Mater. Sci. Eng. R* **48**, 191 (2005).
- [12] S. B. Darling, *Prog. Polym. Sci.* **32**, 1152 (2007).
- [13] *International Technology Roadmap for Semiconductors, 2011 Edition*, <http://www.itrs.net/Links/2011ITRS/Home2011.htm>.
- [14] W. M. Tong (editor), *Alternative Lithographic Technologies IV*, Proc. SPIE, **8323** (2012).
- [15] Y. S. Jung, J. B. Chang, E. Verploegen, K. K. Berggren, and C. A. Ross, *Nano Lett.* **10**, 1000 (2010).
- [16] W. K. Burton, N. Cabrera, and F. C. Frank, *Philos. Trans. R. Soc. London Ser. A* **243**, 299 (1951).

- [17] L. Leibler, *Macromolecules* **13**, 1602 (1980).
- [18] T. Ohta and K. Kawasaki, *Macromolecules* **19**, 2621 (1986).
- [19] O. Pierre-Louis, *Phys. Rev. E* **68**, 021604 (2003).
- [20] F. Liu and H. Metiu, *Phys. Rev. E* **49**, 2601 (1994).
- [21] A. Karma and M. Plapp, *Phys. Rev. Lett.* **81**, 4444 (1998).
- [22] P. N. Patrone and T. L. Einstein, *Phys. Rev. B* **85**, 045429 (2012).
- [23] P. N. Patrone and D. Margetis, *Submitted to Multiscale Modeling and Simulation*, (2013).
- [24] P. N. Patrone, T. L. Einstein, and D. Margetis, *Phys. Rev. E* **82**, 061601 (2010).
- [25] D. Margetis, P. N. Patrone, and T. L. Einstein, *MRS Proceedings* **1318**, (2011).
- [26] P. N. Patrone, R. Wang, and D. Margetis, *J. Phys. A: Math. Theor.* **44**, 315002 (2011).
- [27] P. N. Patrone, R. E. Caflisch, and D. Margetis, *Europhys. Lett.* **97**, 48012 (2012).
- [28] P. N. Patrone and G. M. Gallatin, *Proc. SPIE* **8323**, 83232Q (2012).
- [29] P. N. Patrone and G. M. Gallatin, *Macromolecules* **45**, 9507 (2012).
- [30] P. N. Patrone and G. M. Gallatin, *Proc. SPIE* **8680**, 86801R (2013).
- [31] A. Kühnle, *Current Opinion Coll. Interface Sci.* **14**, 157 (2009).
- [32] N. C. Bartelt, T. L. Einstein, and E. D. Williams, *Surf. Sci.* **312**, 411 (1994).
- [33] S. V. Khare and T. L. Einstein, *Phys. Rev. B* **57**, 4782 (1998).
- [34] N. C. Bartelt, J. L. Goldberg, T. L. Einstein, E. D. Williams, J. C. Heyraud, and J. J. Métois, *Phys. Rev. B* **48**, 15453 (1993).
- [35] X.-S. Wang, J. L. Goldberg, N. C. Bartelt, T. L. Einstein, and E. D. Williams, *Phys. Rev. Lett.* **65**, 2430 (1990).

- [36] N. C. Bartelt, J. L. Goldberg, T. L. Einstein, and E. D. Williams, *Surf. Sci.* **273**, 252 (1992).
- [37] V. I. Marchenko and A. Ya. Parshin, *Soviet Phys. JETP* **52**, 129 (1980).
- [38] E. E. Gruber and W. W. Mullins, *J. Phys. Chem. Solids* **28**, 875 (1967).
- [39] R. Najafabadi and D. J. Srolovitz, *Surf. Sci.* **317**, 221 (1994).
- [40] O. Pierre-Louis and C. Misbah, *Phys. Rev. B* **58**, 2259 (1998).
- [41] O. Pierre-Louis and C. Misbah, *Phys. Rev. B* **58**, 2276 (1998).
- [42] T.L. Einstein, H.L. Richards, S.D. Cohen, and O. Pierre-Louis, *Surf. Sci.* **493**, 460 (2001)
- [43] A. BH. Hamouda, A. Pimpinelli, and T. L. Einstein, *Europhys. Lett.* **88**, 26005 (2009).
- [44] J. W. Jeong, W. I. Park, M. Kim, C. A. Ross, and Y. S. Jung, *Nano Lett.* **11**, 4095 (2011).
- [45] D. P. Sanders, J. Cheng, C. T. Rettner, W. D. Hinsberg, H. Kim, H. Truong, A. Friz, S. Harrer, S. Holmes, and M. Colburn, *J. Photopolym. Sci. Technol.* **23**, 11 (2010).
- [46] J. Y. Cheng, C. T. Rettner, D. P. Sanders, H. Kim, and W. D. Hinsberg, *Adv. Mater.* **20**, 3155 (2008).
- [47] J. Y. Cheng, C. A. Ross, H. I. Smith, and L. Thomas, *Adv. Mater.* **18**, 2505 (2006).
- [48] J. D. Weeks and G. H. Gilmer, *Adv. Chem. Phys.* **40**, 157 (1979).
- [49] R. Marcelin, *Ann. Physique* **3**, 120 (1915).
- [50] E. Wigner, *Z. Phys. Chem.* **B 19**, 203 (1932).
- [51] H. Eyring, *J. Chem. Phys.* **3**, 107 (1935).
- [52] A. Zangwill, C. N. Luse, D. D. Vvedensky, and M. R. Wilby, *Surf. Sci.* **274**, L529 (1992).

- [53] C. N. Luse, A. Zangwill, D. D. Vvedensky, and M. R. Wilby, *Surf. Sci.* **274**, L535 (1992).
- [54] N. G. van Kampen, *Stochastic Processes in Physics and Chemistry*, 3rd ed.; North Holland: Amsterdam, 2007.
- [55] T. Chou, K. Mallick, and R. K. P. Zia, *Rep. Prog. Phys.* **74**, 116601 (2011).
- [56] A. F. Voter, *Introduction to the kinetic Monte Carlo method*, in *Radiation Effects in Solids*, K. E. Sickafus, E. A. Kotomin, and B. P. Uberuaga, Eds., Vol. 235, NATO Sci. Series; Springer: Dordrecht, The Netherlands, 2005, pp. 1–23.
- [57] T. Duguet, Y. Han, C. Yuen, D. Jing, B. Unal, J. W. Evans, and P. A. Thiel, *Proc. Nat. Acad. Sci.* **108**, 989 (2011).
- [58] J. G. Keizer, P. M. Koenraad, P. Smereka, J. M. Ulloa, A. Guzman, and A. Hierro, *Phys. Rev. B* **85**, 155326 (2012).
- [59] T. P. Schulze, P. Smereka, and W. E., *J. Comp. Phys.* **189**, 197 (2003).
- [60] G. Nandipati, Y. Shim, J. G. Amar, A. Karim, A. Kara, T. S. Rahman, and O. Trushin, *J. Phys. Cond. Matt.* **21**, 084214 (2009).
- [61] M. Ranganathan and J. D. Weeks, *Phys. Rev. Lett.* **110**, 055503 (2013).
- [62] A. Chatterjee and D. G. Vlachos, *J. Comput.-Aided Mater.* **14**, 253 (2007).
- [63] J. P. van der Eerden, P. Bennema, and T. A. Cherepanova, *Prog. Cryst. Growth Ch.* **1**, 219 (1978).
- [64] G. Ehrlich and F. G. Hudda, *J. Chem. Phys.* **44**, 1039 (1966).
- [65] R. L. Schwoebel and E. J. Shipsey, *J. Appl. Phys.* **37**, 3682 (1966).
- [66] J. G. Amar, *Comput. Sci. Eng.* **8**, 9 (2006).
- [67] P. Hänggi, P. Talkner, and M. Borkovec, *Rev. Mod. Phys.* **62**, 251 (1990).
- [68] K. A. Fichthorn and W. H. Weinberg, *J. Chem. Phys.* **95**, 1090 (1991).
- [69] J. G. Amar and F. Family, *Phys. Rev. Lett.* **74**, 2066 (1995).

- [70] P. Gambardella, H. Brune, K. Kern, and V. I. Marchenko, Phys. Rev. B **73**, 245425 (2006).
- [71] A. M. Kosevich, *Fundamentals of Crystal Lattice Mechanics*; Nauka: Moscow, 1972.
- [72] V. B. Shenoy, S. Zhang, and W. F. Saam, Surf. Sci **467**, 58 (2000).
- [73] P. -R. Cha, Elec. Mat. Lett. **3**, 103 (2007).
- [74] D. -J. Liu and J. D. Weeks, Phys. Rev. Lett. **79**, 1694 (1997).
- [75] H. -C. Jeong and J. D. Weeks, Surf. Sci. **432**, 101 (1999).
- [76] N. C. Bartelt, T. L. Einstein, and E. D. Williams, Surf. Sci. Lett. **240**, L591 (1990).
- [77] M. A. Ruderman and C. Kittel, Phys. Rev. **96**, 99 (1954).
- [78] K. Yosida, Phys. Rev. **106**, 893 (1959).
- [79] T. Kasuya, Progr. Theoret. Phys. (Kyoto) **16**, 45 (1956).
- [80] C. Kittel, Sol. State Phys. **22**, 1 (1968).
- [81] V. S. Stepanyuk, A. N. Baranov, D. V. Tsvilin, W. Hergert, P. Bruno, N. Knorr, M. A. Schneider, and K. Kern, Phys. Rev. B **68**, 205410 (2003).
- [82] V. S. Stepanyuk, L. Niebergall, R. C. Longo, W. Hergert, and P. Bruno, Phys. Rev. B **70**, 075414 (2004).
- [83] J. D. Howe, P. Bhopale, Y. Tiwary, and K. A. Fichthorn, Phys. Rev. B **81**, 121410(R) (2010).
- [84] W. Luo and K. A. Fichthorn, Phys. Rev. B **72**, 115433 (2005).
- [85] L. M. Roth, H. J. Zeiger, and T. A. Kaplan, Phys. Rev. **149**, 519 (1966).
- [86] Ph. Hofmann, B. G. Briner, M. Doering, H.-P. Rust, E. W. Plummer, and A. M. Bradshaw, Phys. Rev. Lett. **79**, 265 (1997).
- [87] T. Balasubramanian, L. I. Johansson, P.-A. Glans, C. Virojanadara, V. M. Silkin, E. V. Chulkov, and P. M. Echenique, Phys. Rev. B **64**, 205401 (2001).

- [88] T. L. Einstein, in *Physical Structure of Solid Surfaces*, W.N. Unertl, ed.; Elsevier: Amsterdam, 1996, chap 11.
- [89] T.L. Einstein, *Langmuir* **7**, 2520 (1991).
- [90] P. Hyldgaard and T. L. Einstein, *Europhys. Lett.* **59**, 265 (2002); *J. Cryst. Growth* **275**, e1637 (2005).
- [91] A. BH. Hamouda, A. Pimpinelli, and T. L. Einstein, *Surf. Sci.* **602**, 3569 (2008).
- [92] X. D. Zhu, *Phys. Rev. B* **57**, R9478 (1998).
- [93] D. Ackerman and J. Evans, *Multiscale Model. Simul.* **9**, 59 (2011).
- [94] W. A. Strauss, *Partial Differential Equations: An Introduction*, 2nd ed.; John Wiley and Sons: Hoboken, 2007.
- [95] N. Israeli and D. Kandel, *Phys. Rev. B* **60**, 5946 (1999).
- [96] W. Silvestri, A. P. Graham, and J. P. Toennies, *Phys. Rev. Lett.* **81**, 1034 (1998).
- [97] C. Roland and G. H. Gilmer, *Phys. Rev. B* **46**, 13428 (1992).
- [98] C. Roland and G. H. Gilmer, *Phys. Rev. B* **46**, 13437 (1992).
- [99] S. Kodiyalam, K. E. Khor, and S. Das Sarma, *Phys. Rev. B* **53**, 9913 (1996).
- [100] Z. Schuss, *Theory and Applications of Stochastic Processes: An Analytical Approach*; Springer: New York, 2010.
- [101] D. Margetis, *J. Phys. A: Math. Theor.* **43**, 065003 (2010).
- [102] M. Ozdemir and A. Zangwill, *Phys. Rev. B* **42**, 5013 (1990).
- [103] P. Nozières, *J. Phys. (France)* **48**, 1605 (1987).
- [104] A. Pimpinelli, H. Gebremariam, and T. L. Einstein, *Phys. Rev. Lett.* **95**, 246101 (2005).
- [105] H. Risken, *The Fokker-Planck Equation: Methods of Solution and Applications*, 2nd ed.; Springer: Berlin, 1989.

- [106] C. M. Bender and S. Orszag, *Advanced Mathematical Methods for Scientists and Engineers*; Springer: New York, 1999.
- [107] R. Kubo, Rep. Prog. Phys. **29**, 295 (1966).
- [108] M. Kardar, *Statistical Physics of Fields*; Cambridge University Press: Cambridge, 2007.
- [109] E.S. Fu, M.D. Johnson, D.-J. Liu, J.D. Weeks, and E.D. Williams, Phys. Rev. Lett. **77** 1091 (1996).
- [110] T. Ihle, C. Misbah, and O. Pierre-Louis, Phys. Rev. B **58**, 2289 (1998).
- [111] D. R. M. Williams and M. Krishnamurthy, Appl. Phys. Lett. **62**, 1350 (1993).
- [112] S. Tanaka, N. C. Bartelt, C. C. Umbach, R. M. Tromp, and J. M. Blakely, Phys. Rev. Lett. **78**, 3342 (1997); S. Stoyanov and V. Tonchev, Phys. Rev. B **58**, 1590 (1998); W. F. Chung, K. Bromann, and M. S. Altman, Int. J. Mod. Phys. B **16**, 4353 (2002).
- [113] A. W. Bosse, Macromol. Theory Simul. **19**, 399 (2010).
- [114] A. W. Bosse, E. K. Lin, R. L. Jones, and A. Karim, Soft Matter **5**, 4266 (2009).
- [115] R. Choksi and X. Ren, J. Stat. Phys. **113**, 151 (2003).
- [116] Y. S. Jung and C. A. Ross, Nano Lett. **7**, 2046 (2007).
- [117] G. O. R. Alberda van Ekenstein, R. Meyboom, G. ten Brinke, and O. Ikkala, Macromolecules **33**, 3752 (2000).
- [118] A. J. Nedoma, M. L. Robertson, N. S. Wanakule, and N. P. Balsara, Ind. Eng. Chem. Res. **47**, 3551 (2008).
- [119] A. N. Semenov, Macromolecules **27**, 2732 (1994).
- [120] F. A. Detcheverry, D. Q. Pike, U. Nagpal, P. F. Nealey, and J. J. de Pablo, Soft Matter **5**, 4858 (2009).
- [121] F. A. Detcheverry, D. Q. Pike, P. F. Nealey, M. Müller, and J. J. de Pablo, Faraday Discuss. **144**, 111 (2010).

- [122] K. C. Daoulas, M. Müller, M. P. Stoyovich, H. Kang, J. J. de Pablo, and P. F. Nealey, *Langmuir* **24**, 1284 (2008).
- [123] G. E. Stein, J. A. Liddle, A. L. Aquila, and E. M. Gullikson, *Macromolecules* **43**, 433 (2010).
- [124] S. Flügge, in *Practical Quantum Mechanics*, 2nd ed.; Springer-Verlag Publishers: New York, Heidelberg & Berlin, 1994, p 89.
- [125] J. Lekner, *Am. J. Phys* **75**, 1151 (2007).
- [126] J. J. Sakurai, in *Modern Quantum Mechanics*, Revised ed.; S. F. Tuan, Ed.; Addison-Wesley Publishing Company: New York, 1994, p 285.
- [127] M. P. Stoykovich, K. Ch. Daoulas, M. Müller, H. Kang, J. J. de Pablo, and P. F. Nealey, *Macromolecules* **43**, 2334 (2010).
- [128] C. T. Black, R. Ruiz, G. Breyta, J. Y. Cheng, M. E. Colburn, K. W. Cuarini, H. -C. Kim, and Y. Zhang, *IBM J. Res. & Dev.* **51**, 605 (2007).
- [129] B. S. Swartzentruber, Y.-W. Mo, R. Kariotis, M. G. Lagally, and M. B. Webb, *Phys. Rev. Lett.* **65**, 1913 (1990).